

CONCENTRATOR PHOTOVOLTAIC SYSTEM DESIGN USING OFF-ANGLE TRACKING

by

Nathaniel Tanti

B.Eng.Mgt., McMaster University 2010

A Thesis

Submitted to the School of Graduate Studies

in Partial Fulfillment of the Requirements

for the Degree

Master of Applied Science

McMaster University

©Copyright by Nathaniel Tanti, January-2013

MASTER OF APPLIED SCIENCE

MCMASTER UNIVERSITY

(Department of Engineering Physics)

Hamilton, Ontario

TITLE: CONCENTRATOR PHOTOVOLTAIC SYSTEM DESIGN USING OFF-ANGLE TRACKING

AUTHOR: Nathaniel Tanti, B.Eng.Mgt., McMaster University

THESIS SUPERVISOR: Dr. Rafael Kleiman

NUMBER OF PAGES: 121

Abstract

This thesis will discuss a novel method of tracking the Sun. An essential aspect of the method is to rotate a polar aligned single axis tracker such that the angle between the direction of the Sun and the normal of the module remains at a constant angle of 23.44 degrees or a few degrees more. The rotational symmetry that arises from this circumstance enables seasonal tracking to occur inside the module whilst maintaining efficient concentration. Several possible optical designs and a preferred optical design are presented as a way of implementing the tracking method. The tracking method is also open to a plethora of different concentrator photovoltaic system designs which may be integrated onto rooftops more effectively than conventional dual axis tracking systems.

Acknowledgements

I would like to thank my supervisor, Dr. Kleiman, for providing me with the freedom to pursue this project. Thank you George Chiran for your feedback through our discussions. I would also like to thank Shermeen, Dr. Kitai and Dr. Xu for reading a proving feedback on how to improve both the content and layout of my thesis. I would like to thank my parents for being awesome! And the rest of my friends and family for being equally awesome!

Contents

Abstract.....	ii
Acknowledgements.....	iii
Contents.....	iv
Table of Figures.....	vi
Table of Tables.....	xi
1 Introduction.....	1
2 CPV Design.....	2
2.1 Why CPV?.....	2
2.2 Very Brief Market Overview.....	4
2.3 Optical Design.....	5
2.4 Other Technical Limitations.....	6
3 The Sun.....	9
3.1 Introduction.....	9
3.2 The Earth Sun Interaction.....	10
3.3 Atmospheric Effects.....	12
4 Tracking Systems.....	14
4.1 Why Track?.....	14
4.2 Traditional Tracking System Designs.....	15
4.3 Control System.....	16
4.4 Tracker Accuracy.....	17
4.4.1 Tracker Fluctuation and Acceptance Angle Analysis.....	19
4.5 Less Conventional Tracking.....	22
5 Off-angle Tracking Theory.....	26
5.1 Introduction.....	26
5.2 2D Theoretical Limits.....	27
5.2.1 Cosine Loss.....	27
5.2.2 Limitations of Different Optical Configurations.....	29
5.3 GRIN Lenses.....	36
5.4 Adjacent Trackers.....	38
5.5 Off-Angle Tracking Derivation.....	39

6	Concentrator Optical Design.....	46
6.1	Introduction	46
6.1.1	Definitions	46
6.2	On-Axis Designs.....	46
6.2.1	Plano Convex On-Axis Lens	46
6.2.2	Convex Plano On-axis Lens.....	53
6.3	Off-Axis Designs	58
6.3.1	Single Plano Convex Off-Axis Lens	58
6.3.2	Convex Plano Off-Axis Lens.....	58
6.3.3	Single Convex Plano Off-Axis Lens with Tilted Receiver	63
6.3.4	Secondary Optic Design	67
6.3.5	Convex Plano Lens with Tilted CPC Secondary	67
6.3.6	Convex Plano Lens with an Axial Symmetrical Mirror	68
6.3.7	Convex Plano Lens and Plano Convex Lens.....	73
7	A Preferred Off-Angle Optical Design	77
7.1	Mechanical Design	77
7.1.1	Basics.....	77
7.1.2	Mirror and Lens Manufacturability.....	79
7.1.3	Assembly	79
7.1.4	Receiver Symmetry	81
7.1.5	Louvered Tracking System	82
7.1.6	Internal Tracking System.....	82
7.2	Lens Design	85
7.2.1	Specification.....	85
7.2.2	Illumination Analysis	86
8	Conclusion.....	92
	References	94
	Appendix I. Étendue Metric	100
	Appendix II. Geometric Optics and the Application of the Characteristic Equation	101

Table of Figures

Figure 2.1 – NREL chart for world record solar cell efficiencies [9].	3
Figure 2.2 - Illustration of the concentrator’s acceptance angle θ_s , the numerical aperture angle θ_x , and the emission angle from the cell θ_e [29].	6
Figure 2.3 - Maximum theoretical efficiency of a single bandgap solar cell for different temperatures and concentrations.	7
Figure 3.1 - Illustration of Earth's orbit around the Sun.	10
Figure 3.2 –An illustration of blackbody radiation and various standard solar spectra including the AM0 (ASTM E490) Extraterrestrial spectrum; the AM1.5 Global (ASTMG173); the AM1.5 Direct+Circumsolar (ASTMG173); and AM3 and AM10 spectra generated by SMARTS [41].	12
Figure 3.3 - Average sunshape profile[42].	13
Figure 4.1 - Tracking schemes a) a pedestal tracker; b) a tilt roll tracker; c) a carousel tracker; d) a louvered tracking system (adapted from [44]).	16
Figure 4.2 - From a LPI presentation [45].	18
Figure 4.3 - A tracking accuracy sensor mounted on one of Inspira’s CPV lab tracker [50].	19
Figure 4.4 – Illustration of the folding concept.	20
Figure 4.5 - System performance as a function of acceptance angle and standard deviation.	21
Figure 4.6 - Illustration of a low profile rooftop tracker with kohler integration and mirrors [60].	23
Figure 4.7 – Concept of artificial heliotropism [75].	24
Figure 5.1 - Example of an optical design that focuses light incident at a 23.44° angle with respect to the normal of the primary optic.	27
Figure 5.2 - Illustration of cosine loss.	28
Figure 5.3 - Cosine loss for adjacent GRIN lenses; A is the conventional definition of the aperture size (or in this 2D case, length), A0 is the projection of A, delta is the angle the source subtends, and theta0 is the angle the source makes with respect to A.	29
Figure 5.4 – Single lens and tilted receiver configuration.	30
Figure 5.5 – Single lens and flat receiver configuration.	30
Figure 5.6 - Illustration of the relationship between the acceptance angle of a secondary optical element that is rotationally symmetric about the normal of the back plane and the étendue of the incident beam from the primary optical element.	31
Figure 5.7 - Illustration of how a hole would be introduced into the secondary optic.	32
Figure 5.8 - Illustration of how an incident beam with a principle ray that is mainly normal to the back plane is able to focus onto a rotationally symmetric secondary optical element (or receiver); note that the acceptance angle is actually larger than the solid angle that the beam subtends in order to allow for some alignment tolerance.	33
Figure 5.9 - Beam steering with a refractive ring.	34
Figure 5.10 - Illustration of a convex-plano, and plano-convex lens configuration.	35

Figure 5.11 - Secondary optic which brings off-axis beam back on axis.....	36
Figure 5.12 – Illustration of the Luneburg lens as a radiation concentrator from an extended far-field source of angular extend $2\theta_a$ onto a spherical-cap absorber (of arc length $2\theta_a$ in cross section). The three wave fronts are at the two extreme angles plus a nominal incidence angle of angle zero. [80].	37
Figure 5.13 – Spherical gradient-index lenses as radiation concentrators illustrated for an incident extended far-field source of angular extent $2\theta_a$ (in analogy to the Luneburg lens, $r_1 = 1$). The three wave fronts are traced at the two extreme angles plus a nominal incidence angle of zero. $R_1 = 2.55$ (r_1 greater than unity), also corresponding to the fish-eye lens [80].	37
Figure 5.14 – Self shading of adjacent trackers under different tracking configurations.	38
Figure 5.15 - Diurnal tracking without a daily transition.	39
Figure 5.16 - Diurnal tracking with a daily transition.....	39
Figure 5.17 – Illustration of the collector reference frame with respect to a Earth surface reference frame.	40
Figure 5.18 – Illustration of a conventional dual axis tracker within the collector reference frame.	41
Figure 5.19 – Illustration of an on-axis tracker.	41
Figure 5.20 - Projection of \mathcal{S} in the collector plane reference system.	42
Figure 5.21 - Illustration of the collector’s diurnal motion phase shifted by $\pm\psi$	43
Figure 5.22 - Mapping between the declination, δ , and off-angle, κ , with the phase shift, ψ , and orientation, ϕ , of the focal point on the receiver plane.	45
Figure 6.1 - Illustration of a focused beam at 0° (blue), 0.5° (green) and 1° (red) incidence; the points A and B are shown here and in Figure 6.2 and Figure 6.3 to show the correspondence of each diagram.....	47
Figure 6.2 - Phase space diagram of tangential rays at the aperture (top) and the receiver (bottom).....	48
Figure 6.3 – Spot diagram of edge rays incident at 0° , 0.5° and 1° ; The black spot correspond to rays within the tangential, sagittal, and all other planes that intersect the principle ray.....	49
Figure 6.4 – Encircled energy diagram for the on-axis plano convex lens; there is a total of 7.854 W incident on the receiver plane.....	51
Figure 6.5 – Irradiance distribution histogram for the on-axis plano convex lens.	51
Figure 6.6 – Irradiance distribution diagram for the on-axis plano convex lens.	52
Figure 6.7 - Transmission curve for the on-axis plano convex lens.	52
Figure 6.8 - Illustration of a focused beam at 0° (blue), 0.5° (green) and 1° (red) incidence; the points A and B are shown here and in Figure 6.9 and Figure 6.10 to show the correspondence of each diagram.....	53
Figure 6.9 - Phase diagram.....	54
Figure 6.10 - Illustration of edge rays on the receiver.....	55

Figure 6.11 – Encircled energy diagram for the on-axis convex plano lens; the peak energy incident is 7.854 W.....	56
Figure 6.12 – Irradiance distribution histogram for the on-axis convex plano lens.	56
Figure 6.13 – Irradiance distribution diagram for the on-axis convex plano lens.	57
Figure 6.14 – Transmission curve for the on-axis convex plano lens; clearly, the cut-off is much sharper for the convex-plano lens than for the plano-convex lens.....	57
Figure 6.15 - Illustration of severe astigmatism and field curvature; the intensity distribution of light from the lens is also not rotationally symmetric about the receiver plane’s normal.	58
Figure 6.16 - Illustration of astigmatism.	59
Figure 6.17 – Encircled Energy Diagram for the convex plano off-axis lens; the peak energy is 7.1045 W.	61
Figure 6.18 – Irradiance distribution histogram for the convex plano off-axis lens.....	61
Figure 6.19 – Irradiance distribution diagram for the convex plano off-axis lens.....	62
Figure 6.20 – Intensity plot for a 24° (blue), 25° (red), and 26° (green) incident beam of sunlight; the blue circle indicates the acceptance angle that a secondary optic made to be rotationally symmetric about the normal of the back plane (corresponding to the blue cone in Figure 6.15); the red circle represents the boundary of the intensity distribution observed at the receiver from the primary lens (corresponding to the red cone in Figure 6.15).....	62
Figure 6.21 - Convex plano off axis lens with a tilted receiver.	63
Figure 6.22 - Edge ray analysis; the blue rays represent the edge rays from a source infinitely far away but subtends an arc of 1.2665°; ray bundle 1 and 2 originate from a point source in the tangential plane at 23.73° and 26.27° respectively.	65
Figure 6.23 – Spot diagram illustrating the intersection of the edge rays of a source subtending an angle of 0.2665° with the receiver plane (blue); a point source in the tangential plane at 23.73° (green); and a point source in the tangential plane at 26.27° (red).....	66
Figure 6.24 - Diagram of an off-angle convex plano lens with a tilted CPC secondary optic.	67
Figure 6.25 - Illustration of a convex-plano lens using a secondary optic that is rotationally symmetric about the primary’s optical axis.	68
Figure 6.26 – Larger view of the system showing the parabola and receiver position.	69
Figure 6.27 – Encircled Energy Diagram for an off-axis convex plano lens with an axially symmetric reflective secondary; the maximum enclosed power 7.1181 W.	71
Figure 6.28 – Irradiance distribution histogram for an off-axis convex plano lens with an axially symmetric reflective secondary.....	71
Figure 6.29 – Irradiance distribution diagram for an off-axis convex plano lens with an axially symmetric reflective secondary.....	72
Figure 6.30 – Transmission angle diagram for an off-axis convex plano lens with an axially symmetric reflective secondary.....	72
Figure 6.31 - Convex Plano-Plano Convex Lens combination with a 25° design angle.....	73

Figure 6.32 – Encircled energy diagram for the convex plano and plano convex off-axis lens system; the incident energy is 7.1181 W and the energy incident on the receiver is 6.9187 W. .	75
Figure 6.33 – Irradiance distribution histogram for the convex plano and plano convex off-axis lens system.....	75
Figure 6.34 – Irradiance distribution diagram for the convex plano and plano convex off-axis lens system.	76
Figure 6.35 – Transmission diagram for the convex plano and plano convex off-axis lens system.	76
Figure 7.1 - Illustration of the mechanical motion of the secondary optic with respect to the primary optic.....	77
Figure 7.2 - Illustration of a simplified and hypothetical CPV module assembly.	80
Figure 7.3 - Illustration a simplified and hypothetical off-angle tracking CPV module.	80
Figure 7.4 – Possible secondary optic configuration.	81
Figure 7.5 – Circular III-V Cells [85].	81
Figure 7.6 - Arrangement of a louvered tracking system from PHILLIPS which is analogous to what the off-angle tracking method allows for [87]......	82
Figure 7.7 - Illustration of an array of secondary optical elements kept in synchronous motion through an intermediate gear assembly.....	83
Figure 7.8 - Another possible way of simultaneously adjusting the secondary optical elements.	83
Figure 7.9 - Synchronous secondary optic movement achieved through a belt, chain or another long, flexible construct.....	84
Figure 7.10 - Synchronous motion achieved with a stiff structure attached to pivoting joints on the secondary optical elements.....	85
Figure 7.11 - Edge rays for a 1° radius source.....	87
Figure 7.12 - Secondary cross-section showing how the NA is not completely filled; the 37° and 20° extent along the L axis correspond to the extent seen in Figure 7.16.	88
Figure 7.13 – Encircled energy diagram for the off-axis concentrator with dual freeform mirrors; the peak energy incident is 7.1181 W.	89
Figure 7.14 – Irradiance distribution histogram for the off-axis concentrator with dual freeform mirrors.....	89
Figure 7.15 – Irradiance distribution diagram for the off-axis concentrator with dual freeform mirrors.....	90
Figure 7.16 – Intensity spot diagram of rays from a 1° half angled source; the illustration is intended to show the angular extent of the rays within the 0.243cm radius receiver.	90
Figure 7.17 - Transmission for sources of a 0.5° (cyan), 0.75° (red) and 1° (yellow) half-angle....	91
Figure II-1 - Illustration of the resulting rays from Equation (33) and (34).....	106
Figure II-2 - Illustration of edge rays incident on a parabola with a 45° rim angle.....	108
Figure II-3 - A projection of Appendix Figure II-4 showing the phase space at the focal plane. .	108

Figure II-4 - Illustration of the final ray position on the focal plane as a function of p_{02} and p_{12} .
..... 109

Table of Tables

Table 1 - Limiting efficiencies and possible implementations [8].....	4
Table 2 - Lens Specifications (cm) for a plano convex lens.....	47
Table 3 – Étendue analysis for a plano convex lens at 95% transmission.....	49
Table 4 - Lens Specifications (cm) for a convex plano lens.....	53
Table 5 - Étendue analysis for a convex plano lens at 95% transmission.....	55
Table 6 - Lens Specifications (cm) for an off-axis convex plano lens with a tilted receiver.....	63
Table 7 – Lens Specifications (cm) for a convex plano lens with an axially symmetric reflective secondary.....	69
Table 8 - Étendue analysis results for the convex plano lens with an axially symmetric mirror secondary.....	70
Table 9 - Lens Specifications for the convex plano lens and plano convex lenses.....	73
Table 10 - Étendue analysis results for the convex plano lens and plano convex lenses.....	74
Table 11 - Lens Specification (cm) for a off-axis convex plano lens with two reflective mirror secondaries.....	85
Table 12 - Étendue analysis results.....	87

1 Introduction

In recent times the world has met an energy crises characterized by a rise in energy costs, a perception of over consumption, and too much pollution. The term 'green energy' has arisen as a way of communicating what energy sources may power our future in a sustainable way. Photovoltaic cells are one of the most notable examples which, if made cheap enough, could potentially harness the number one source of energy in the solar system, our Sun. There are many different types of photovoltaic technologies, and even though silicon based photovoltaic cells dominate the market today, there is no indication that they won't one day be replaced by more advanced technologies. Concentrator photovoltaic (CPV) technology refers to any photovoltaic technology that uses an optical system to concentrate light. Optics are used because advanced photovoltaic cells are made of expensive materials. Therefore, by necessity, large area photovoltaic cells must be replaced by a large, inexpensive lens that focuses sunlight onto a small photovoltaic cell. Because the laws of thermodynamics prohibit high concentration without the use of a tracking system, a variety of different methods have been developed to track the Sun. The goal of this thesis will be to illustrate an entirely new method of tracking and concentrating sunlight dubbed off-angle tracking. Furthermore, various patent pending embodiments of the tracking method will also be presented and analyzed (*N. Tanti and R. Kleiman, USPTO patent application, Jan. 23, 2013*).

The thesis is broken up into seven chapters. The first chapter will familiarize the reader with some basics of concentrator photovoltaic design. The second chapter will go over the relevant aspects of the Sun in relation to CPV systems. A central aspect of this thesis is the integration of both the optical and tracking aspects of the CPV system. The third chapter will review the basic aspects of solar tracking and introduce some other less common tracking methods. Within the knowledge of the author, the theory of a completely new approach to CPV systems shall be introduced in the fourth chapter. Building upon the knowledge of the previous chapters, chapter five shall guide the reader through the basic aspects of the most common types of concentrator optical designs, eventually leading to optical designs for the proposed off-angle tracking approach. In chapter six, a solution to the problems presented in chapter five regarding the optics using the off-angle tracking is presented.

2 CPV Design

2.1 Why CPV?

The main motivation of CPV system design is the recent advent of high efficiency multi-junction photovoltaics which can be mass produced at an average of about 40% efficiency [1], but cost about two orders of magnitude more than conventional photovoltaic cells by area, which is approximately $\$1\text{-}8/\text{cm}^2$ [2],[3],[4]. These cells can be manufactured by over 12 companies [5]¹ and have predominately been used in space base applications where cost is driven by predominantly by weight ($\sim\$20,000$ USD per pound) [6]. For use in terrestrial applications, these cells must be used in conjunction with concentrating optics. As a consequence, the cost burden shifts from the cell to the optics and tracking system.

As seen in Figure 2.1, multi-junction solar cells have proven themselves to be the most efficient type of cell by far. In the current industry state, silicon PV simply cannot compete with conventional utility scale power supplies in many regions around the world without government subsidy. The exceptions are places with lots of sunshine and/or very high local electricity prices. However, as seen for more than a decade and especially in recent years, photovoltaics are quickly becoming more wide spread. A simple cost analysis of the 2012 silicon module cost structure shows that efficiency has by far, the greatest influence on the total cost of a PV system [7]. *Ceteris paribus*, efficiency acts to reduce the effective cost of every power independent component, not just in the module, but among the BOS (balance of system) components as well.

In the author's opinion, high efficiency PV is the only long term option that will allow for a significant share of the utility scale energy market. How high this efficiency should be is a matter of debate. But, it is clear that III-V materials and expensive processing methods required to make the cells will likely be prohibitive without some breakthroughs. In addition, it turns out that the efficiency of a typical cell actually increases under concentrated light so that the theoretical limit of a triple junction cell actually increases from 49.3% under no concentration to a maximum of 63.8% under concentration [8].² Thus, not only will the use of concentrators likely be necessary to make the use of the most efficient cells cost effective, but they will also push the cell efficiencies closer to their maximum theoretical limit.

¹ See Table 5

² As discussed in the Optical Design section, the maximum cell efficiency can be made independent of concentration, but in any case tracking will always be a must.

Best Research-Cell Efficiencies

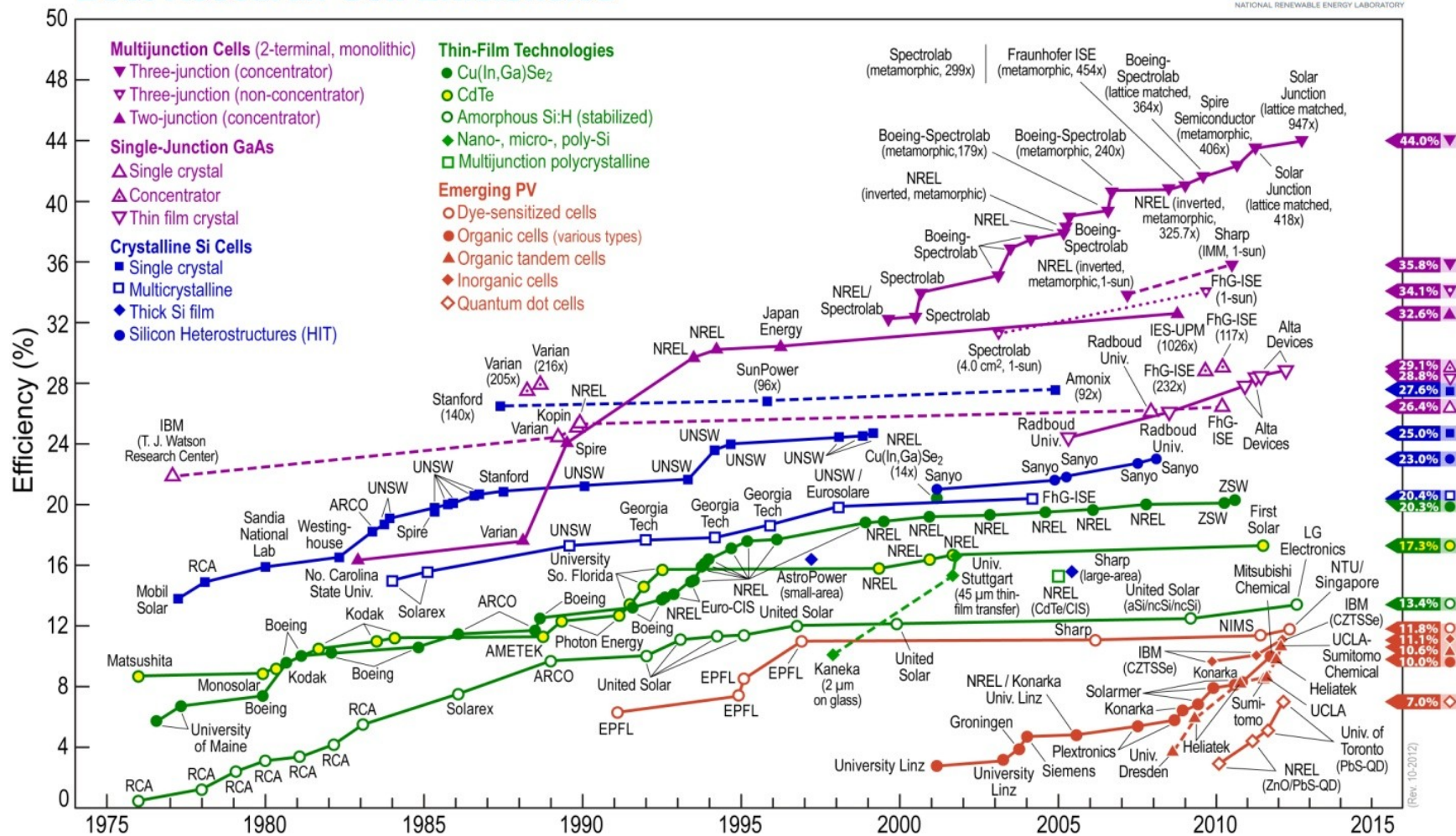


Figure 2.1 – NREL chart for world record solar cell efficiencies [9].

Table 1 shows the upper limit in how efficient cells can be. To gain an appreciation for the state of different photovoltaic technology, consider the 31.8% theoretical limit of single bandgap solar cells and the 25.0% record for silicon cells [10], [11]. This is rather impressive especially considering the fact that silicon is an indirect bandgap material. On the other hand, multi-junction cells have reached 44.0% efficiency at 947x concentration whereas the theoretical limit under direct sunlight is 63.8% [12]. The point is that the incremental improvements in laboratory silicon cell efficiency stopped nearly a decade ago. In contrast, multi-junction technology has been showing steady improvements and there is certainly plenty of headroom for growth, especially from a theoretical standpoint.

Table 1 - Limiting efficiencies and possible implementations [8].

Efficiency Limit	Direct	Global	Implementation
Landsberg	93.3%	73.7%	Circulators Antenna
Multicolour	86.8%	68.2%	Hot carrier Tandem cells Impact ionization
Black-body	85.4%	53.6%	Thermal electric Thermophotovoltaic Thermionics
3-level	63.8%	49.3%	Up- & down- converters 3 cell stack Impurity PV Impurity band Up-converters
2 cells	55.7%	42.9%	2 cell stack
Single Junction	40.8%	31.0%	Single junction

2.2 Very Brief Market Overview

Although economies of scale can bring down the cost of PV, other factors such as research and development (R&D), knowledge spillovers, and market dynamics play a far more critical role [13]. For example, some believe that the recent dramatic drop in photovoltaic cell prices had more to do with the sudden drop in silicon prices than the experience curve effect [14]. It is also clear from Figure 2.1 that R&D has led to the increased efficiency of silicon PV over the past decades. Also, the technological developments that led to the 25% efficient silicon cell in the 1990s is only now being gradually implemented in industry [15].

A significant market factor is that the amount of funding into solar R&D has a significant positive correlation with the price of crude oil. Perhaps one reason for this is that photovoltaic

adds no new functionality that people are willing to pay for except in a few cases where photovoltaic turns out to be cheaper or more convenient than current incumbent technologies.

It should be emphasized that the silicon photovoltaic industry would not have existed if silicon production from the microelectronics industry did not exist. Historically, silicon based technology has been immensely successful and has managed to obliterate technological advancement based on alternative materials. On this line of thought, potential future advancements may be in the area of advanced silicon based cells that go beyond the limit of single bandgap c-Si cells.

However, despite the previous success of silicon photovoltaics for terrestrial applications, mass production of much more efficient multi-junction cells has managed to find a market in space based applications. If very high efficiency is the goal, it is more logical to adopt the existing multi-junction technology from the space industry than to try and introduce a completely new, advanced solar technology. Long development phases for a brand new product with only marginal gains in efficiency within a market with rapid cost reductions will not necessarily be successful.

2.3 Optical Design

Perhaps one of the most important advents in lens manufacturing technology is the ability to affordably manufacture freeform surfaces within optical tolerances [16]–[22]. In particular, the nonimaging optical design discussed in this thesis would not be possible without freeform optics. And just like many other areas of engineering, modern optical designs are largely made using numerical techniques on computers. Older analytical methods, such as the use of Hamilton’s characteristic function, are still very useful in providing general insight and closed form solutions for special cases. An example of Hamilton’s characteristic equation is given in Appendix II.

In optics, a generalized Cartesian oval is the name given to a freeform surface which couples two non-spherical wavefronts [16]. It is actually an extension of Cartesian ovals which were first discovered by Descartes who showed that they could be used to couple any two spherical wavefronts. It was Levi-Cevita who generalized this wavefront coupling problem from spherical to non-spherical wavefronts. He showed in 1900 that unlike Cartesian ovals, which are strictly limited to aspheric surfaces, the general solution to the wavefront coupling problem leads to a freeform surface [23]. In other words, Levi-Cevita showed that a single deflective surface is enough to transform any normal congruence of rays into any other normal congruence of rays.

The converse of this theorem was actually found earlier by Malus in 1808 [24], [25], and later more generally by others including Dupin in 1816. The theorem, which is often referred to

as the Malus-Dupin theorem, states, *a normal rectilinear congruence remains normal after any number of refractions or reflections* [26].

Now, both the Malus-Dupin theorem and the converse theorem proven by Levi-Civita only concern themselves with a single surface. In more modern times, computers have allowed us to look at more complicated situations involving two or more surfaces. Although it has not been proven analytically, it has been shown that numerically that two surfaces are able to simultaneously transform any two normal congruences of rays into any other two normal congruences of rays [27].

Another important aspect of the CPV system's optical design is how the numerical aperture should match the PV cell's acceptance angle as closely as possible. The fact is that the theoretical limiting efficiency of a photovoltaic system is only reached once all emission of photons from the cell are sent straight back towards the Sun [28][29][30]. In optics, the solution to this very well known light coupling problem is that the étendue of both the source and receiver must match. Thus, to achieve maximum system efficiency, it only makes sense that the cell's emission angle and the numerical aperture of the concentrator be tailored to one another.

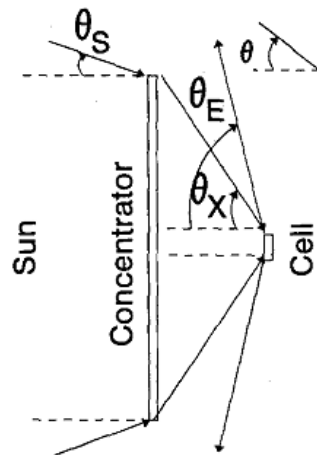


Figure 2.2 - Illustration of the concentrator's acceptance angle θ_x , the numerical aperture angle θ_x , and the emission angle from the cell θ_E [29].

2.4 Other Technical Limitations

Arguably, the most important feature of all photovoltaic systems is efficiency. Consider the effect of concentration and temperature on the theoretical efficiency limit which is illustrated in Figure 2.3 for a single bandgap cell. Although CPV systems often do not use single bandgap cells, the main point that is made here is that both concentration and low operating temperature contribute significantly to the overall efficiency of the system.

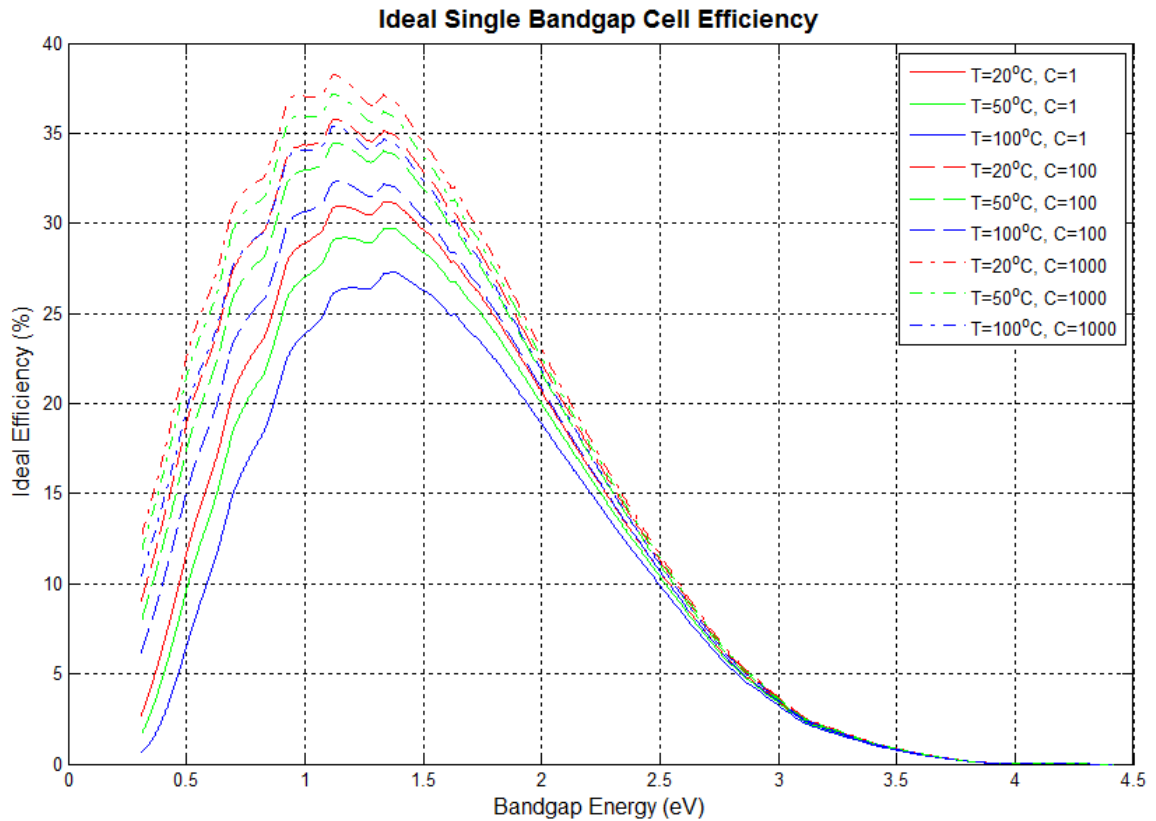


Figure 2.3 - Maximum theoretical efficiency of a single bandgap solar cell for different temperatures and concentrations.

The cell size also plays an important role in the practical limits associated with nearing the theoretical performance limits. Up to a point, the smaller the cell the more efficient passive thermal management is, the shorter the optical focal length can be, and the lower the cell's series resistance. The benefit is a smaller module profile, cheaper heat sinks, and higher operating efficiency under inhomogeneous illumination and high concentration.

Despite the advantageous of small cells, the cost of assembly and interconnects will go up, which may be why one will typically find cells on the order of 1 cm². The solution may lie in massively parallel assembly methods, such as the ones developed by the John Rogers group [31], which can act to reduce this cost.

In general, the requirements for any CPV prototype can be categorized into performance, cost and reliability. According to Kurtz, we can separate these three categories further [5].

Performance can be further broken down into optical efficiency, thermal management, manufacturing tolerances, tracking performance, wind flexure, thermal expansion and contraction, and optical surface soiling.

Cost requirement mandate that inexpensive materials be used, components are easily manufactured, and that inexpensive assembly is achievable.

Reliability is also very important and includes aspects such as degradation of optical components, loss of adhesion between the cell and heat sink or the cell and secondary optic, and long term performance of the tracker.

The list of requirements above is not meant to be exhaustive; it is only intended as a guide. Most of these requirements are linked in some way which has led to difficulty in designing a system which can meet all requirements simultaneously.

3 The Sun

3.1 Introduction

The Sun can essentially be thought of as an immense ball of hot plasma. To think of it as just a condensed ball of gas is incredibly misleading since the ability for plasma to conduct currents gives rise to very complex phenomena. Thanks to satellites such as SOHO (Solar and Heliospheric Observatory), SDO (Solar Dynamic Observatory), more and more experimental evidence is helping to reveal the true nature of the Sun every day.

Due to the immense gravitational attraction on the Earth from the Sun, the Earth's trajectory is perturbed in a way that causes it to orbit around the Sun. In most cases, this orbit can be considered nearly circular. In reality, it actually orbits the Sun in an ellipse causing it to annually come closer and go further away from the Sun by an amount that actually causes the Sun's apparent radius to change by about one hundredth of a degree. Furthermore, the Earth is tilted with respect to the plane in which it orbits, called the ecliptic plane, by 23.43928108° [32]. It is this tilt which causes our seasons and the requirement for seasonal tracking in CPV systems. Although it is slightly beyond the discussion at hand, neither the elliptical orbit of the Earth around the Sun nor the tilt of the Earth remain constant either. They change very slowly over tens of thousands of years in cycles referred to as Milankovitch cycles, which have several notable effects. One such effect is the apparent shift of the solstice and equinox relative to the perihelion and aphelion. Another is the influence on global climate change [33].

As seen in Figure 3.1, the Earth revolves about the Sun so that we have the spring and fall equinox in the months of March and September respectively. We also experience the summer and winter solstice during June and December, respectively. Figure 3.1 also shows us the location of the closest and furthest position of the Earth from the Sun. These points are referred to as the perihelion and aphelion, respectively. There is about a 3% difference in the distance from the Sun at the aphelion and perihelion, which as mentioned before gives rise to a measureable difference in the apparent size of the Sun on Earth. Due to the implications Earth's noncircular orbit can have on both tracking systems and the optics of CPV systems, it is worthwhile to understand it in a bit more detail.³

³ No standard size of the Sun has been found in literature, so this exercise will also serve to justify the definition used through the thesis.

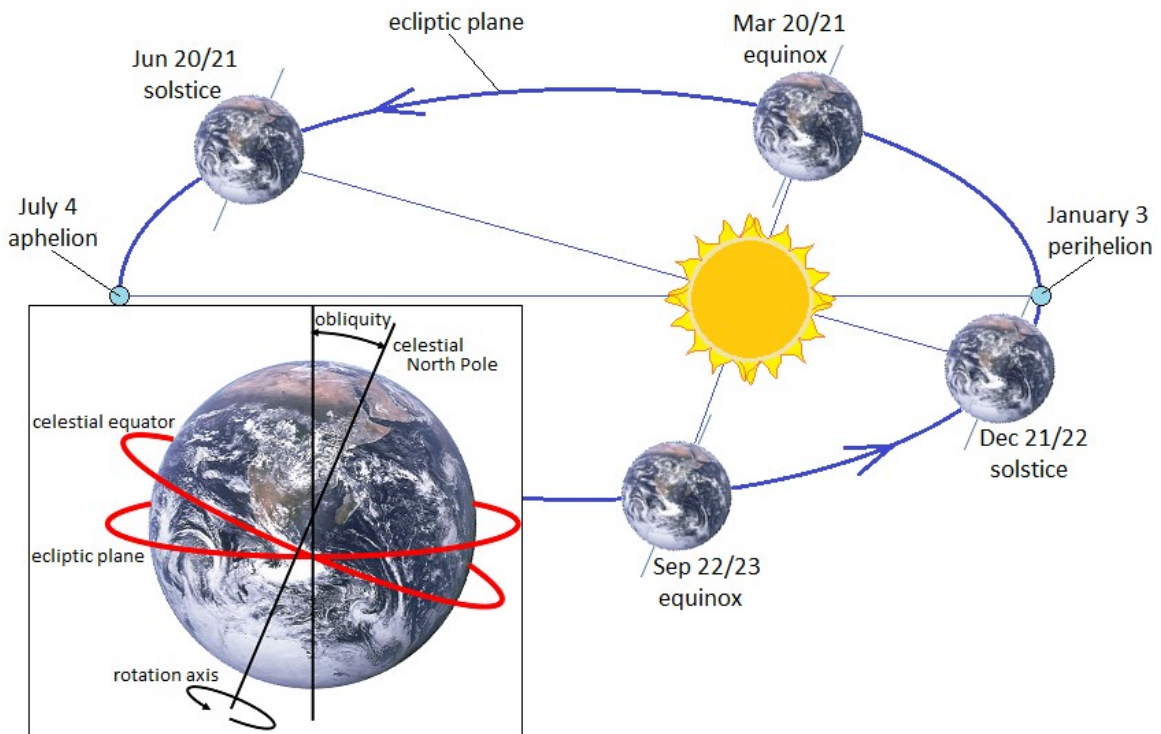


Figure 3.1 - Illustration of Earth's orbit around the Sun.

3.2 The Earth Sun Interaction

A common unit used to describe astronomical scales is referred to as an astronomical unit, which is defined as $1\text{AU} = 149,597,870,700 \pm 3\text{m}$. This is roughly the mean distance between the Earth and the Sun [34]. According to the ephemerides from NASA [35], the semi major axis of the Earth's orbit, a , is 1.00000261 AU and the eccentricity, e , is given to be 0.01671123.

From basic geometry, we know that the aphelion and perihelion are given by the respective Equations (1) and (2).

$$\text{aphelion} = a(1 + e) \quad (1)$$

$$\text{perihelion} = a(1 - e) \quad (2)$$

Substituting in the values a and e ,

$$\text{aphelion} = 1.016713884 \text{ AU}$$

$$\text{perihelion} = 0.9832913364 \text{ AU}$$

The average over the mean anomaly gives a time average distance of the Earth from the Sun equal to,

$$a \left(1 + \frac{1}{2}e^2\right) = 1.000142243 \text{ AU} \quad (3)$$

We know the eccentricity of Earth's orbit causes the apparent size of the Sun to vary, but what is the Sun's absolute size? The absolute size of the Sun has been measured empirically with space based instruments such as SOHO and SDO. The Sun's radius has historically been a topic of much debate, mostly due to the fact that measurements were made through the atmosphere which introduced aberrations and apparent cyclical variation. This sometimes misled people to create false theories about the how the Sun works. Modern space-based instruments have currently arrived at results disputed within about 500km, due mostly to systematic errors [36]. For our discussion, we shall quote the NASA ephemerides which has put the radius at 696,000 +/- 40 km [36], [37]. From this value, we find the apparent size at the aphelion, $\delta = 0.2622^\circ$; the perihelion, $\delta = 0.2711^\circ$; and mean anomaly, $\delta = 0.2665^\circ$.

The solar spectrum closely follows the blackbody radiation law for a body that is at 5778 K, such as the one illustrated in Figure 3.2 [37]. Were the sun a perfect blackbody at 5778 K, the irradiance at the sun's surface would be, $\sigma T^4 = 6.32 \cdot 10^6 \text{ W} \cdot \text{m}^{-2}$. In addition, empirical evidence has shown that the Sun's shape is remarkably spherical and unvarying despite the Sun's rapid rotation, numerous cycles and other dynamic fluctuations [38]. That being the case, we can approximate with reasonable accuracy how sunlight is incident on the Earth by using a so called "geometric factor" which shall describe how isotropic radiation from a spherical source is incident on a Lambertian receiver.

With the geometric factor, $B0$, we can obtain the irradiance on the Earth from [39],

$$\Phi = \frac{B0}{\pi} \sigma T^4 \quad (4)$$

Or,

$$\begin{aligned} \Phi &= \sin^2(\delta) \cos(\theta_0) \sigma T^4 \\ \Phi &= 1367.62 \text{ W/m}^2 \end{aligned} \quad (5)$$

where δ is the apparent diameter for the mean anomaly, and θ_0 is zero. For comparison, the standard ASTM E-490 extraterrestrial spectrum is defined to have an integrated power of 1366.1 W/m^2 .⁴ Thus, even though the agreement is not exact, it is still very close especially considering the fact that the true solar output is not blackbody, and it varies by about 1% every 11 years [38]. Further analysis shows that the atmosphere also scatters and absorbs incoming sunlight which for all intent and purpose is completely random due to the unpredictable nature of our weather.

⁴ The most recent measurements from NASA's Solar Radiation and Climate Experiment (SORCE) have indicated the total solar irradiance during the 2008 solar minimum period at 1AU is actually closer to $1360.8 \pm \text{W/m}^2$ [40]. The previous higher recommended value in the 1990s was mostly due to scattered light entering the radiometer.

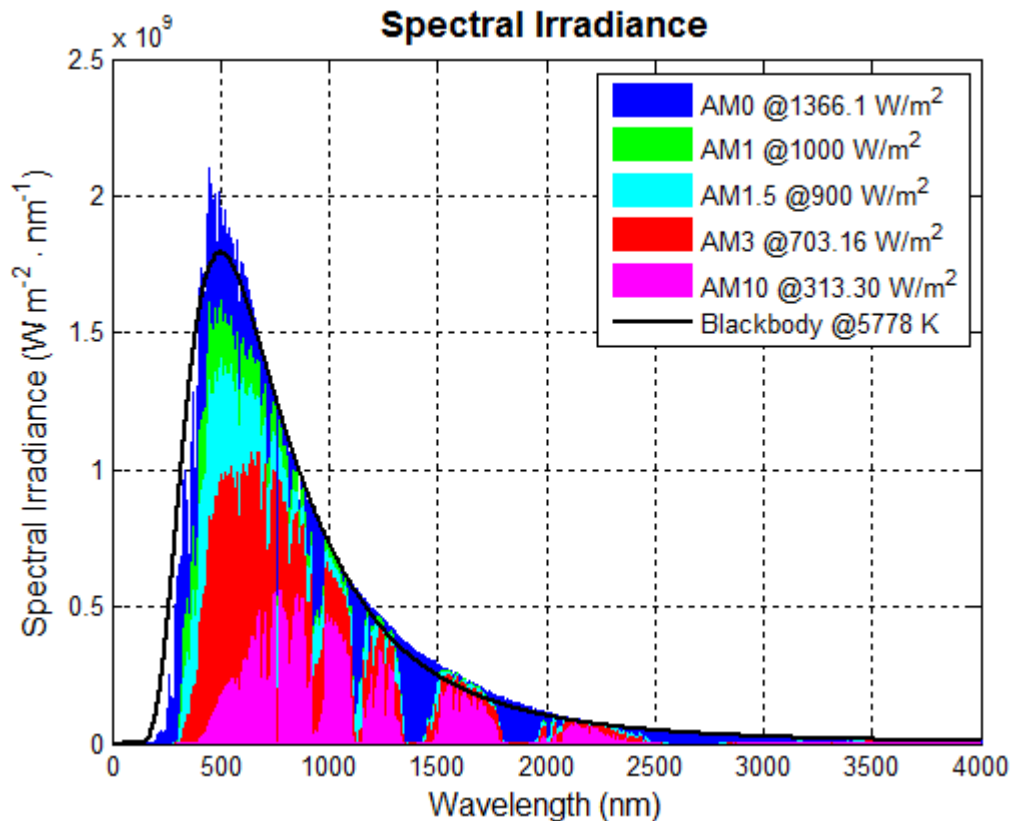


Figure 3.2 –An illustration of blackbody radiation and various standard solar spectra including the AM0 (ASTM E490) Extraterrestrial spectrum; the AM1.5 Global (ASTMG173); the AM1.5 Direct+Circumsolar (ASTMG173); and AM3 and AM10 spectra generated by SMARTS [41].

3.3 Atmospheric Effects

The atmosphere can have enormous effects on the performance of a CPV system to the point that it can make a CPV system economically viable in Spain for instance, but not Canada. In Figure 3.2, it was shown without explanation how the radiation spectrum from the Sun received here on Earth depends strongly on the state of the atmosphere. The degree of light absorption and scatter can most simply be described in terms of effective air mass. Although the description is not perfect, already from Figure 3.2 above, we can see that both the total irradiance and the spectral composition of the light changes. This is important to note, especially for multi-junction cells as the multiple bandgaps cause them to be more sensitive to spectral variations than single bandgap materials.

Although in space the Sun's disk shape ends quite abruptly, our atmosphere tends to scatter the light beyond these edges resulting in a broader disk shape with fading edges that depends on the current weather. Direct light is said to come from the solar disk and circumsolar radiation (CSR) between the Sun's disk and a 1° radius. The method of measuring the sunshape varies, but with the advent of digital cameras, a process developed by the German Aerospace

Center (DLR) has been used to capture sunshape images all across the globe. These images have been subjected to a statistical analysis and the results are shown in Figure 3.3.

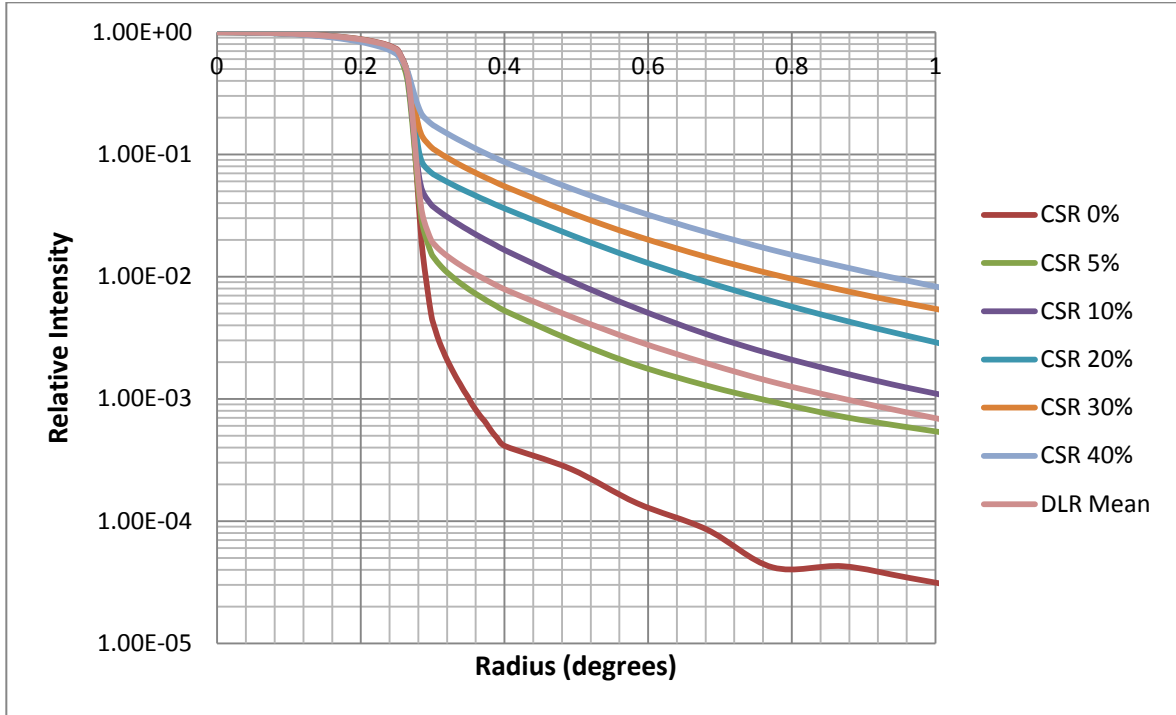


Figure 3.3 - Average sunshape profile[42].

The sunshape is important in practical CPV design as it tends to broaden the size of the source.

4 Tracking Systems

4.1 Why Track?

There are four main reasons for tracking:

- Increase collected power
- Better match between the daily production and demand curves
- Enable the use of concentrator optics
- Only way to approach the theoretical limit of efficiency

Although tracking does increase the collected power for any given PV area, one should also note that tracking decreases the land area usage efficiency due to shading issues. Another way of thinking about this is that a continuous, flat array will suffer *cosine losses*. However, a field of trackers will suffer from *shading losses*. However, cosine loss results in an average drop of flux over an evenly illuminated surface. Shading losses result in a constant irradiance on one surface but complete darkness in another. The difference is important because solar array performance deteriorates dramatically when only a portion of it is completely shaded. *Ceteris paribus* a continuous array will always be able to produce more power per unit land area than a field of tracking systems. But keep in mind that there is also an economic trade-off between land, which may be cheap, and the spacing between arrays, which are expensive. This is probably the most important reason why practical systems are almost never a continuous array.

In addition to capturing more energy per module, using a tracking system allows one to better match the daily demand cycle for electricity than fixed plate systems. Designers of flat plate systems usually find themselves at a junction deciding if the extra energy gained from the use of a tracker is worth the extra associated cost. Meeting the demand curve never enters into the equation as subsidy driven markets do not account for this. Since CPV systems require trackers, the decision is already made and thus both the increase in captured energy and better match to the demand curve is often pitched as an inherent benefit.

Tracking is a must for CPV systems and thus the only way very efficient, yet very expensive photovoltaic cells can be used in terrestrial applications.

The fourth reason for tracking has to do with the laws of thermodynamics which state that when two bodies exchange energy, in order for no entropy to be generated both bodies must reach thermodynamic equilibrium. That is, all the energy sent and received by each body must be equal. So, ideally if the cell's surface is Lambertian, the optics should be designed such that all the light emitted from a 90° cone is transformed to a narrow pencil of light directly towards the Sun. The result is that the acceptance angle of the system must be minimized which necessitates the use of trackers.

It is also important to note that a *tracker* does not necessarily have to mechanically change the orientation of a solar panel. Rather, a tracker is anything that changes the direction from which light must enter into the system to be incident on the receiver. As an example, an appropriate change in a material's index of refraction could serve as a tracker.

4.2 Traditional Tracking System Designs

Due to the Earth's obliquity with respect to the ecliptic, the diurnal and seasonal movements impose certain requirements on different combinations of solar collectors and solar tracking devices. The diversity of requirements that solar collectors has led to such a wide variety of different tracking methods that no clear cut classification system is possible.

For the highest concentrations, $C > 500$, the required tracking accuracy is usually below 0.1° , but some concentrators may allow a tolerance up to around 1° [43].

A considerable amount of cost is associated with the tracker portion of the CPV system, the largest of which is the steel used to support it. R&D efforts aim at optimizing the construction with respect to size, stability, load-capacity, material consumption and stiffness [43]. According to the European research strategy plan, cost targets for trackers are around 100 to 150 \$(2006)/m² by 2013 [43].

Figure 4.1 shows four very common tracking configurations. They are a) a tracking pedestal which tracks the Sun by pivoting an array about a central point; b) a tilt roll system which is aligned towards the equator, following diurnal motion through the tilt axis and seasonal motion through the roll motion; c) a carousel which follows the Sun through appropriate combinations of rotation through the elevation axis and azimuth axis; and lastly d) a louvered tracking system, which is like the tilt roll system but mounted differently.

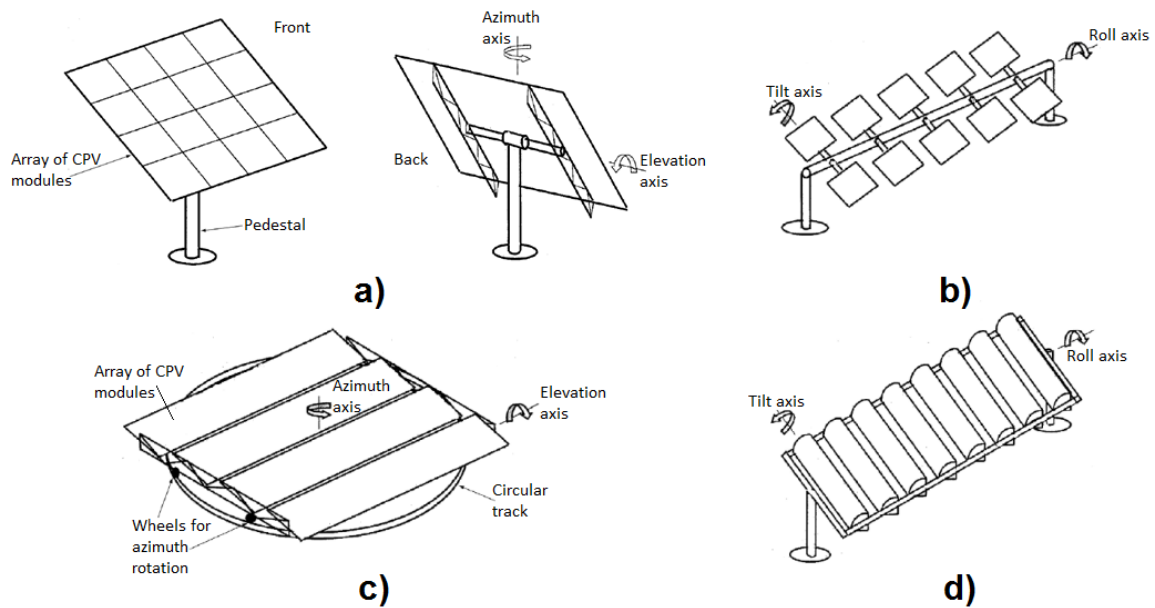


Figure 4.1 - Tracking schemes a) a pedestal tracker; b) a tilt roll tracker; c) a carousel tracker; d) a louvered tracking system (adapted from [44]).

Other common forms of tracking use a field of heliostats which generally aim to reflect light towards a central receiver rather than maintain a fixed alignment of the optical system with respect to the Sun.

Pedestal trackers are quite common as they offer reasonable tracking accuracy and a low land footprint. However, because the array rests on a central pivot, they are susceptible to flexing in windy conditions and under their own weight.

Carousel trackers are more rigid structures than pedestal trackers but they also have a larger land footprint. The TITAN tracker is an example of a large carousel tracker with a tracking accuracy of 0.01° . Such a system is especially required for a central receiver solar system because of the tracking accuracies required for mirrors on the perimeter of the heliostat field.

Both the tilt-roll and louvered system are very similar. Later, it shall be shown how off-angle tracking is also very similar as it uses the same tilt axis to follow the diurnal motion of the Sun. The difference is that the roll axis is replaced by an internal tracker that rotates about the normal of the collector.

4.3 Control System

Control systems for trackers play a large role in the overall accuracy of the system. There are generally three approaches. The first is an open loop system where a computer uses a preprogrammed path of the Sun to follow. This approach is fine when low accuracy is needed because the Sun follows a simple path which can be easily programmed. However, to account

for the small deviations from this path in high accuracy CPV systems, more complicated algorithms are needed. Another problem is the presence of systematic and statistical errors in initial alignment techniques and mechanical motion that cannot sufficiently be accounted for with this approach.

Another method is closed loop systems. The problem with these is that the tracker does not work if there is temporary cloud cover.

Usually, the most useful system is a combination of open loop and closed loop systems. This allows the tracker to roughly track the Sun in all conditions, while The negative feedback system accommodates for small perturbations caused by initial alignment errors, drift, and other factors.

4.4 Tracker Accuracy

Any practical concentrator will inevitably be manufactured with some level of imperfection. Assembling an array of concentrators, cells and other components will also result in some level of imperfection. All of these imperfections can be controlled within a certain tolerance but with a certain cost. That is, the tighter the tolerance the higher the cost.

In CPV, this nonimaging optics finds its application in the design of a small number of simple components that simultaneously allow for high concentration and generous manufacturing and alignment tolerances. In other words, unlike imaging optics which requires that an image be formed, nonimaging optics only aims to deliver radiant energy in the most thermodynamically efficient manner.

Why reach the thermodynamic limit? When a concentrator is thermodynamically efficient, its acceptance angle is maximized for a given level of geometric concentration. Figure 4.2 illustrates why maximizing the design acceptance angle is important for reducing the system cost through increased manufacturing tolerances and reduced tracking accuracy requirements.

Tolerance budget distribution

Example: Design acceptance half-angle $\alpha = 1$ deg

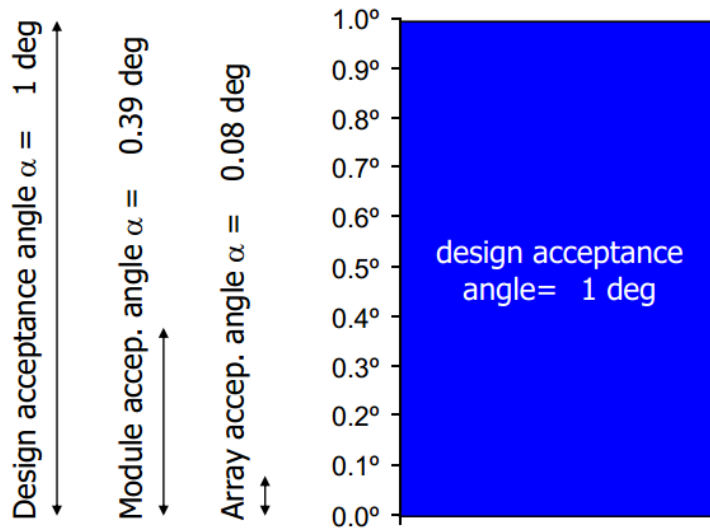


Figure 4.2 - From a LPI presentation [45].

Although tracking accuracy has been reported at least back to 1988 at the Sandia National Laboratory [46], it should also be noted that currently, there is no standard method of determining the tracking accuracy for industrial trackers [47]. Apparently, CPV developers overlook this issue and claim high tracking accuracies without any explanation as to how this number was obtained.

Despite this problem, progress in tracking accuracy measurement has been made. For example, a group in Madrid, Spain developed and patented a tool used to measure the precision at which a sun tracker can follow the sun, as seen in Figure 4.3 [48][49][50].



Figure 4.3 - A tracking accuracy sensor mounted on one of Inspira’s CPV lab tracker [50].

An Italian organization called the ENEA (Italian National Agency for New Technologies, Energy and Sustainable Economical Development) is responsible for the development of another instrument intended to measure solar tracker accuracy [51]. Another example of a device to measure tracking accuracy is the “Trac-Stat SL1” device from GreenMountain Engineering [52].

4.4.1 Tracker Fluctuation and Acceptance Angle Analysis

The acceptance angle of a solar module can be thought of as the tolerance for statistical fluctuation in the alignment of the module with respect to the sun. If the acceptance angle distribution, $\psi(x)$, is for example one degree, we have,

$$\psi(x) = \begin{cases} 1 & -1^\circ < x < 1^\circ \\ 0 & \text{otherwise} \end{cases} \quad (6)$$

The statistical fluctuation distribution of the module alignment, $\phi(x)$, is assumed to be normal with a mean of zero. Thus, we can write,

$$\phi(x) = \frac{1}{\sqrt{2\pi\sigma^2}} \exp\left(-\frac{x^2}{2\sigma^2}\right) \quad (7)$$

If for example, we consider a standard deviation of 1° and 0.5° , the resulting area of the distribution that remains within the acceptance angle is 95.4% and 68.3% respectively. This can be found by integration of the product of the angular acceptance distribution with the statistical fluctuation distribution, and then integration over their angular extent.

$$\int \psi(x)\phi(x) dx \quad (8)$$

This is illustrated graphically in Figure 4.4.

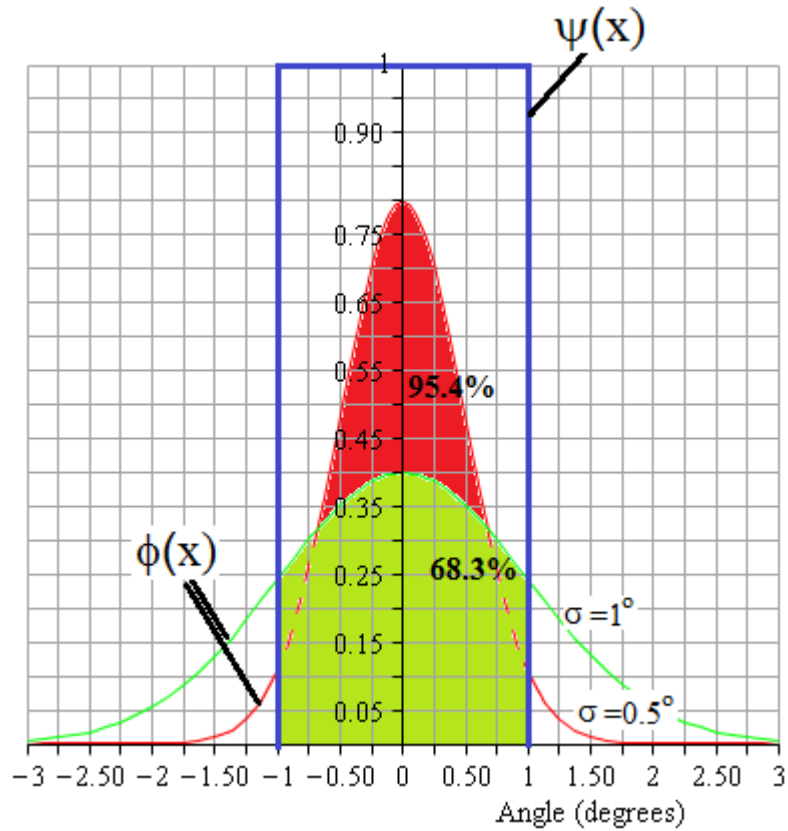


Figure 4.4 – Illustration of the folding concept.

Note that $\psi(x)$ is not necessarily piecewise continuous or symmetrical. But, assuming a piecewise continuous function yields a relatively simple result. Consider a Gaussian distribution with a mean of zero, which is given by Equation (7).

We shall assume that the acceptance distribution has a value of unity over an acceptance angle of a .

$$\phi(x) = \begin{cases} 1 & -a < x < a \\ 0 & \text{otherwise} \end{cases} \quad (9)$$

Now, folding ϕ with ψ as in (8), we obtain,

$$\begin{aligned} & \int \psi(x)\phi(x) dx & (10) \\ &= \frac{1}{\sqrt{2\pi\sigma^2}} \int \exp\left(-\frac{x^2}{2\sigma^2}\right) dx \\ &= \text{erf}\left(\frac{a}{\sqrt{2}\sigma}\right) \end{aligned}$$

This result will be assigned to a value called the system efficiency or performance, Eff_{sys} .

$$Eff_{sys} = \operatorname{erf}\left(\frac{a}{\sqrt{2}\sigma}\right) \quad (11)$$

Figure 4.5 shows a contour plot of Equation (11) with respect to the acceptance angle and standard deviation. Each contour line represents the linear relationship between the acceptance angle and standard deviation for a given system performance. There are no guidelines regarding what an acceptable performance level is. That being said, whenever an acceptance angle is stated one must be careful in the interpretation.

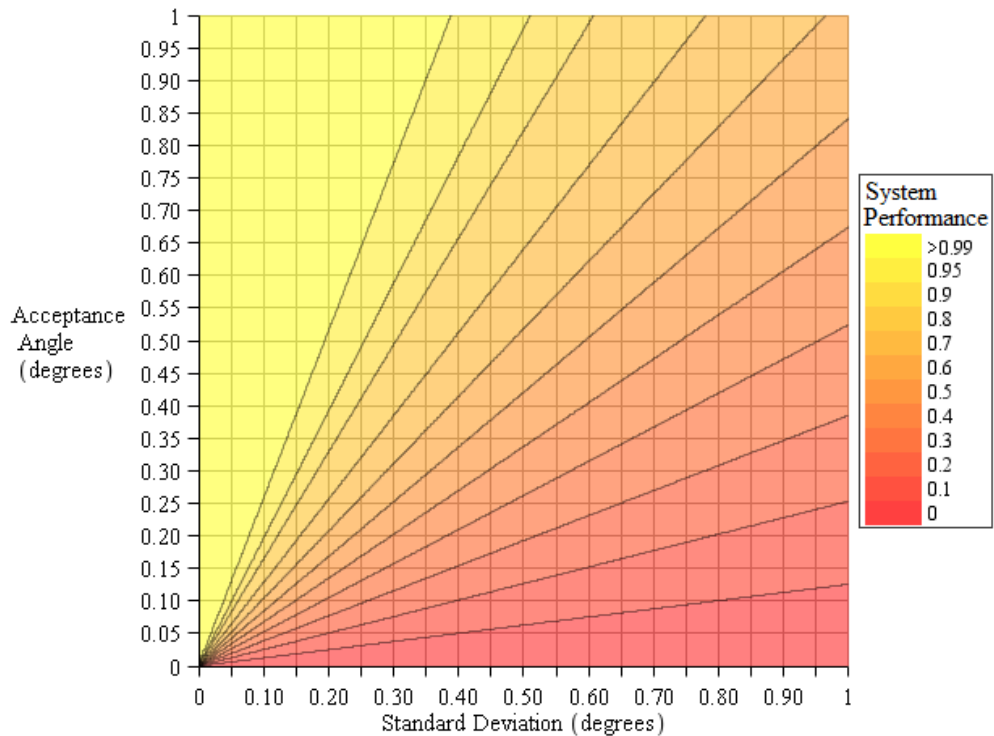


Figure 4.5 - System performance as a function of acceptance angle and standard deviation.

If the system performance is held constant, then it is obvious that Equation (11) shows that the standard deviation and acceptance angle are proportional to each other, which is shown by the linear curves in Figure 4.5. Multiplying each axis by the same scaling factor will allow one to extend the effective range the chart describes. For example, multiplying both axes in Figure 4.5 by five will extend the angular range to five degrees.

4.5 Less Conventional Tracking

There are many different ways of tracking the Sun, most of which require some form of mechanical motion. Some *nonconventional* tracking concepts and actual implementations are described here along with some of their strengths and the weaknesses that off-angle tracking attempts to address.

Campbell and Machado show one tracking method is to use two concentrators that rotate independently about the same axis of rotation in a way similar to the way Risley prisms rotate on the same axis, often to steer laser beams [53]. In this case the concentrators both concentrate and steer light towards a receiver.

Bijl and Peter use a similar method for tracking as Campbell and Machado, but with a catadioptric optical system [54].

Tomonori *et al.* describe a method of moving a receiver laterally within a plane so that as the sun moves across the sky, the cell follows the changing position of the focused image [55].

Duerr *et al.* describe an integrated concentrator and tracking system which moves both the receiver and lenses laterally within a plane [56]. As with the design from Tomonori *et al.* [55], this has some advantageous, but it still requires more degrees of freedom than necessary to always track the sun's motion in the sky. There is only a brief mention of the use of lateral tracking in combination with single axis tracking [56], which is elaborated on in a presentation [57].

Kotsidas, Modi, and Gordon describes a system where gradient index (GRIN) optics are moved by a small amount along the x, y, and z axis in order to bring an array of them to focus light onto an array of receivers [58],[59]. Again, there are more degrees of freedom than necessary.

Benitez *et al.* illustrate a typical approach to how one may create a low profile tracking system [60]. This essentially consists of replacing one large tracker with many smaller ones.

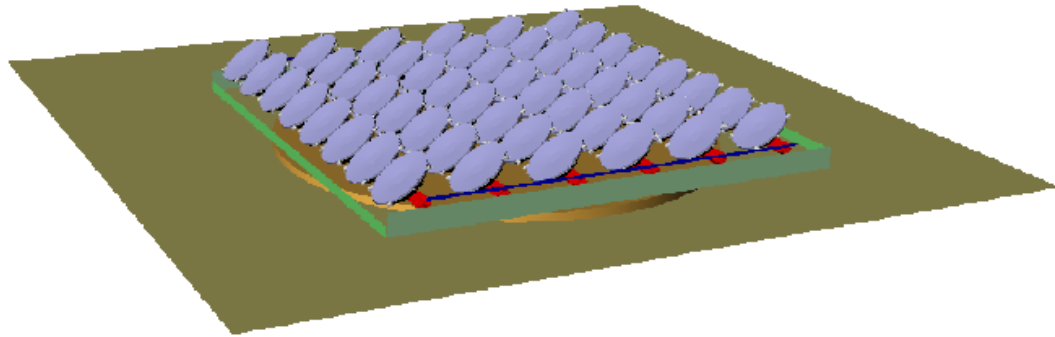


Figure 4.6 - Illustration of a low profile rooftop tracker with kohler integration and mirrors [60].

Tomlinson also describes a method of positioning a plurality of concentrator modules which focus light onto a receiver in a way that allows for the system as a whole to maintain a low profile on a rooftop [61]. The claimed advantage of this system is that it uses a set of optical components designed to receive light at an angle offset from the normal of the surface. The purpose of these elements is to reduce or eliminate the need for polar axis alignment.

Winston and Zhang describe a tracking receiver that utilizes a hemispherical mirror [62]. A major disadvantage is severe aberrations from non-paraxial rays which cause nonuniform illumination [63].

Kritchman describes a fixed, linear convex Fresnel lens with a moving receiver to track the sun as it moves across the sky [64]. Unfortunately, the sun moves over a large portion of the sky and due to a lack of symmetry in the system, large aberrations are inevitable when the sun is in a certain positions.

Bachmaier, *et al* describe a method of making fine adjustments to the receiver to compensate for misalignment in the optical system [65].

One patent [66] describes a method of capturing light using a dimpled planar waveguide. The economic motivation behind this idea was that this system would use roll-to-roll processing to make it cost competitive [67], [68]. The dimples serve as lenses which focus the beam onto a facet which steers the light to become coupled into the light guide. It is possible to move all of these facets laterally so that the sun may be focused over a wide range of angles. However, this method of tracking has only been demonstrated to capture up to 65% of incident energy at 125x concentration, and up to 75% of incident energy when mounted on a polar axis tracker [69].

As with all waveguides, there are absorption issues altering the solar spectrum and possibly having adverse effects on the performance of the solar cell. The lack of symmetry

through the course of the year also reduces the ultimate concentration ratio that can be achieved.

A proposed extension of this waveguide design is in the use of active materials which allow the index of refraction to change in such a way that can replace the mechanical motion of a tracking system [70]. However, such designs are concepts that have yet to be proven commercially viable.

Brunotte, Goetzberger, and Blieske describe a method that utilizes a one-axis tracker to follow the diurnal movement of the sun [71]. Mohr *et al.* also describe a similar system [72]. The basic idea is to exceed the concentration of 2D concentrators on single axis trackers by also making use of the limited divergence of the sun's seasonal motion.

Bouchard and Thibault [73] proposed a planar waveguide system which replaces the spherical micro lens array from the planar dimple waveguide system for a cylindrical micro lens array. Because the focus is a line instead of a point, it is possible to use just seasonal tracking instead of two axis tracking. The claim is that in addition to bringing down the cost, it may also make rooftop applications feasible.

Passive systems may offer cost advantages because they do not require power and they do not have the added cost of fitting and maintaining the control system and motor [74]. However, one disadvantage is that they do not work very well in cloudy weather and it may be difficult to reposition them every morning [74]. Figure 4.7 illustrates an interesting passive tracker that utilizes actuators which convert light directly into mechanical energy, mimicking the way some plants follow the Sun [75].

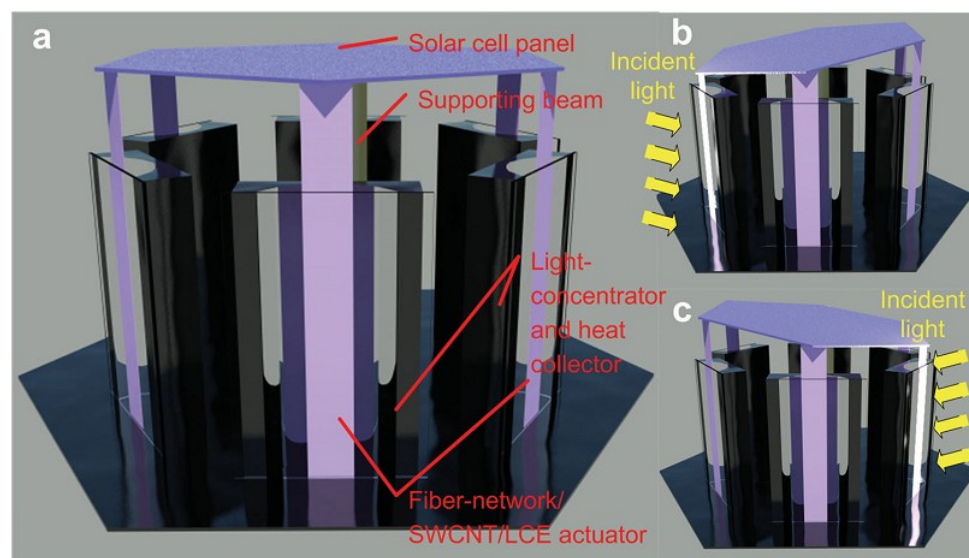


Figure 4.7 – Concept of artificial heliotropism [75].

Another interesting solar tracker concept uses a flexible pole surrounded by a material that expands when wet and contracts when dry [76]. A sponge is a common example of such a material. If these trackers are placed on a floating platform within a pool of water, the sponge like material can then be allowed to draw up water via capillary action.

Two hemispherical dielectric halves can be bonded together and suspended in a fluid. By applying an electric field at different regions relative to the sphere, it can be made to rotate. One can utilize this concept to create a thin film embedded with rotatable mirrors that can direct light to a central receiver [77], [78].

5 Off-angle Tracking Theory

5.1 Introduction

To appreciate how the concept of off-angle tracking applies to solar tracking, it is easiest to first break down the basic motion of the Sun. To a good approximation, the Sun appears to circle the Earth every day; and those circular paths appear to be slightly higher or lower in the sky depending on what day of the year it is. More precisely, the Sun's diurnal motion is nearly circular, moving across the sky at a rate of 1° every four minutes. The declination of the Sun ranges from about -23.44° to $+23.44^\circ$, and so over the course of a year the Sun's seasonal motion is about $46.88^\circ/365=0.13^\circ$ per day on average.

In order to achieve 500-1000x concentration, which is necessary to make the use of multi-junction cells in terrestrial applications, the acceptance angle of the optical system used to focus the light is limited to about 1° . Taking into account various other tolerances, such as in manufacturing the lens surface and assembling the module, it has been found that in general trackers require at least 0.1° tracking accuracy for the system to operate reliably. Another way of looking at it is that the tracking accuracy required for CPV systems is about the same magnitude as the Sun's seasonal motion per day.

The off-angle tracking concept is intended exploit the fact that the maximum extent of the Sun's declination is about 23.44° from the equinox. The cosine of 23.44° is about 0.92, which means that if a surface were to be aligned at an angle of 23.44° with respect to the Sun, then the resulting cosine loss would only be about 8%. For a conventional, polar aligned single axis tracker, this means that at the spring and fall equinox, there is no cosine loss when following the diurnal motion of the Sun. However, at the summer and winter solstice, there is approximately an 8% cosine loss when following the diurnal motion of the Sun. Thus, the cosine loss changes throughout the year.

It can be shown using trigonometry that it is possible to follow the diurnal motion of the Sun with a polar aligned, single axis tracker such that the angle between the collector's surface normal and the Sun is always 23.44° . This results in a constant cosine loss of 8% throughout the entire year. The benefit is that one can take advantage of the resulting rotational symmetry in the design of an optical system which utilizes an internal tracking system to follow the Sun's seasonal motion.

It is not possible to simultaneously maintain an angle between the collector's surface normal and the Sun is less than 23.44° and track the Sun for the entire year. This is due to the obliquity of Earth discussed in Chapter 3. A trade-off between cosine losses and tolerance in the alignment with the Celestial pole arises when fixing the angle between the collector's surface normal and the position of the Sun.

An example of such an optical design is shown below in Figure 5.1 which shows how light is initially focused off of the optical axis onto a mirror. Subsequent reflections off of the outer mirror and then inner mirror focus the light back onto the optical axis. The thing to notice is that the two mirrors may rotate about the optical axis in such a way that allows it to focus light incident at any orientation about the optical axis, so long as it makes an angle of 23.44° with respect to the optical axis.

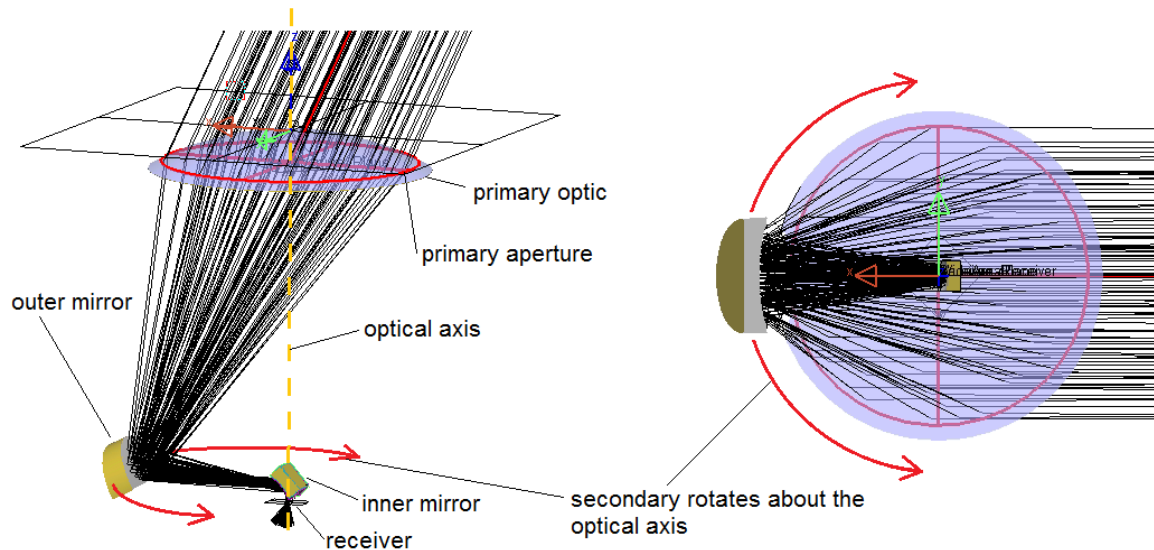


Figure 5.1 - Example of an optical design that focuses light incident at a 23.44° angle with respect to the normal of the primary optic.

In general, off angle tracking would theoretically be able to reach the thermodynamic limit of concentration. Practically, the module for off-angle tracking will require about 8% more material than an on axis module that captures the same amount of energy. This is because the normal of the module's surface is designed to be at an angle of about 23.44° with respect to the sun.

5.2 2D Theoretical Limits

5.2.1 Cosine Loss

One of the most important aspects of off-angle tracking is the cosine loss. This does not imply that the performance of off-angle tracking is inherently worse than on-axis concentrators. Rather, it means that the primary aperture of the concentrator must be larger to achieve the same throughput as on-axis concentrators. The confusion arises from the fact that traditionally, geometric concentration is defined as the ratio of the input aperture area over the receiver area. The definition of the input aperture area is straightforward to define for on-axis concentrators. However given the novelty of off-axis trackers there is no formal definition of geometric concentration.

Consider how blackbody radiation from a spherical surface is incident on a flat Lambertian surface. It can be shown that the flux on the Lambertian surface is given by,

$$\Phi = \sin^2(\delta) \cos(\theta_0) \sigma T^4$$

Clearly, the flux drops off in proportion to the cosine of the angle between the position of the sphere and the normal of the surface.

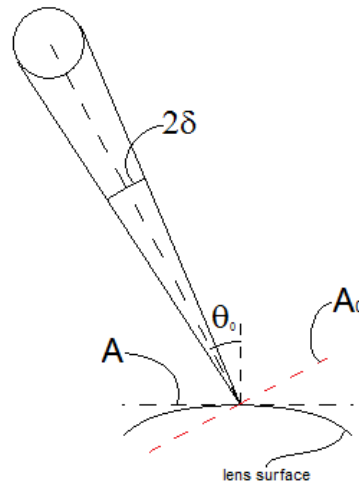


Figure 5.2 - Illustration of cosine loss.

From this perspective, the reduced irradiance on the primary aperture of a concentrating system could be viewed as a loss when compared to an on-axis concentrating system. In reality, this “loss” really poses no constraint on the thermodynamic efficiency that the system can achieve when compared to on-axis trackers.

This idea can be more clearly understood by considering 2D GRIN lenses as seen in Figure 5.3 below. Due to the symmetry of GRIN lenses, we can conclude that the thermodynamic efficiency of the lens is the same no matter what direction light from a sphere is coming from. Two interpretations now become apparent. The first is that the cosine loss is from the projection of light from the sphere on an aperture with length A .

The second interpretation is that there is no cosine loss because the light from the sphere is normally incident on an aperture with length A_0 , equal to the projected length of A . In this case, the base of the apertures with length A_0 are spaced at intervals of an amount equal to A in order to avoid self shading. The net result is that in order to take advantage of the symmetry that arises from off-angle tracking, the aperture must be larger than that of an equivalent on-axis concentrator by an amount proportional to $1/\cos(\theta)$.

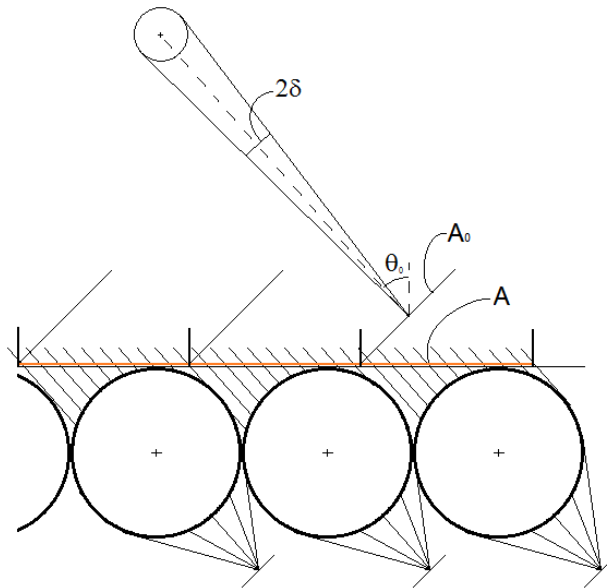


Figure 5.3 - Cosine loss for adjacent GRIN lenses; A is the conventional definition of the aperture size (or in this 2D case, length), A_0 is the projection of A , δ is the angle the source subtends, and θ_0 is the angle the source makes with respect to A .

5.2.2 Limitations of Different Optical Configurations

If the cell is tilted with respect to the back plane of the module, then the cell must be reoriented with respect to the optical axis to maintain symmetry, as illustrated below. In such a case, the most efficient method of positioning the cell would be to rotate each one individually about the optical axis of the lens which is illuminating it.

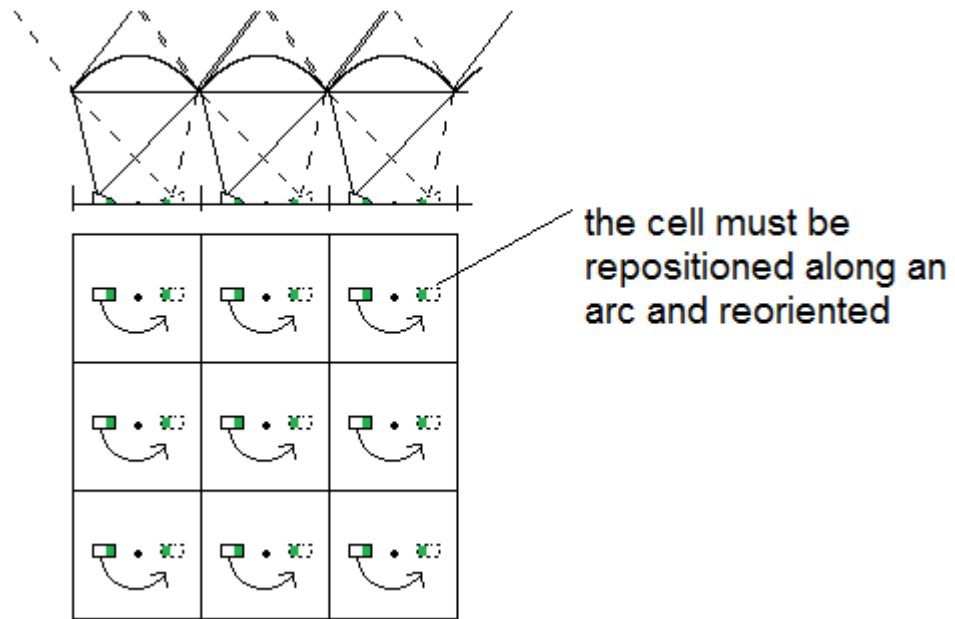


Figure 5.4 – Single lens and tilted receiver configuration.

If the cell is positioned to be parallel with the back plane of the module, then it is not necessary that the cell be reoriented.

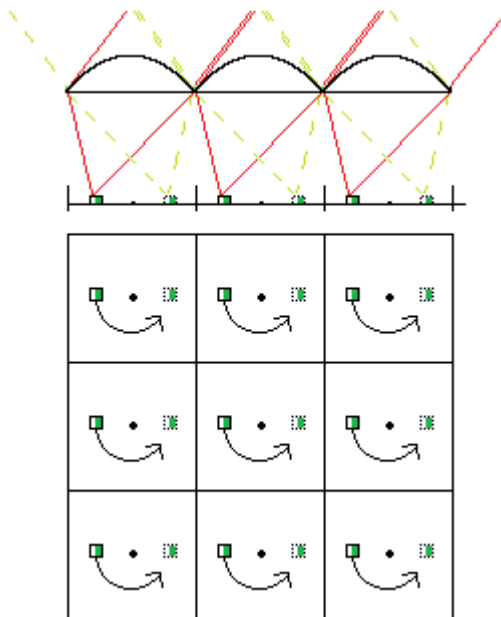


Figure 5.5 – Single lens and flat receiver configuration.

Because only x-y motion is required, it is possible to move all cells simultaneously with only two actuators, one for the x-direction and one for the y-direction. One caveat of this

strategy is that so long as the receiver is located off the optical axis, then the required acceptance angle of any secondary optic that is rotationally symmetric about the normal of the back plane will be larger than what is required for the system to be thermodynamically efficient. This can clearly be seen in Figure 5.6 which illustrates the alignment for a beam incident from the right (red) and the beam incident from the left (green) to both be captured by the secondary optic. Thus, at any given moment only a fraction of the secondary optic's étendue is filled.

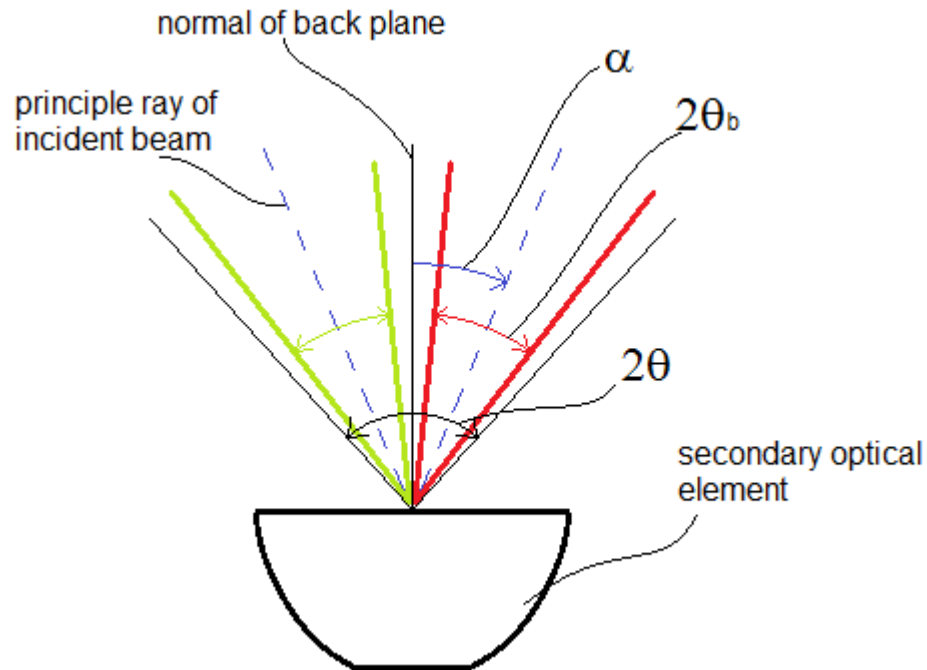


Figure 5.6 - Illustration of the relationship between the acceptance angle of a secondary optical element that is rotationally symmetric about the normal of the back plane and the étendue of the incident beam from the primary optical element.

There are two solutions to fixing this problem. The first strategy is to introduce a hole in the acceptance angle of the secondary optic. However, this strategy only partially fixes the problem as the étendue of the secondary optic is only partially filled at any given time.

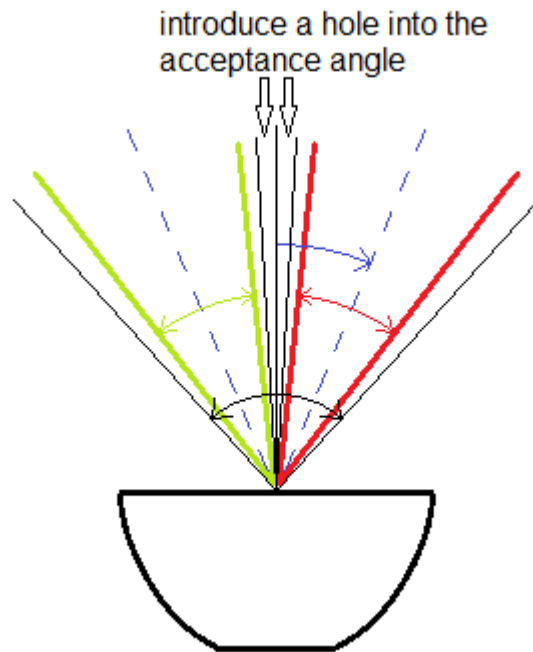


Figure 5.7 - Illustration of how a hole would be introduced into the secondary optic.

A second strategy is to steer the light so that the principle ray is parallel with the optical axis. The reason is that unless that cosine space of the incident light is rotationally symmetric about the optical axis, then a rotationally symmetric secondary will not be able to focus the light optimally.

Figure 5.8 illustrates how making the beam perpendicular to the back plane of the module will allow for the secondary optic to have a very limited acceptance angle, thus allowing the optical design to come closer to the étendue limit.

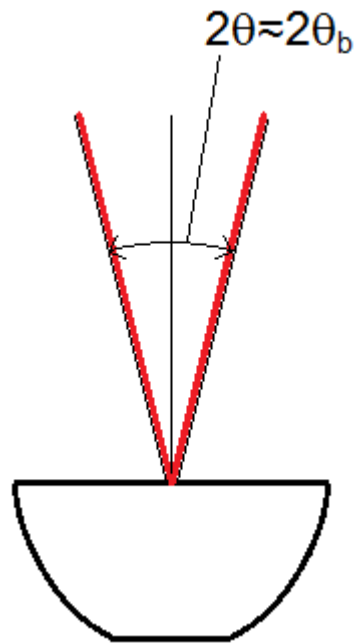


Figure 5.8 - Illustration of how an incident beam with a principle ray that is mainly normal to the back plane is able to focus onto a rotationally symmetric secondary optical element (or receiver); note that the acceptance angle is actually larger than the solid angle that the beam subtends in order to allow for some alignment tolerance.

Figure 5.9 illustrates how a refractive ring could at least bring the tangential rays of the beam into focus onto the receiver. The beam would mainly be perpendicular to the back plane, however experience has shown that because of the restriction in the rotational symmetry of the ring, the severe astigmatism which arises from focusing off axis with the primary optic is not easily corrected. This is also true in reflective optics with rotational symmetry about the optical axis. In either case, the restriction would ultimately prevent the design from reaching the thermodynamic concentration limit.

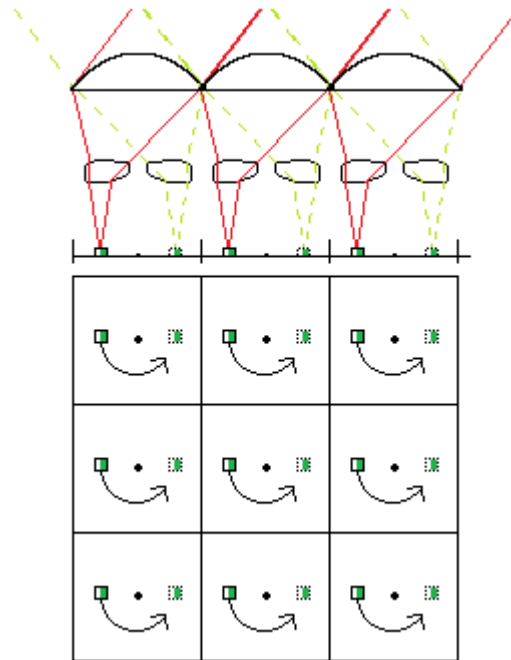


Figure 5.9 - Beam steering with a refractive ring.

Another implementation of the off-angle tracking concept is similar to that of Duerr *et al.* [56], [79]. It utilizes two lenses which are convex plano and plano convex. The mechanical motion that results from such a design is illustrated below. Clearly, the design would be much more simplified if the secondary lens were to focus along its own optical axis.

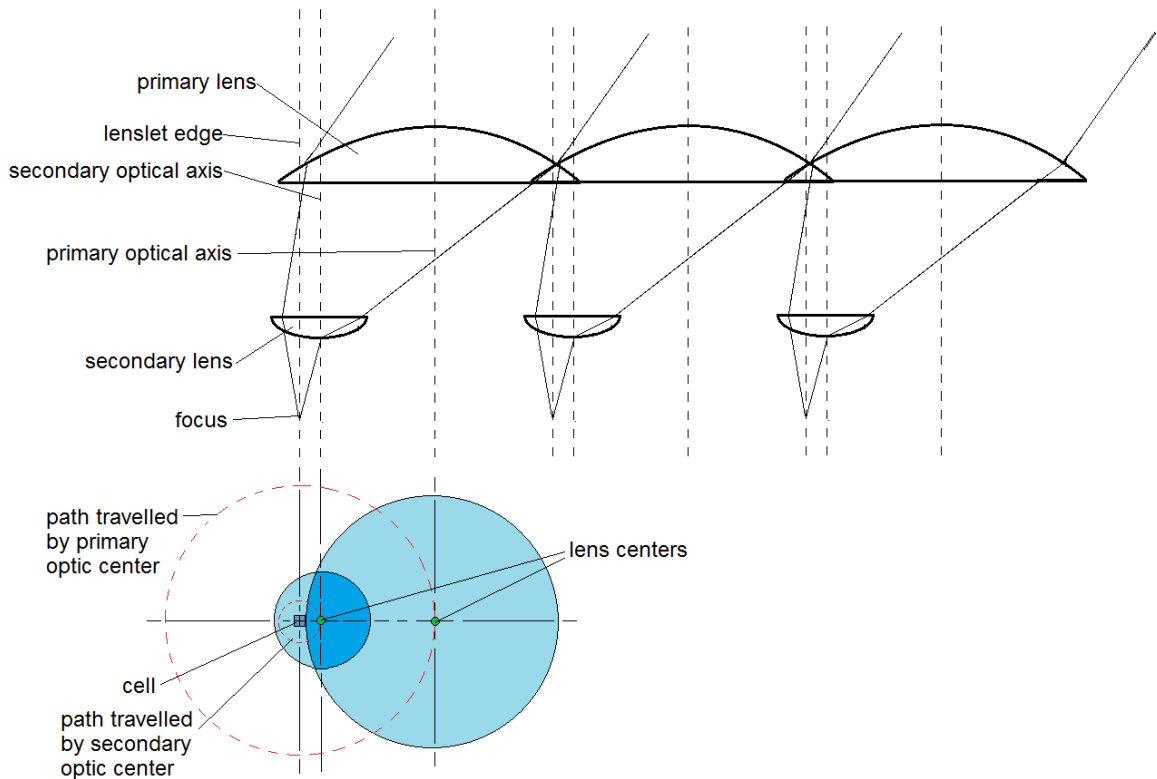


Figure 5.10 - Illustration of a convex-plano, and plano-convex lens configuration.

Another strategy would be to bring the beam back to the central optical axis. This can be done using different optical configurations. However, one particularly effective configuration may be to use two small freeform mirrors. This would likely allow enough degrees of freedom to both bring the beam back towards the optical axis and compensate for the astigmatism generated by the primary optic.

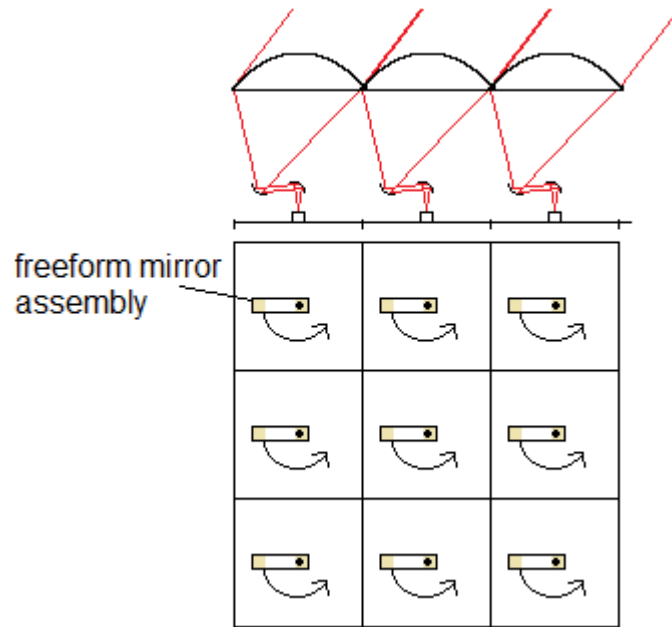


Figure 5.11 - Secondary optic which brings off-axis beam back on axis.

5.3 GRIN Lenses

Although the lens configurations shown so far do not make it obvious how the theoretical concentration limit would be achieved with an off-angle tracker, this does become obvious when looking at the properties of GRIN lenses. If we consider a Luneburg lens as seen in Figure 5.12, it becomes obvious that if the receiver were to be placed on a small fraction of the spherical cap that the Luneburg lens focuses onto, then it would be very straightforward to introduce the simple rotations that correspond to the requirements for off-angle tracking.

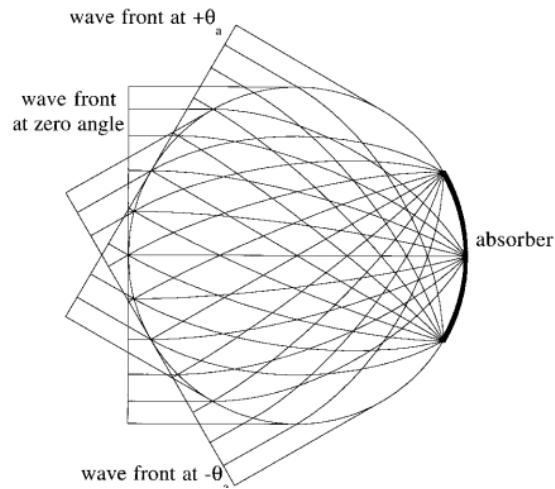


Figure 5.12 – Illustration of the Luneburg lens as a radiation concentrator from an extended far-field source of angular extent $2\theta_a$ onto a spherical-cap absorber (of arc length $2\theta_a$ in cross section). The three wave fronts are at the two extreme angles plus a nominal incidence angle of angle zero. [80].

Another, example that does not achieve perfect concentration, but very near to perfect concentration, is shown in Figure 5.13. In this case, the spherical cap that the lens focuses onto is located significantly beyond the lens itself.

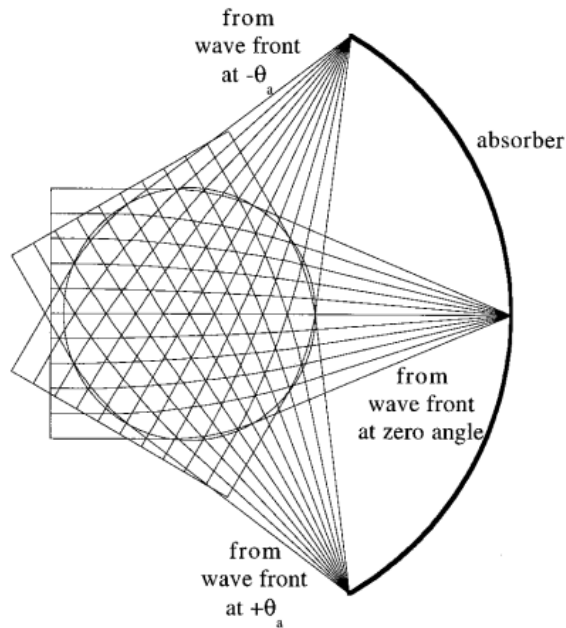


Figure 5.13 – Spherical gradient-index lenses as radiation concentrators illustrated for an incident extended far-field source of angular extent $2\theta_a$ (in analogy to the Luneburg lens, $r_1 = 1$). The three wave fronts are traced at the two extreme angles plus a nominal incidence angle of zero. $R_1 = 2.55$ (r_1 greater than unity), also corresponding to the fish-eye lens [80].

The most significant problem with GRIN lenses is the ability to manufacture them. It is currently possible to vary the index of refraction continuously over a range of about 0.3. By introducing discontinuities into the GRIN lens design, it is theoretically possible to create a GRIN lens with a homogenous core and a gradient index of refraction varying radially outward from the core [58][81]. This design has been worked out, at least in theory, but work on a demonstrated prototype has yet to be published. A PCT was filed in 2012 regarding this newly invented design [59].

5.4 Adjacent Trackers

Self shading of adjacent trackers is a problem in all CPV systems. However, the problem is a bit different in off-angle trackers. The issue is best illustrated by considering how two adjacent trackers will shade each other when approaching the horizon under different tracking configurations.

Below, we have an illustration of two different tracking configurations which follow the hypothetical Sun approaching the horizon. Clearly, one tracking configuration requires more limited diurnal motion than the other. The shading of such a configuration is also complicated by the fact that the module has thickness. Obviously, the thinner the module, the less shading there is when in the configuration given by solution 2.

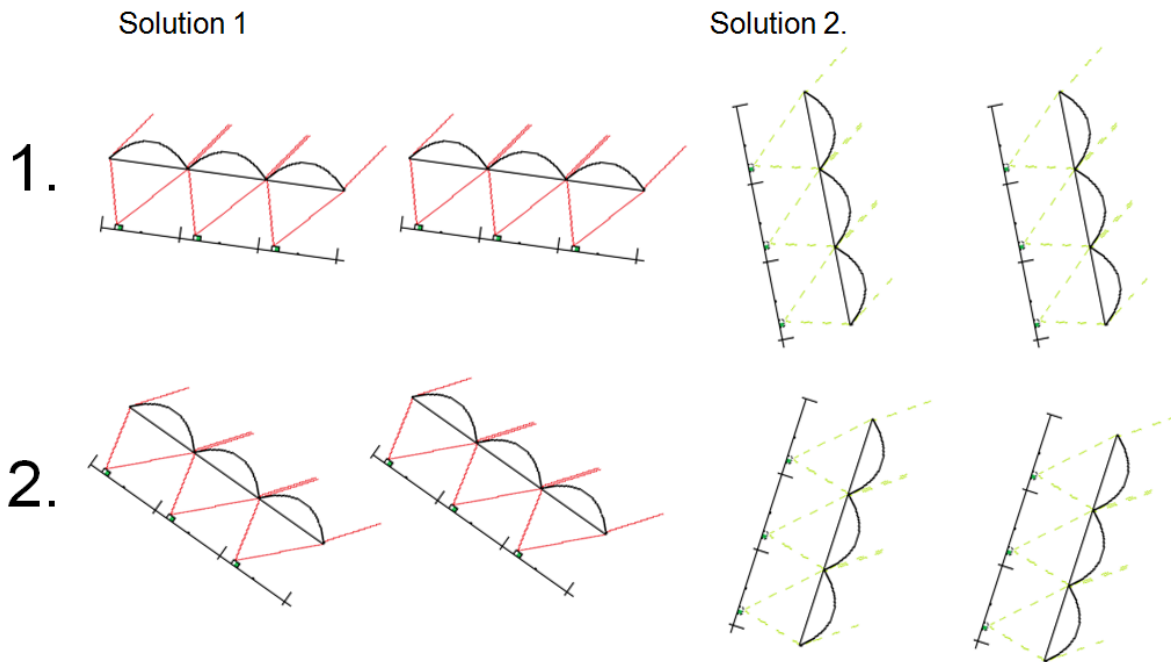


Figure 5.14 – Self shading of adjacent trackers under different tracking configurations.

Given that the shading is influenced by both the module thickness and the choice between two solutions, finding the optimal configuration of the system becomes more difficult.

It might be the case that the optimal design would require that the system move from one solution to the other on a daily basis. The result is that there would be a daily interruption in the system's power output as it temporarily stops harvesting energy to allow for the system to move from one configuration to the other. The difference between a daily transition configuration and a no transition configuration can easily be explained by looking at Figure 5.15 and Figure 5.16 below.

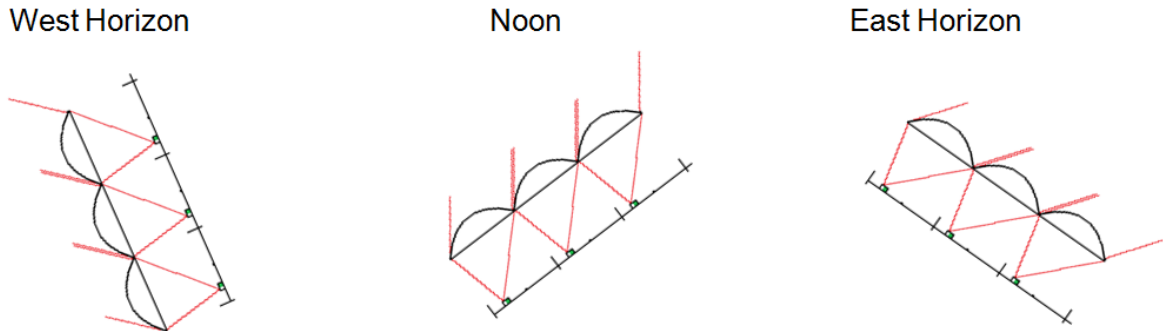


Figure 5.15 - Diurnal tracking without a daily transition.

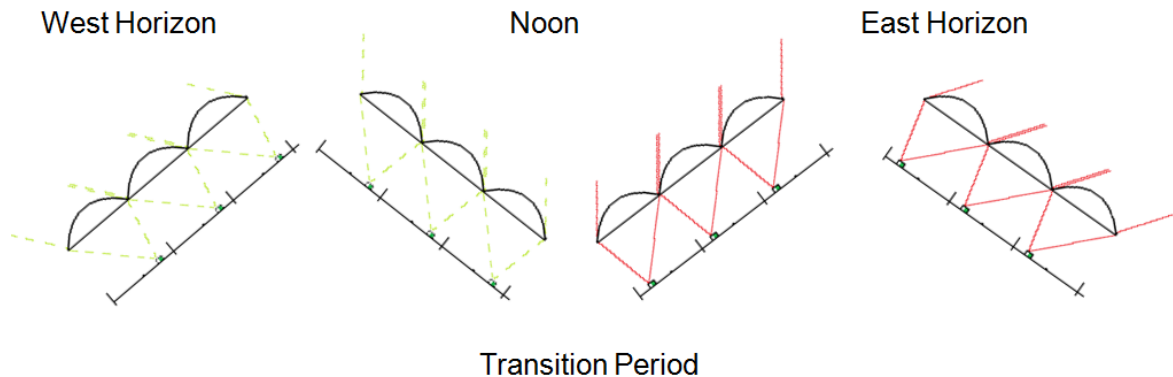


Figure 5.16 - Diurnal tracking with a daily transition.

5.5 Off-Angle Tracking Derivation

Before deriving a mathematical representation of off-angle tracking, a reference frame needs to be established. It also seems logical to treat the derivation as an extension to conventional tracking. Analytical expressions of conventional tracking can already be found in the literature, [82]–[84], but in this work, the notation is most similar to [82].

Conventional tilt-roll trackers can be described quite simply within the collector reference frame which is defined by the horizontal axis, H , the reference axis, R , and the vertical axis, V . As seen in Figure 5.17, the collector reference frame is oriented such that the vertical axis it is both aligned with the Earth's axis of rotation and points towards the celestial north pole; the horizontal axis points westward; and the reference axis is orthogonal to them both.

The result is that the angle of V with respect to the zenith is approximately $\pi/2$ minus the latitude of the collector reference frame's location on Earth.

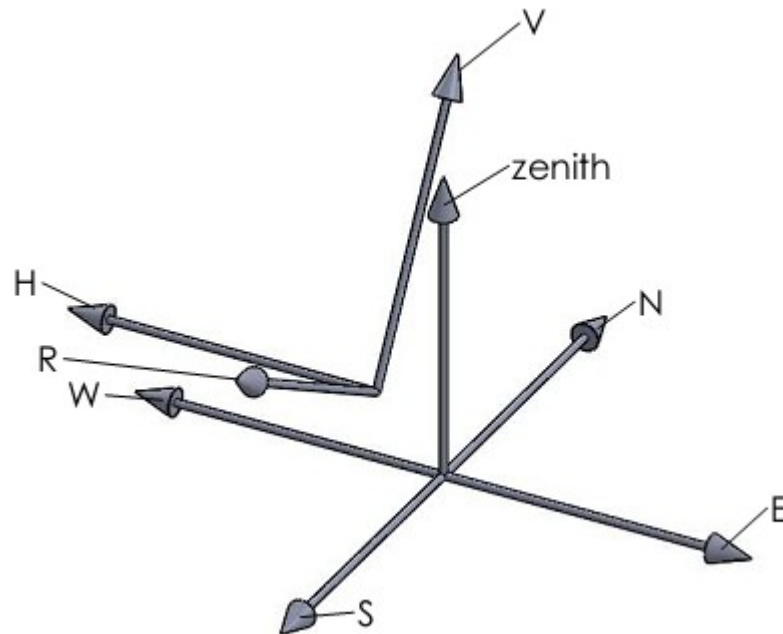


Figure 5.17 – Illustration of the collector reference frame with respect to a Earth surface reference frame.

As seen in Figure 5.18, the tracker orientation within the collector reference frame is defined by the position of the collector plane normal, v , the collector plane vector, k , and the tilt axis vector, r . Collectively, these three vectors are referred to as the collector plane's reference frame. And it should be noted that all vectors in this discussion are considered to be unit vectors unless otherwise stated.

In regards to the tracker orientation, the movement of the tracker is restricted such the collector plane vector always remains within the plane formed by R and H . With the remaining two degrees of freedom, the collector plane normal is oriented according to the angles β and α . To align the collector plane normal with the Sun's position vector, one must set β equal to the hour angle, ω , and set α equal to the declination, δ .

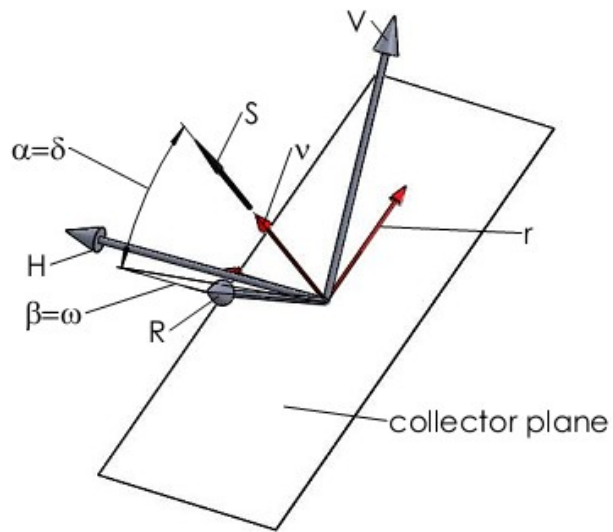


Figure 5.18 – Illustration of a conventional dual axis tracker within the collector reference frame.

In the case of the polar aligned single axis tracker, as seen in Figure 5.19, the tilt axis remains coincident with the vertical axis, which forces the angle α to be zero. With the remaining degree of freedom, the collector normal, v , is positioned such that β equals the hour angle, ω . Thus, in this case a change in the Sun's position vector, S , always remains within the plane occupied by the collector normal, v , and the vertical axis. Then the angle S makes with respect to the collector normal is equal to the declination, δ .

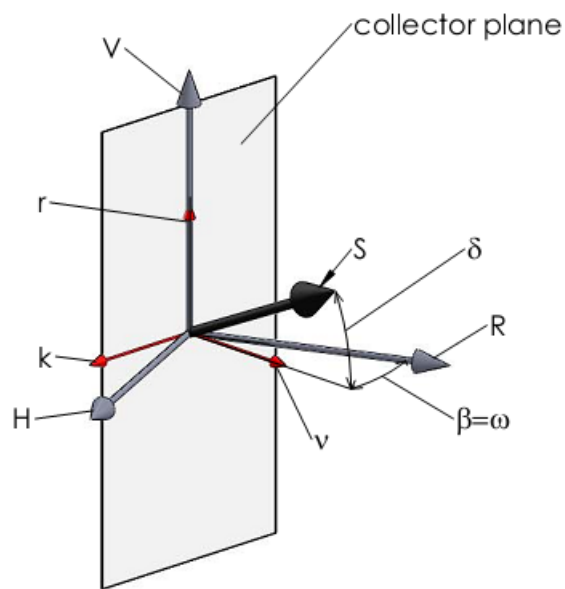


Figure 5.19 – Illustration of an on-axis tracker.

Now, it will be shown that by simply shifting the diurnal motion of the single axis tracker by a phase shift, ψ , such that $\beta = \omega + \psi$, then a constant angle off-angle, κ , can be made between the Sun's position vector and the collector normal.

Consider only the collector plane's reference frame which is only allowed to rotate about the polar aligned axis, r , such that the Sun's position vector S remains at an off-angle, κ , with respect to the collector plane normal, v . As a consequence, given that the magnitude of S is unity, the projections of S in the $k - v$ plane and $k - r$ plane, as illustrated in Figure 5.20, clearly must be true.

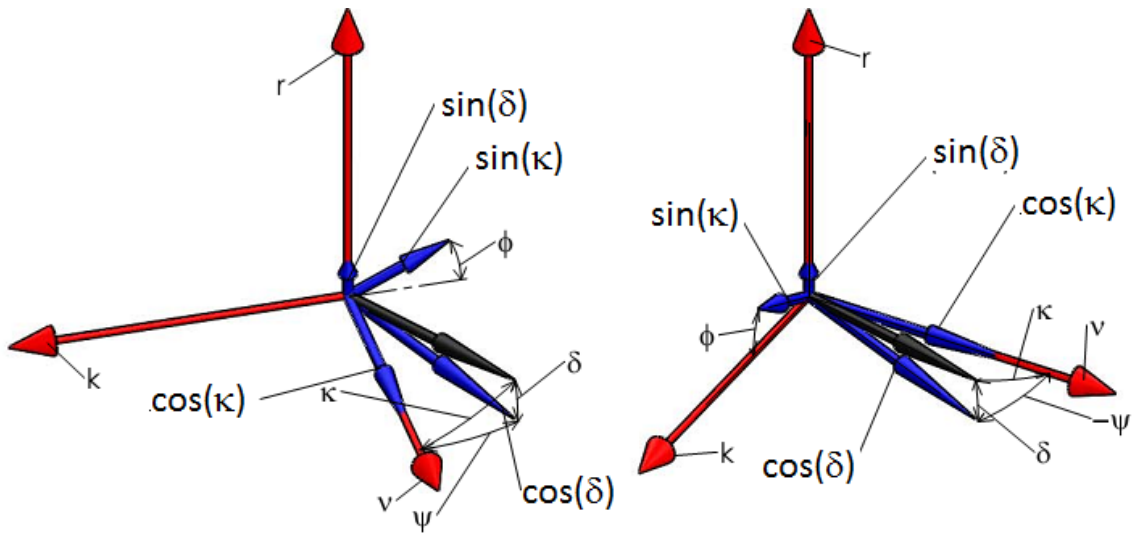


Figure 5.20 - Projection of S in the collector plane reference system.

It follows, therefore, that if one wants to move the collector with respect to the Sun's position vector subject to our declared constraints, the following relationships must also be true.

$$\cos(\psi) = \frac{\cos(\kappa)}{\cos(\delta)} \quad (12)$$

And,

$$\sin(\phi) = \frac{\sin(\delta)}{\sin(\kappa)} \quad (13)$$

where we define,

$$0 < \kappa \quad (14)$$

Equation (12) and (13) provide us with the transformation from conventional polar tracking to an off-axis tracking configuration given κ and the declination δ . As the naming

convention implies, the phase shift, ψ , is simply a shift of the diurnal tracking motion from the hour angle ω . The alignment angle, ϕ , is the angle with respect to the k axis within the collector plane which, as its name implies, indicates how the optical system must be oriented. Exactly how the optics are aligned depends on the exact design. However, we know that some form of dynamic rotation within the optics that is proportional to the change in the alignment angle must occur.

There are clearly there are two possible scenarios corresponding to $\pm\psi$, which clearly satisfies the conditions in Equation (12), since $\cos(\psi) = \cos(-\psi)$. As illustrated in Figure 5.20, when we add a phase ψ , then ϕ must be measured with respect to the negative k axis. Using the same type of reasoning, when a phase ψ is subtracted from the hour angle, ϕ must be measured with respect to the positive k axis.

To clarify the diurnal motion of an off-angle tracker, the orientation of the collector with respect to the collector frame of reference is shown below Figure 5.20 with the orientation of the collector set to be at $\beta = \omega + \psi$ or $\beta = \omega - \psi$.

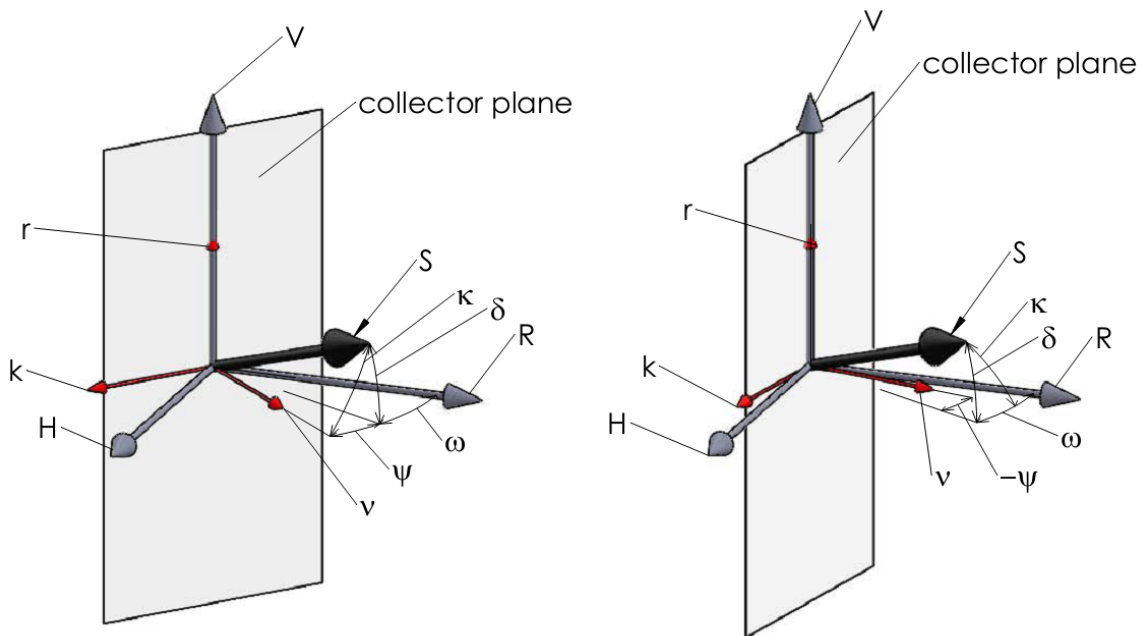


Figure 5.21 - Illustration of the collector's diurnal motion phase shifted by $\pm\psi$.

Off-angle tracking works because the Sun's position is bounded by the positions at the winter and summer solstices. Unlike conventional tracking, off-angle tracking is not capable of aligning the optics at any point within 4π steradian and this can be understood by observing Equation (12) where we can clearly see that if $\kappa < |\delta|$, the equation has no real solution.

Physically, this requirement means that in order for off-angle tracking to be possible, the declination angle must never exceed the off-angle, κ . In a more abstract sense, an imaginary belt, symmetrical about the $R - H$ plane and with an angular extent of $-\kappa < \delta < \kappa$, may define the region where the source position vector may point to while satisfying the conditions set forth by Equation (12) and (13).

As an aid for understanding, Figure 5.22 shows a mapping between (κ, δ) and (ψ, ϕ) .

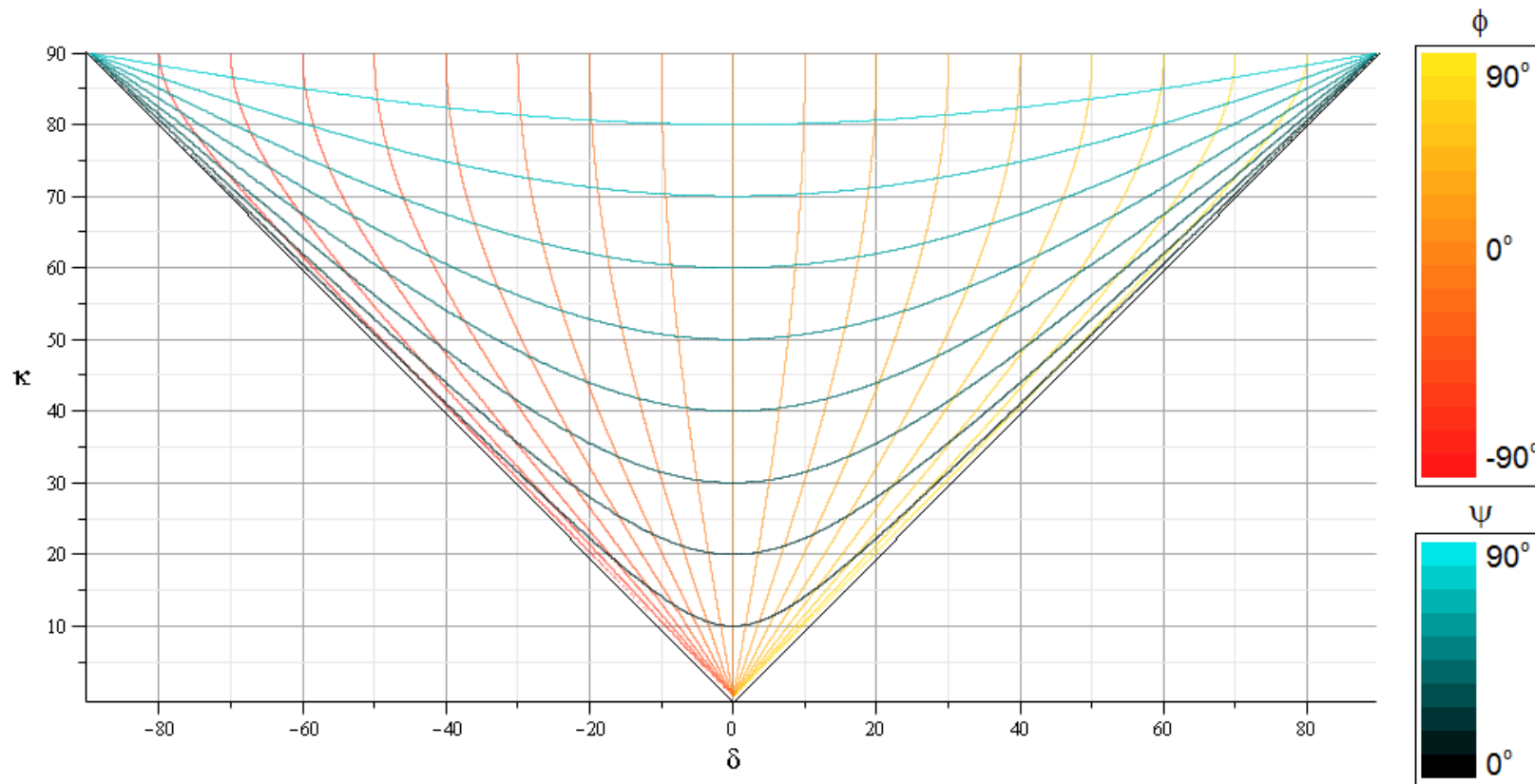


Figure 5.22 - Mapping between the declination, δ , and off-angle, κ , with the phase shift, ψ , and orientation, ϕ , of the focal point on the receiver plane.

6 Concentrator Optical Design

6.1 Introduction

Systematic optimization methods implemented with a computer can only at best modify the curvature and distances between multiple optical elements. However, it is up to the optical designer to determine the best configuration of the lenses within an optical system. The configuration of the lenses has the greatest impact on the system performance and functionality. As a result, while optimization plays a role in the following analysis, the central goal was to find the best system configuration.

6.1.1 Definitions

In all models, the Sun is modeled in LightTools as a Lambertian disk set far away from the receiver. As seen from the aperture, the source thus appears to be an isotropic source with a radius that subtends a 0.2665° arc. The spectrum is defined to be the standard AM1.5 spectrum and the irradiance on a surface perpendicular to the source is a standard $0.1\text{W}/\text{cm}^2$. However, unless otherwise stated, the index of refraction is set to be 1.5 and there is no dispersion. All reflective surfaces are also lossless at all wavelengths.

For convenience sake, the radius of the concentrator's aperture is 5 cm. The receiver radius is defined as the radius of a circle which encompasses 95% of the energy incident on the receiver plane for a Lambertian source that subtends a given arc length. For the given arc length, the corresponding geometric concentration ratio would then be the area of the aperture over the area of the receiver.

In addition, the off-angle is set to be 25° instead of 23.44° simply because it is a nice number close enough to 23.44° to still be reasonable to work with. In addition, a practical system may also have a design angle slightly larger than 23.44° to allow for more tolerance. In any case, the results from following analysis are still applicable to other design angles.

6.2 On-Axis Designs

Although off-axis lenses are our primary concern, on-axis lenses are far more popular and easier to understand. For the sake of completeness and as an introduction, they will be discussed here. The discussion will also aid in our understanding of the off-axis lens performance issues.

6.2.1 Plano Convex On-Axis Lens

In CPV system design, it is more common to have the flat side of a lens facing outward than inwards. This actually has very little to do with optical performance and is related to the fact that flat surfaces are less prone to soiling. This is especially true if a Fresnel lens and its many grooves are facing the external environment. On the other hand, a better focus can be

achieved by facing the curved surface towards the more collimated beam, which is especially true for off-axis illumination. Consider for example, a lens with the specifications given in Table 2.

Table 2 - Lens Specifications (cm) for a plano convex lens.

Primary Rear Surface	
Conic Constant	-2.25
Curvature	0.1498
Diameter	10
Depth	1.65
Refractive Index	1.5
Receiver Plane	-15

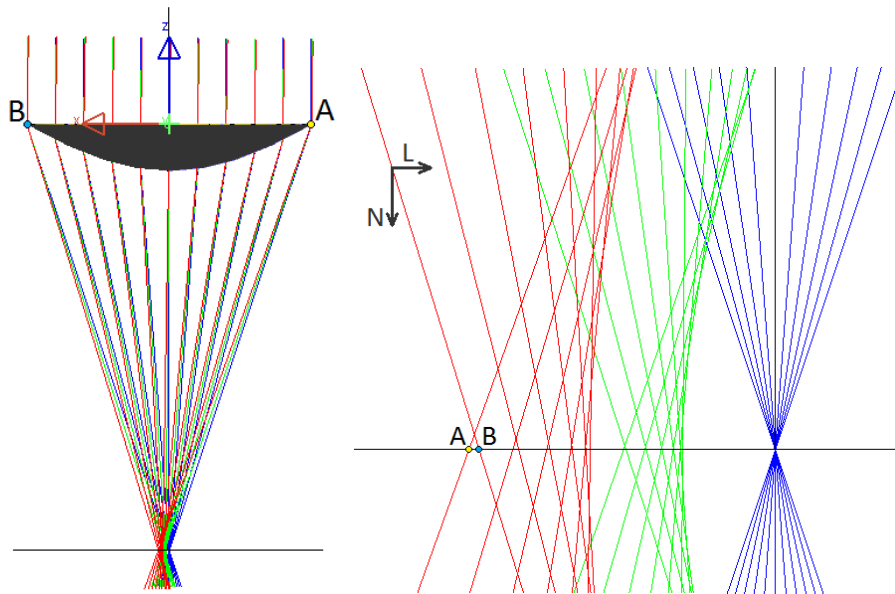


Figure 6.1 - Illustration of a focused beam at 0° (blue), 0.5° (green) and 1° (red) incidence; the points A and B are shown here and in Figure 6.2 and Figure 6.3 to show the correspondence of each diagram.

Figure 6.1 is an illustration of a plano convex lens which forms a perfect stigmatic image along the optical axis. Such a lens is called an aplanat because it is free from spherical aberration. Rays located in the plane containing both the optical axis and the object point are said to be located in the tangential plane. The rays within the plane perpendicular to the tangential plane and containing the principle ray are said to be in the sagittal plane. Only considering tangential rays, we can see from the phase diagram in Figure 6.2 how incident light

deviates from normal incidence. We can also see how for increasing incidence angles, the rays spread apart along the focal plane as indicated by the bow in the lines in Figure 6.2.

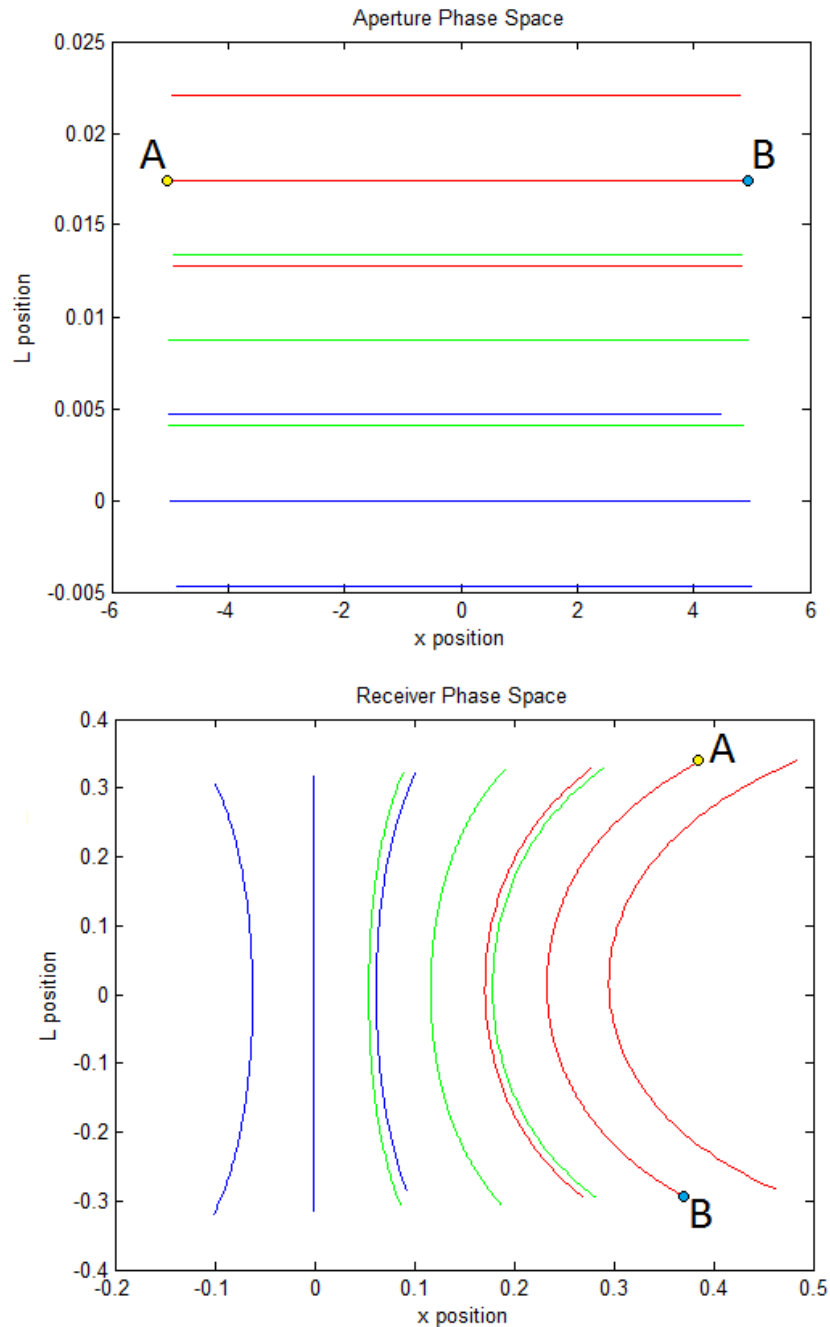


Figure 6.2 - Phase space diagram of tangential rays at the aperture (top) and the receiver (bottom).

The same spreading of rays can be seen for rays outside the tangential plane as seen in Figure 6.3. Essentially, what we have are the edge rays for a spherical source infinitely far away,

subtending an arc of 0.2665° . Superimposed on top of that is a spot diagram showing the rays within meridional planes separated by 10° intervals, for 0° , 0.5° and 1° angle of incidence. Ideally, the edge rays would form a perfect circle and the normally incident beams would converge to a single point. However, this is clearly not the case and is the underlying cause for aberrations in imaging optics and poor thermodynamic efficiency in nonimaging concentrators.

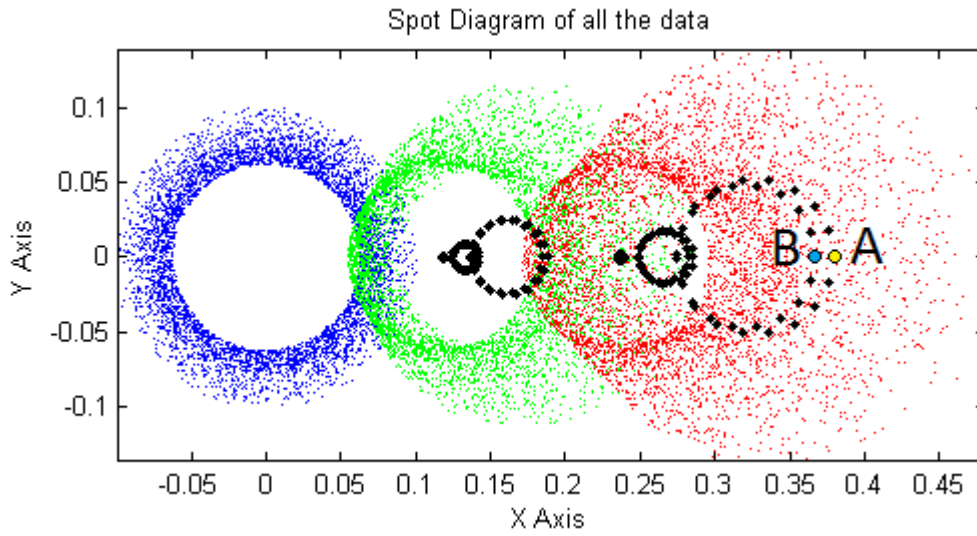


Figure 6.3 – Spot diagram of edge rays incident at 0° , 0.5° and 1° ; The black spot correspond to rays within the tangential, sagittal, and all other planes that intersect the principle ray.

If one were to measure the étendue directly in 4D phase space, the volume would remain the same regardless of the shape. In solar concentration, a thermodynamically efficient concentrator is really only achieved when the edge rays form a perfect stigmatic image. When this is not the case, the result is referred to as étendue dilution. A measure of this quantity is described in the Appendix and some results are shown in Table 3.

Table 3 – Étendue analysis for a plano convex lens at 95% transmission.

Lambertian source half angle	0.2665°	0.5°	1°
NA	0.3219	0.3244	0.3329
Receiver Radius	0.081 cm	0.151 cm	0.302 cm
Aperture Étendue	$\epsilon_{\text{aper}} = 0.005338 \text{ cm}^2 \text{ sr}$	$\epsilon_{\text{aper}} = 0.01879 \text{ cm}^2 \text{ sr}$	$\epsilon_{\text{aper}} = 0.07515 \text{ cm}^2 \text{ sr}$
Receiver Étendue	$\epsilon_{\text{rcvr}} = 0.00671 \text{ cm}^2 \text{ sr}$	$\epsilon_{\text{rcvr}} = 0.02367 \text{ cm}^2 \text{ sr}$	$\epsilon_{\text{rcvr}} = 0.09977 \text{ cm}^2 \text{ sr}$
Thermodynamic Efficiency	$\eta_{\text{opticThermo}} = 75.60\%$	$\eta_{\text{opticThermo}} = 75.40\%$	$\eta_{\text{opticThermo}} = 71.56\%$
Concentration	3810x	1096x	274x

Referring to Figure 6.4, Figure 6.5, Figure 6.6 and Figure 6.7, we can see that there is clearly a relationship between homogeneity, acceptance angle, throughput, and concentration.

Although it is useful to think of these concepts as independent, they clearly are not. The purpose of the plots is to provide an overall description of the optics without bias from a particular metric and without performing a whole system analysis. In addition, the plots are annotated to correspond to the results seen in Table 3.

For clarification, the encircled energy diagram in Figure 6.4 contains a blue curve which indicates the enclosed power and the colored markers represent the percentage of the maximum incident power; the green curve represents the geometric concentration ratio; and the red curve represents the product of the throughput and the geometric concentration ratio. The cyan, red and yellow dashed curve in Figure 6.4 and Figure 6.6 represent the 95% transmission point of the 0.2665° , the 0.5° and the 1° source given in Table 3.

The idea behind the irradiance distribution histogram in Figure 6.5 is to show how much of the receiver area is covered by a given irradiance level. The color of the bars corresponds to the throughput as indicated by the colored markers in the encircled energy plot, Figure 6.4.

Figure 6.6 shows the irradiance distribution at the receiver. The direct normal incidence of sunlight on the primary aperture is set to be a standard $0.1\text{W}/\text{cm}^2$. As a result, it is somewhat easy to gauge the localized concentration. For example, a local flux of $100\text{ W}/\text{cm}^2$ would correspond to a local concentration of 1000x. Lastly, the solid, concentric rings are color coded to correspond to the 0-100% bar in Figure 6.4.

Figure 6.7 illustrates the transmission curve for the 0.2665° , 0.5° and 1° sources as given in Table 3.

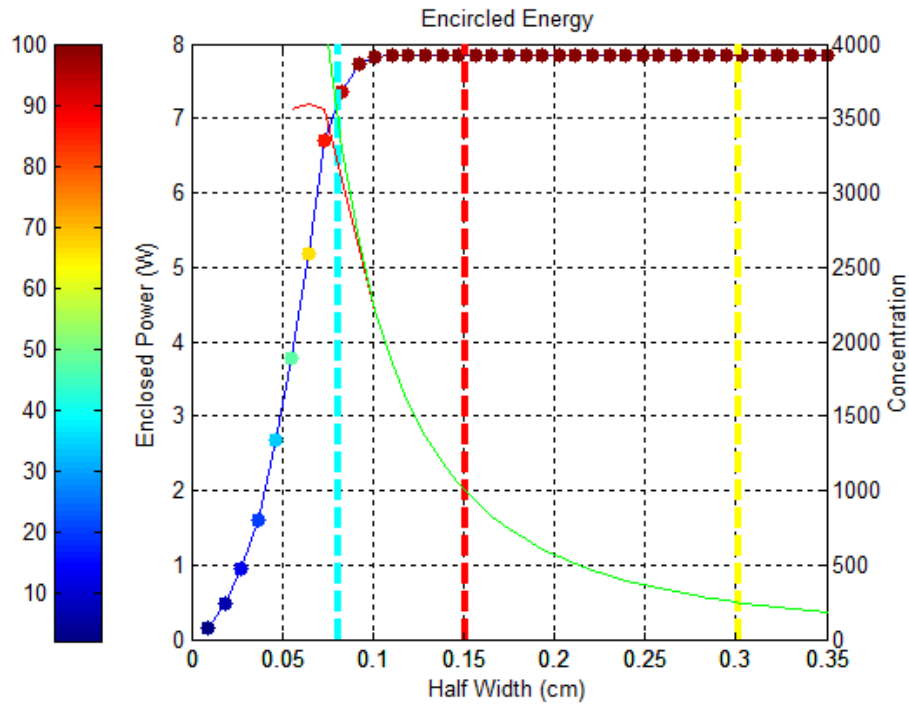


Figure 6.4 – Encircled energy diagram for the on-axis plano convex lens; there is a total of 7.854 W incident on the receiver plane.

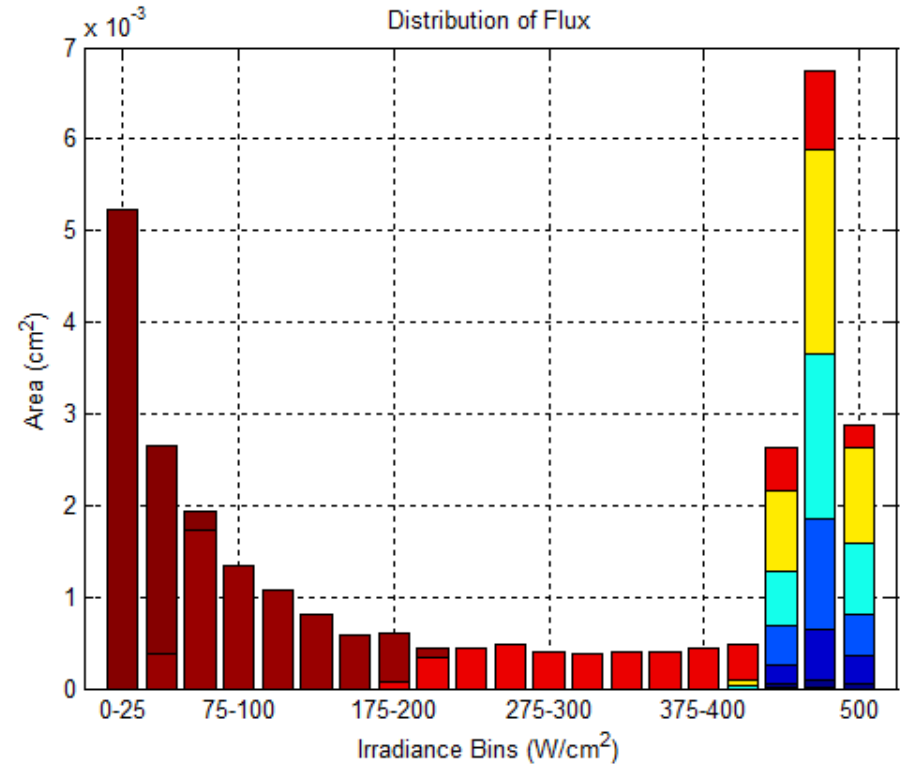


Figure 6.5 – Irradiance distribution histogram for the on-axis plano convex lens.

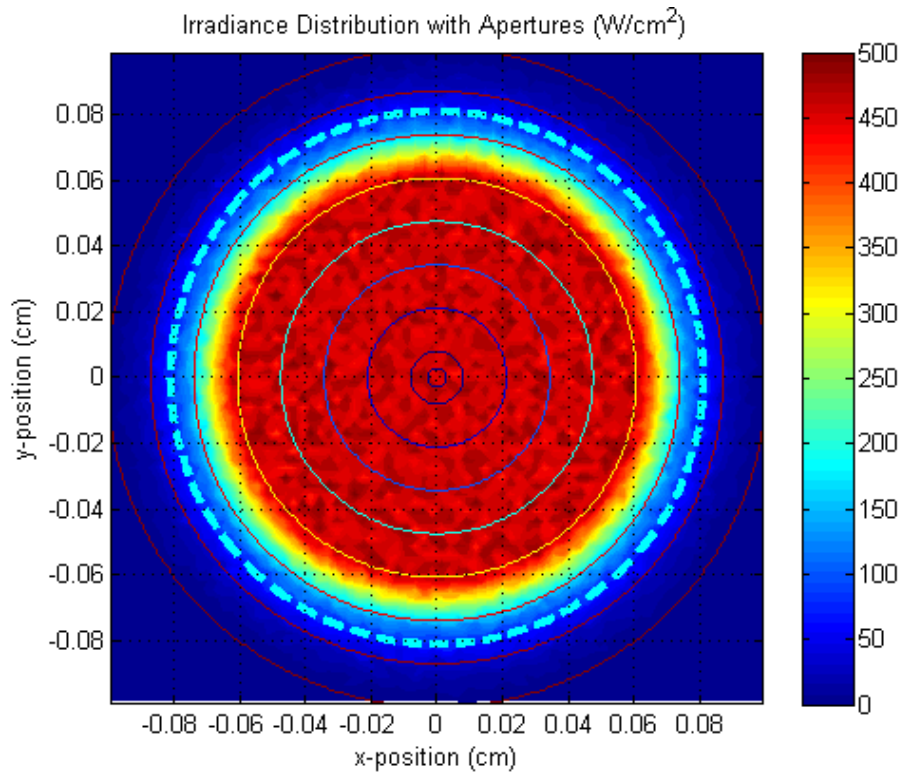


Figure 6.6 – Irradiance distribution diagram for the on-axis plano convex lens.

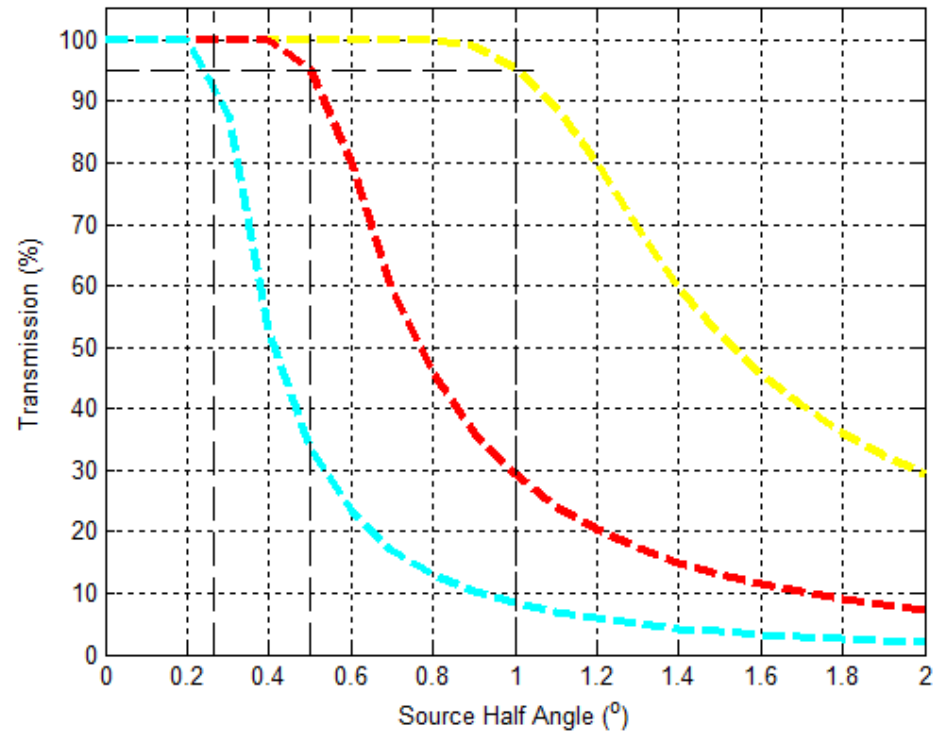


Figure 6.7 - Transmission curve for the on-axis plano convex lens.

6.2.2 Convex Plano On-axis Lens

The convex plano lens suffers much less off-axis aberration than the plano convex lens does. Here, we increased the thickness of the lens slightly but kept the focal length the same, as shown in Table 4

Table 4 - Lens Specifications (cm) for a convex plano lens.

Primary Front Surface	
Conic Constant	-0.5890
Curvature	0.1397
Diameter	10
Depth	2
Refractive Index	1.5
Receiver Plane	-15

In Figure 6.8, an illustration of the rays is shown in the same way as before. However, it is clearly seen that although the system suffers from spherical aberration, the off-axis focus is much better.

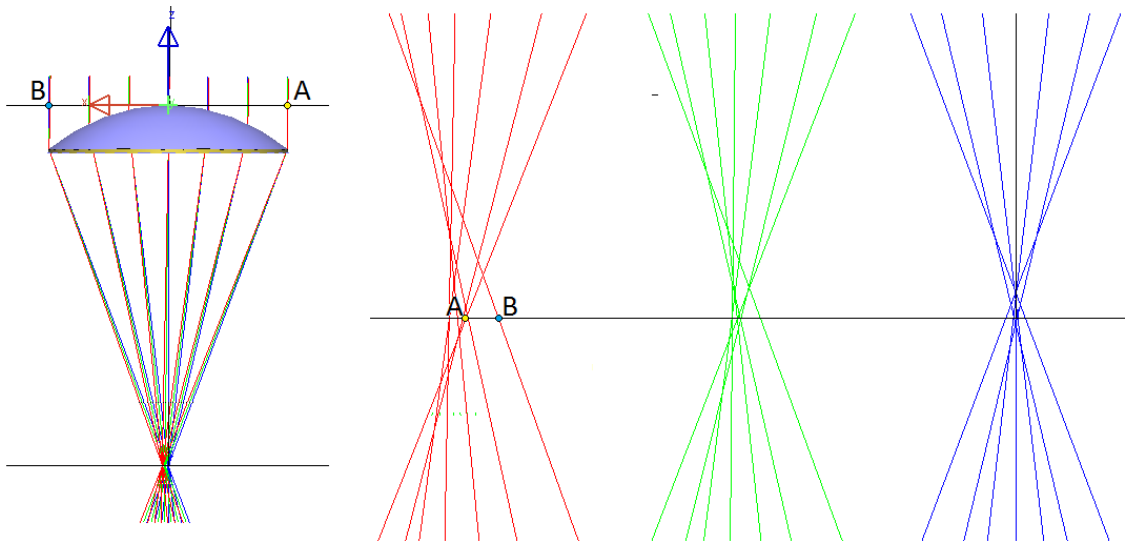


Figure 6.8 - Illustration of a focused beam at 0° (blue), 0.5° (green) and 1° (red) incidence; the points A and B are shown here and in Figure 6.9 and Figure 6.10 to show the correspondence of each diagram.

As seen in both Figure 6.9 and Figure 6.10, the edge rays tend to form a better focus in the convex plano lens than for the plano convex lens. Furthermore, we can see a fundamental

limitation of both the plano convex lens and convex plano lens is that the receiver has a limited numerical aperture.

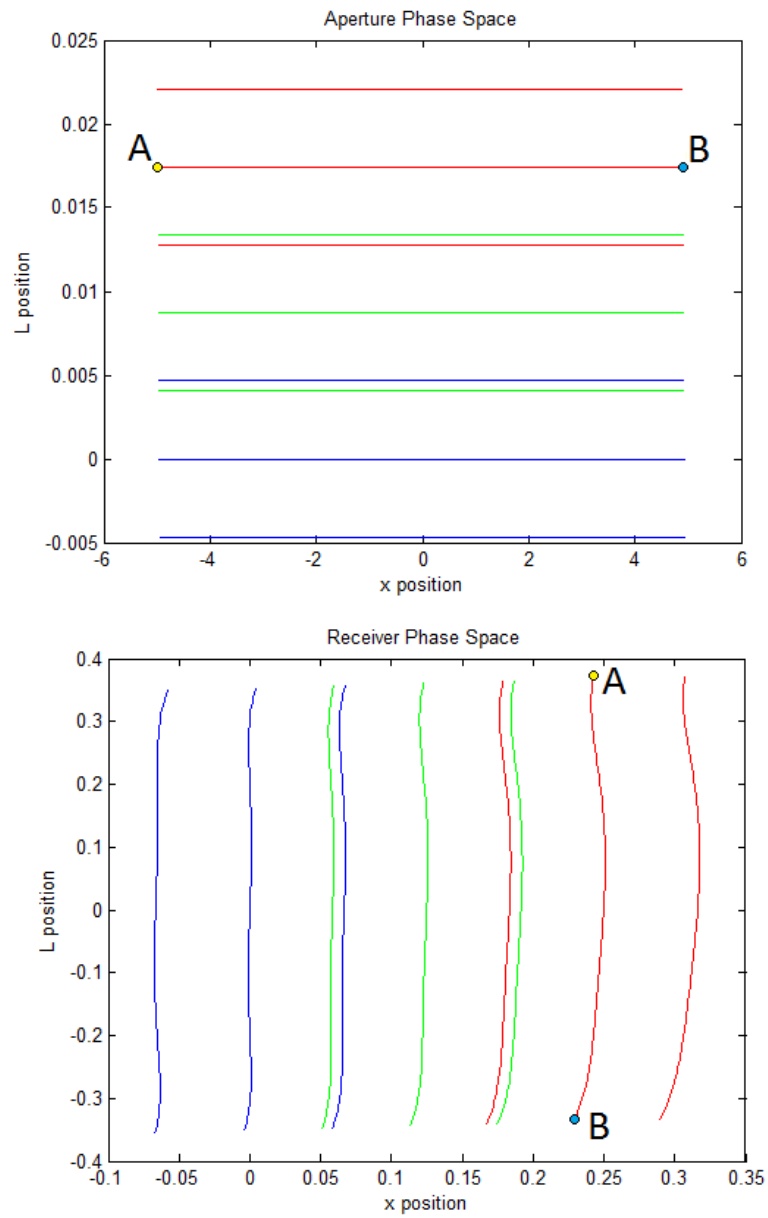


Figure 6.9 - Phase diagram.

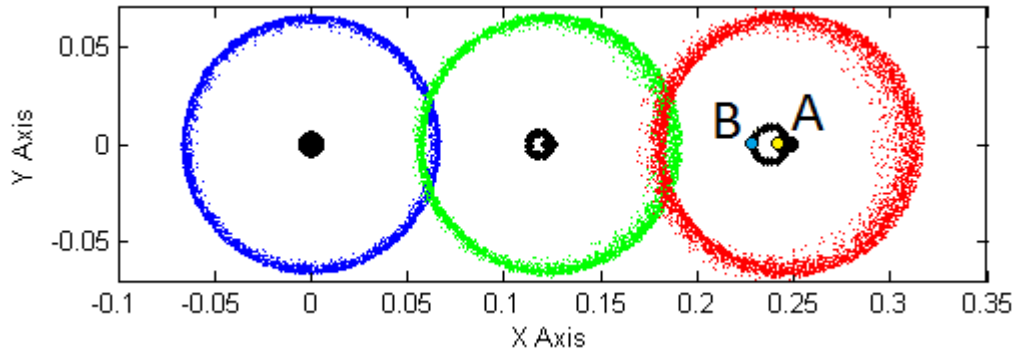


Figure 6.10 - Illustration of edge rays on the receiver.

The better optical characteristics of the convex plano lens compared to the plano convex lens are also reflected in the more intense irradiance distribution at the receiver as illustrated in Figure 6.11, Figure 6.12, Figure 6.13, and Figure 6.14. Furthermore, the analysis results in Table 5 also confirm the improved performance.

Table 5 - Étendue analysis for a convex plano lens at 95% transmission.

Acceptance Angle	0.2665°	0.5°	1°
NA	0.3597	0.3632	0.3701
Receiver Radius	0.0653 cm	0.122 cm	0.244 cm
Aperture Étendue	$\epsilon_{\text{aper}} = 0.005338 \text{ cm}^2 \text{ sr}$	$\epsilon_{\text{aper}} = 0.01879 \text{ cm}^2 \text{ sr}$	$\epsilon_{\text{aper}} = 0.07515 \text{ cm}^2 \text{ sr}$
Receiver Étendue	$\epsilon_{\text{rcvr}} = 0.00545 \text{ cm}^2 \text{ sr}$	$\epsilon_{\text{rcvr}} = 0.01938 \text{ cm}^2 \text{ sr}$	$\epsilon_{\text{rcvr}} = 0.08049 \text{ cm}^2 \text{ sr}$
Thermodynamic Efficiency	$\eta_{\text{opticThermo}} = 93.13\%$	$\eta_{\text{opticThermo}} = 92.12\%$	$\eta_{\text{opticThermo}} = 88.49\%$
Concentration	5863x	1680x	420x

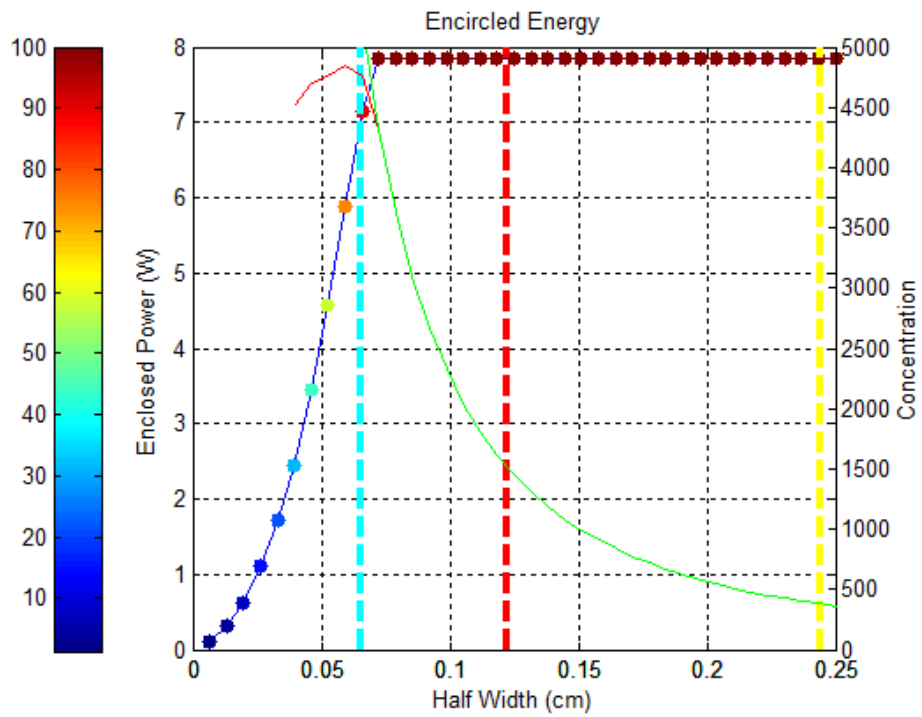


Figure 6.11 – Encircled energy diagram for the on-axis convex plano lens; the peak energy incident is 7.854 W.

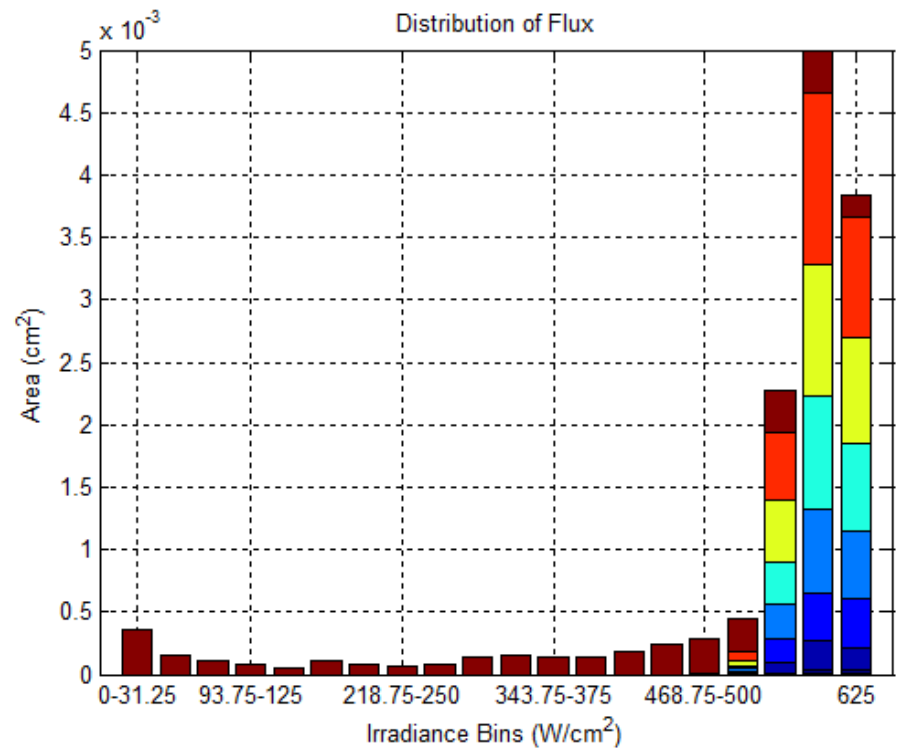


Figure 6.12 – Irradiance distribution histogram for the on-axis convex plano lens.

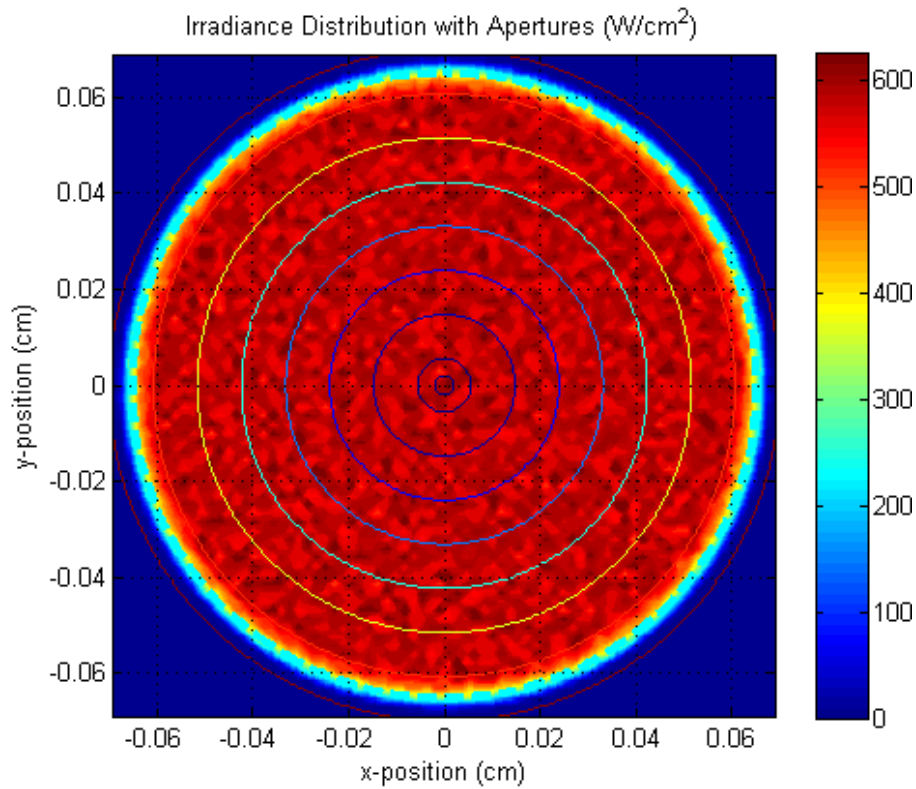


Figure 6.13 – Irradiance distribution diagram for the on-axis convex plano lens.

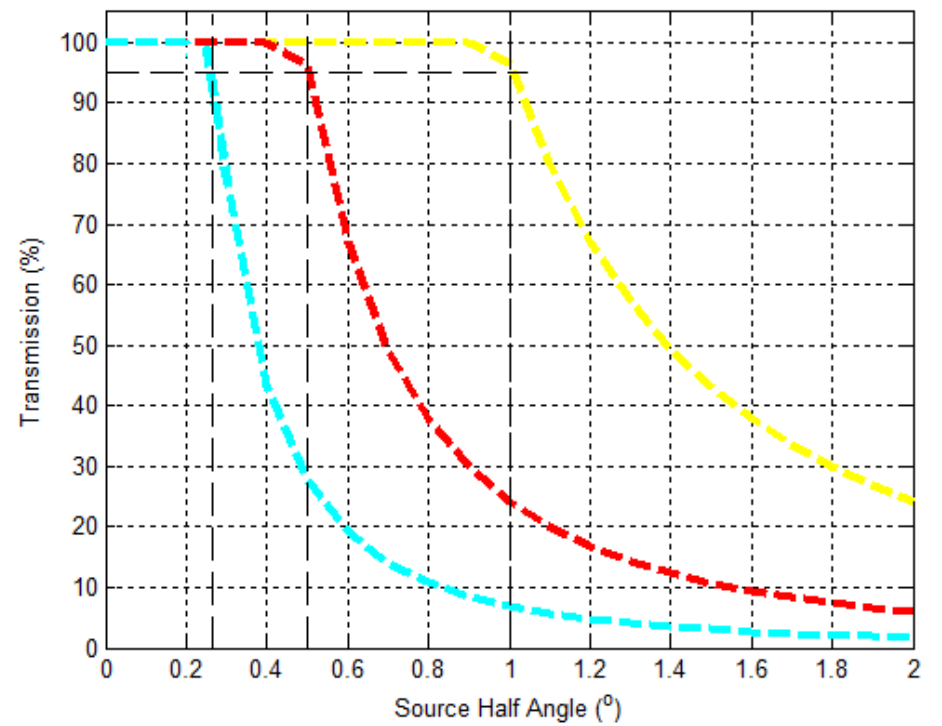


Figure 6.14 – Transmission curve for the on-axis convex plano lens; clearly, the cut-off is much sharper for the convex-plano lens than for the plano-convex lens.

6.3 Off-Axis Designs

6.3.1 Single Plano Convex Off-Axis Lens

The poor performance of the plano convex lens is exaggerated even more for off-axis illumination which for a 25° incident angle, ends up leading to a large caustic. This caustic would be very difficult to remove. As a result, plano convex lenses were not considered as a primary optic.

6.3.2 Convex Plano Off-Axis Lens

The lens as seen in Figure 6.15 used as an off-axis concentrator is the same as the single, convex plano lens used for the on axis concentrator in the previous discussion.. All the specifications as seen in Table 4 are valid except for the receiver plane position which has been moved between the two conjugate focal points.⁵ All main features that result from light being incident 25° off axis can be seen in Figure 6.15. This includes severe astigmatism, field curvature, a smaller effective aperture, and étendue dilution.

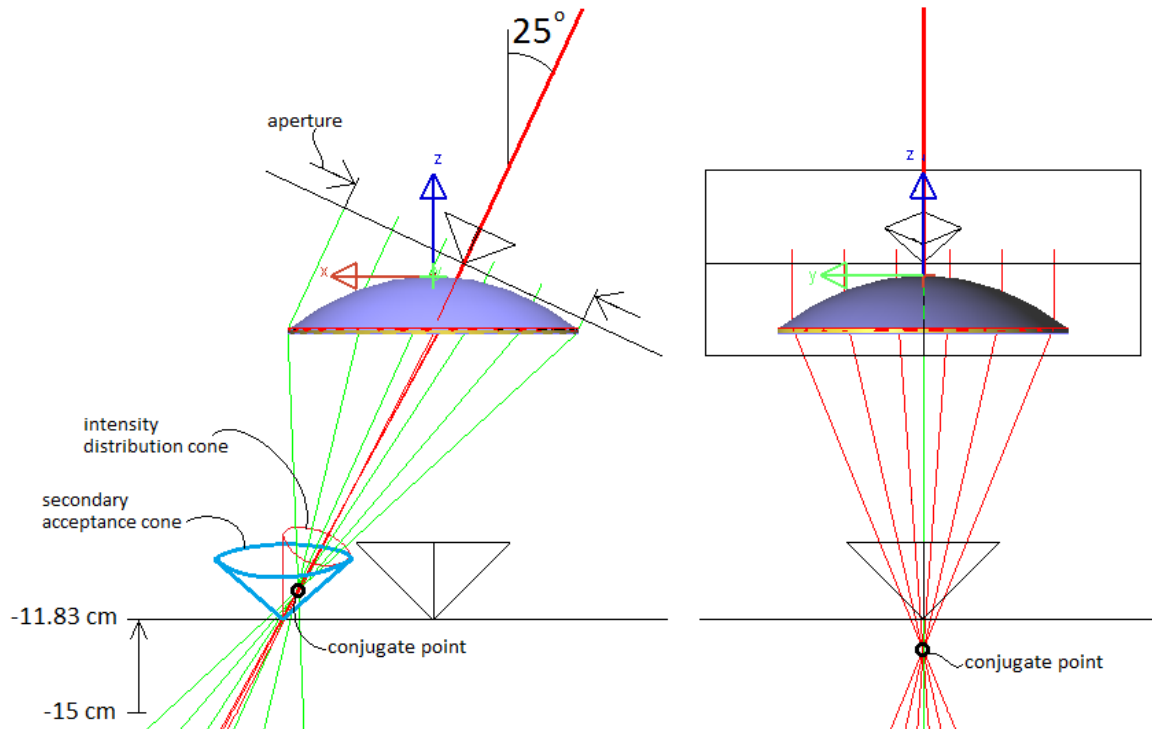


Figure 6.15 - Illustration of severe astigmatism and field curvature; the intensity distribution of light from the lens is also not rotationally symmetric about the receiver plane's normal.

When rays incident on a rotationally symmetric optic are not nearly parallel to the optical axis, the resulting asymmetry leads to the system appearing to have two different focal

⁵ $(x,y,z) = (0\text{ cm}, 0\text{ cm}, -11.826\text{ cm})$

lengths. This phenomenon is referred to as astigmatism and is illustrated in Figure 6.16. The rays within the tangential plane tend to be focused closer to the lens than the sagittal rays. Astigmatism specifically refers to the difference between the two focal points, or conjugate points. This is contrary to the term stigmatism which refers to the property of an optical system whereby rays from a single point in object space also converge to a single point in image space.

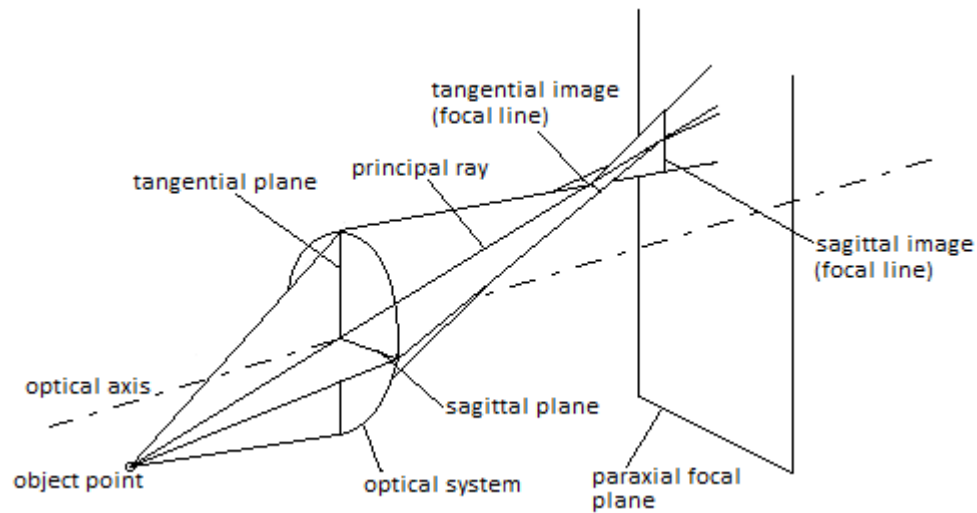


Figure 6.16 - Illustration of astigmatism.

It is important to note that within the limits of ray optics, the rays will rarely ever converge to a single point in either the tangential or sagittal plane. They usually only come very close together to form a caustic surface, or more precisely two caustic surfaces.

The field curvature is clearly illustrated by the fact that the point of best focus shortens from 15 cm to 11.83 cm. In imaging optics a flat field is highly desirable. However in nonimaging optics only the perimeter of the illuminated area needs to form a flat image.

Some confusion may arise when trying to define the size of the aperture in this system. Although there is no widely accepted definition, in this case the aperture will be defined to be the projected lens area onto a plane that is perpendicular to the incoming rays. That is,

$$A \cos(\theta)$$

Thus, in this case concentration is defined by,

$$\cos(\theta) (Primary\ Aperture\ Area)/(Receiver\ Area)$$

However, despite the severe aberrations there is a more critical problem with this design in the context of off-angle tracking. In CPV design it is not uncommon to combine imaging and nonimaging optical components to achieve high thermodynamic efficiency. For

example, the primary optic could be a Fresnel lens and the secondary optical element could be a compound parabolic concentrator (CPC). However, in this case we are focusing off-axis onto a flat plane. Due to the symmetry of the tracking system the secondary optic would have to be rotationally symmetric about the normal of the receiver plane. This poses major limitations since the acceptance angle of the secondary optic must be large to accommodate the mechanical motion. At the same time, an acceptance angle this large will result in étendue dilution thus severely limiting the potential thermodynamic efficiency of this particular configuration.

Figure 6.20 illustrates how the acceptance angle of a secondary optic which maintains rotational symmetry about the normal of the back plane would only ever be partially filled by illumination from the primary optic. Ideally, the secondary optic's acceptance angle should be completely filled.

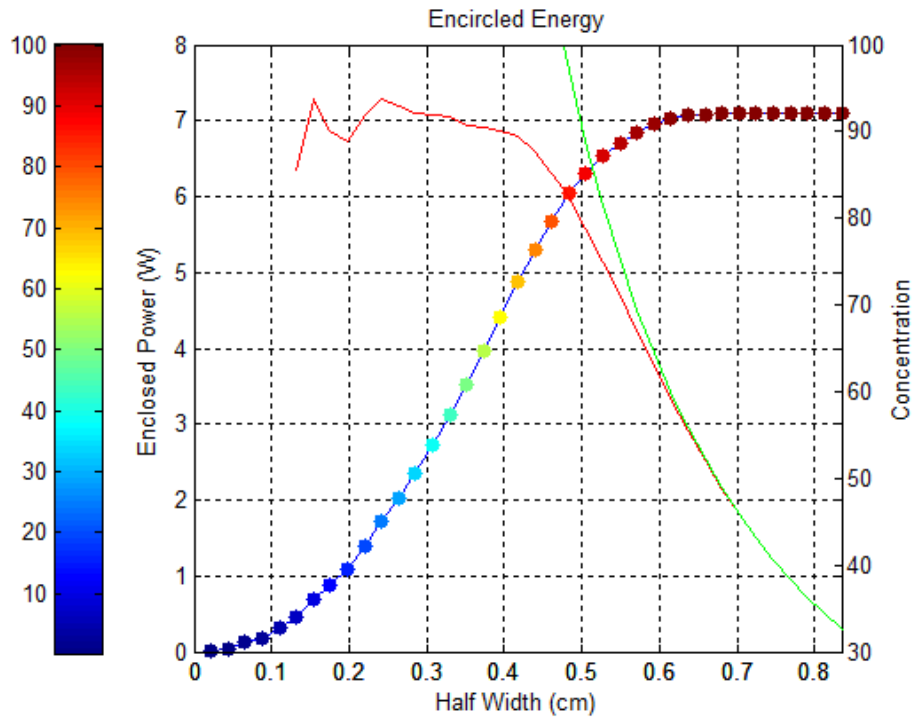


Figure 6.17 – Encircled Energy Diagram for the convex plano off-axis lens; the peak energy is 7.1045 W.

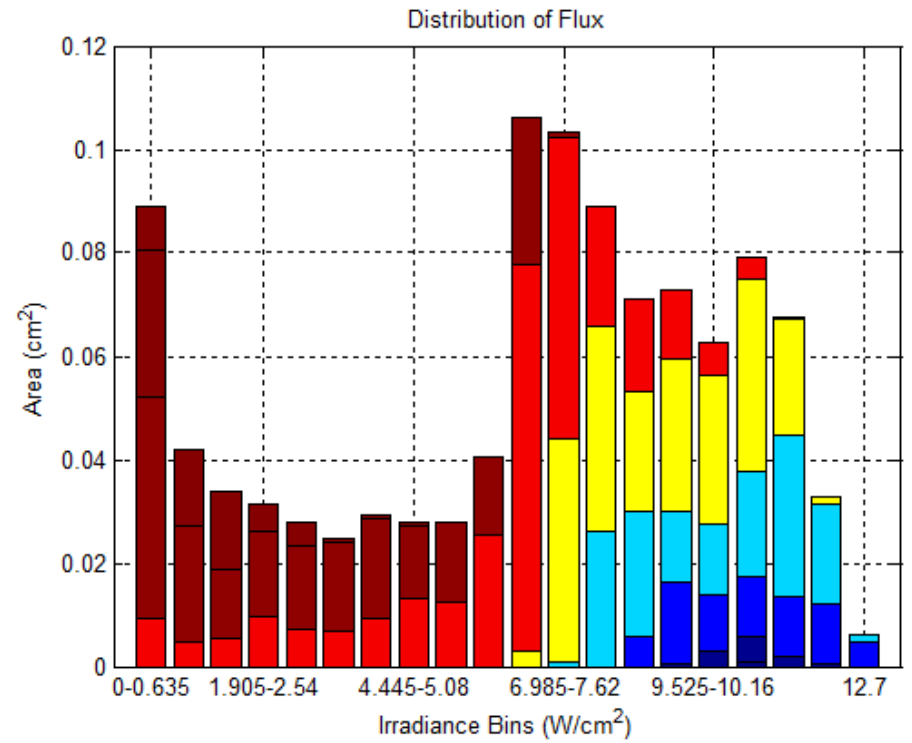


Figure 6.18 – Irradiance distribution histogram for the convex plano off-axis lens.

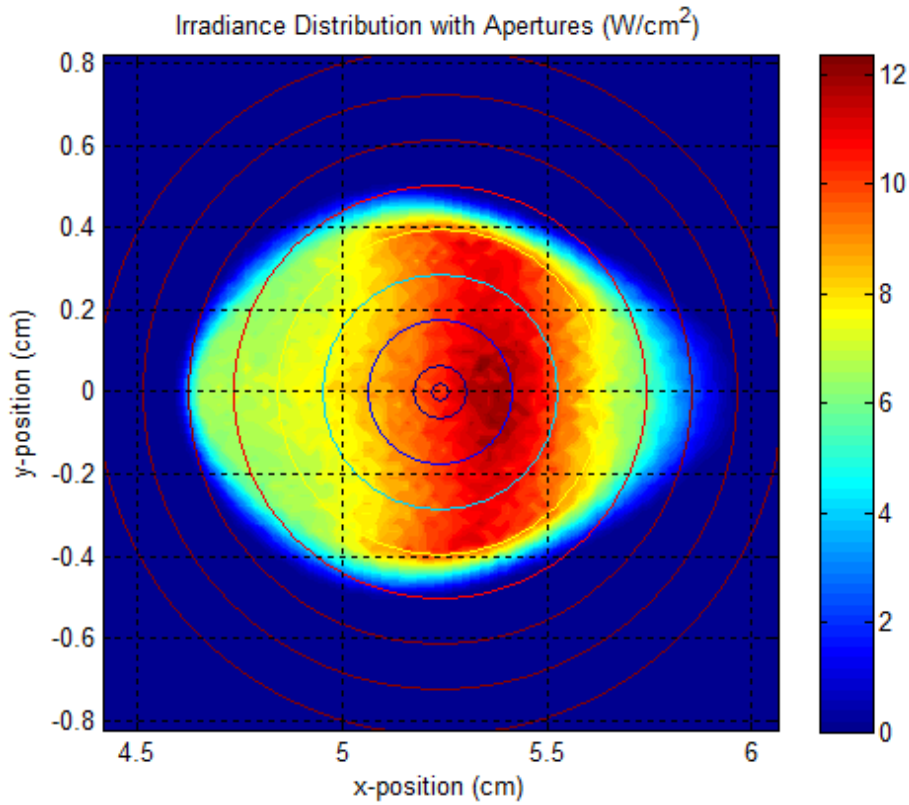


Figure 6.19 – Irradiance distribution diagram for the convex plano off-axis lens.

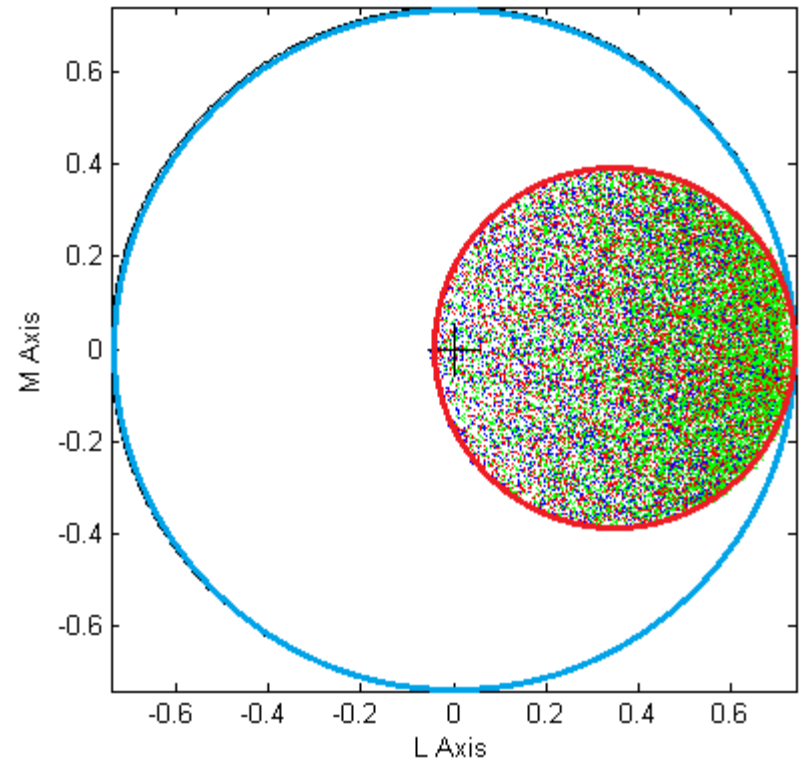


Figure 6.20 – Intensity plot for a 24° (blue), 25° (red), and 26° (green) incident beam of sunlight; the blue circle indicates the acceptance angle that a secondary optic made to be rotationally symmetric about the normal of the back plane (corresponding to the blue cone in Figure 6.15); the red circle represents the boundary of the intensity distribution observed at the receiver from the primary lens (corresponding to the red cone in Figure 6.15).

6.3.3 Single Convex Plano Off-Axis Lens with Tilted Receiver

To address the étendue dilution problem, one can tilt the receiver so that rotation of the receiver about the primary optical axis still allows for the design of a secondary optical element which has a more limited acceptance angle. However, symmetry limits how effectively an array of receivers can move within the off-angle tracking requirements.

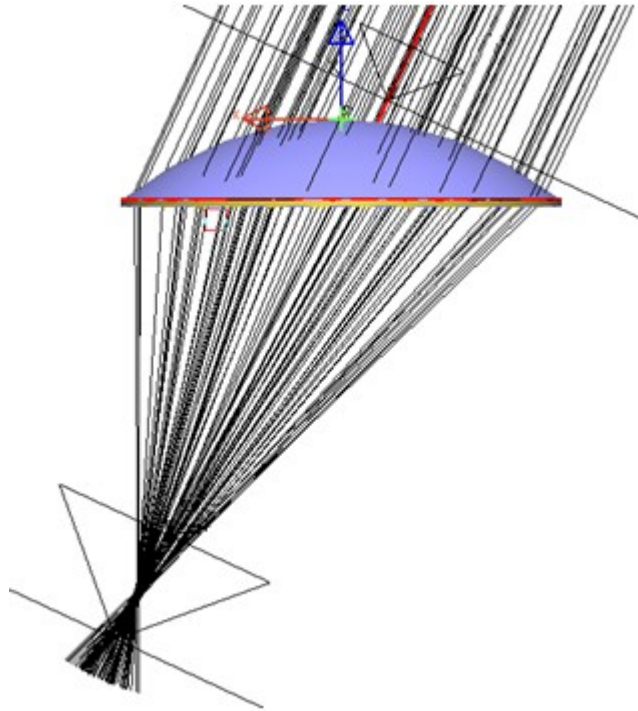


Figure 6.21 - Convex plano off axis lens with a tilted receiver.

Every aspect of the lens has remained the same as specified in Table 4 except for the receiver position and orientation summarized in Table 6.

Table 6 - Lens Specifications (cm) for an off-axis convex plano lens with a tilted receiver.

Primary Front Surface	
Receiver Plane Z	-11.83
Receiver Plane X	5.13
Receiver Plane Orientation	25°

Now consider a secondary optic which enables maximum concentration for a 1° acceptance angle. To do this, we construct a rotationally symmetric edge ray source which is

infinitely far away and subtends an arc of 1.2665° , and with a 25° offset from the normal.⁶ This construction is illustrated in Figure 6.22.

The edge rays form a continuum in R^1 , so theoretically it would require an infinite number of degrees of freedom to perfectly focus the entire source. Instead, only two ray bundles, determined by where the tangential plane intersects the edge ray source, will be considered.

Figure 6.22 illustrates how two planar wave fronts incident at 23.7335° and 26.2665° are focused to the perimeter of 1.2665° radius edge rays. If these two bundles are adequately controlled, symmetry should allow for the continuum of rays to either be well focused or ideally perfectly focused.

⁶ Realistically, neither the sun nor the source within the model is infinitely far away. It is just simple to approximate it as such.

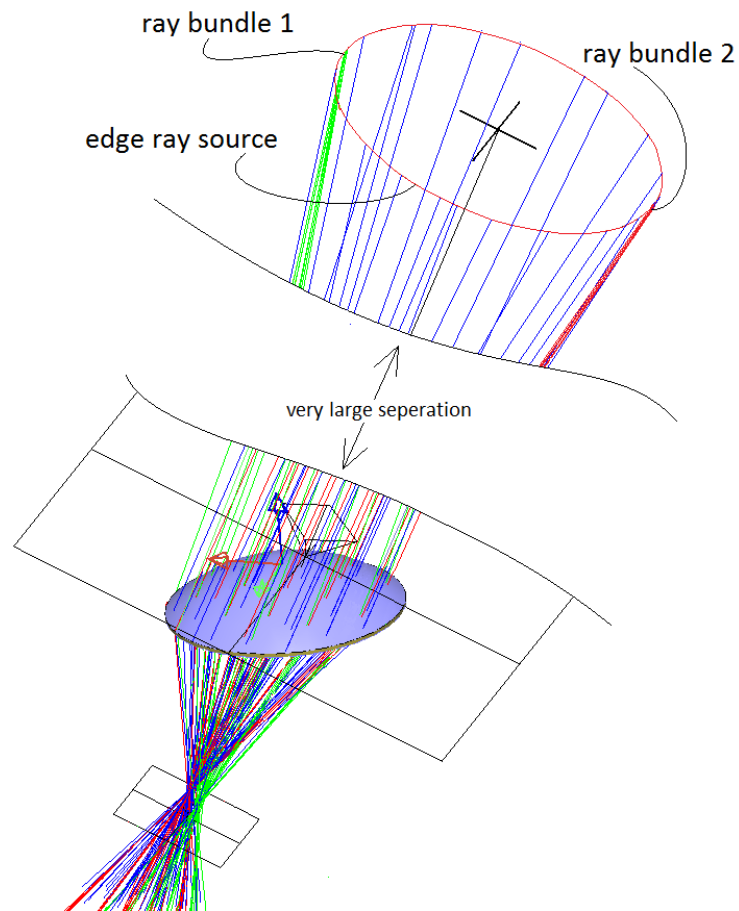


Figure 6.22 - Edge ray analysis; the blue rays represent the edge rays from a source infinitely far away but subtends an arc of 1.2665° ; ray bundle 1 and 2 originate from a point source in the tangential plane at 23.73° and 26.27° respectively.

In conventional simultaneous multiple surface (SMS) design methods, controlling two bundles of rays can be achieved with two optical surfaces in order to allow for very efficient optical designs. It is thought that the same design concepts could be applied here. The intersection of these ray bundles in relation to the continuum of edge rays is illustrated in Figure 6.23.

However, the configuration of these two optical surfaces also plays a role in both the optical and functional performance of the system. This leads, once again, to the exploration of different optical configurations.

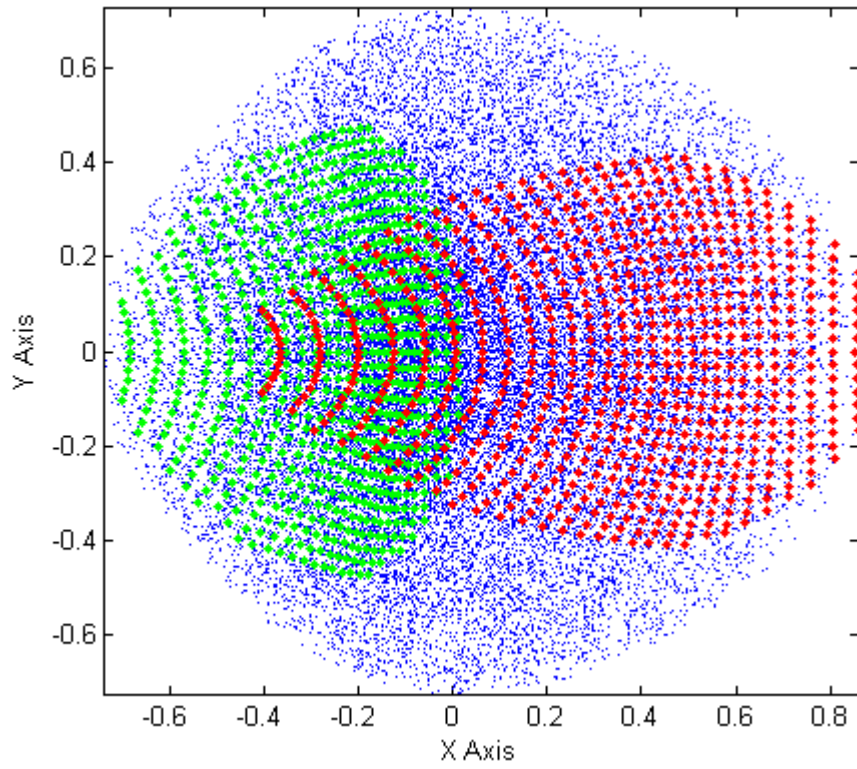


Figure 6.23 – Spot diagram illustrating the intersection of the edge rays of a source subtending an angle of 0.2665° with the receiver plane (blue); a point source in the tangential plane at 23.73° (green); and a point source in the tangential plane at 26.27° (red).

6.3.4 Secondary Optic Design

As shown above, off-axis concentration with a rotationally symmetric primary lens does work. However, even with the potential tracking advantages, without a secondary optic of some kind, the optical performance will be quite poor. Here, we will discuss several possibilities and eventually describe one of the better designs. It is important to note however, that off-angle tracking is a broad concept which encompasses a wider variety of design configurations than will be presented.

6.3.5 Convex Plano Lens with Tilted CPC Secondary

Although the CPC improves the overall thermodynamic efficiency, it is still far from perfect. The only way to come closer to a thermodynamically efficient system would be to remove the rotational symmetry of the secondary optic. This would certainly be possible in the configuration shown in Figure 6.24.

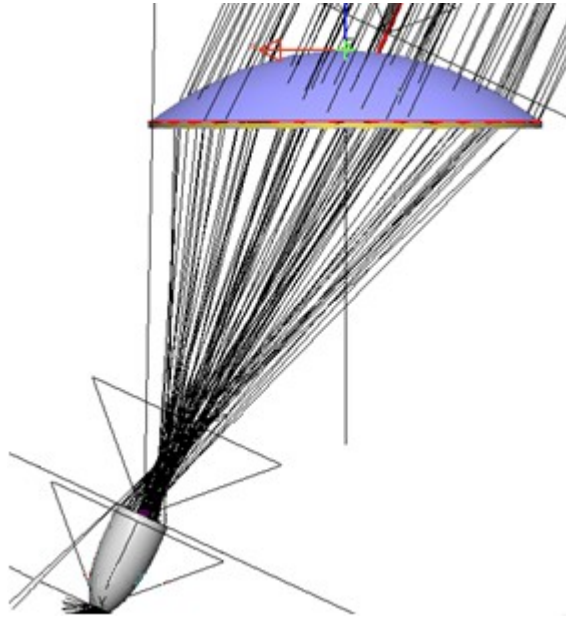


Figure 6.24 - Diagram of an off-angle convex plano lens with a tilted CPC secondary optic.

6.3.6 Convex Plano Lens with an Axial Symmetrical Mirror

The optical system shown in Figure 6.25 is an attempt to use an axially symmetric mirror in combination with a convex plano lens design to operate within the off-angle tracking configuration. It was thought that the mirror could allow for some degrees of freedom which are the curvature of the parabola within the meridional plane, and the curvature of the circle formed by the rotation of that parabola. Even though some improvement was found, it was realized that the relationship between the curvature of the circle and curvature of the parabola imposed constraints on the optimization process. This would be true no matter what curve was revolved around the optical axis. Although it was not proven, it seems reasonable to expect that this system configuration has limited thermodynamic efficiency because of the rotational symmetry restriction.

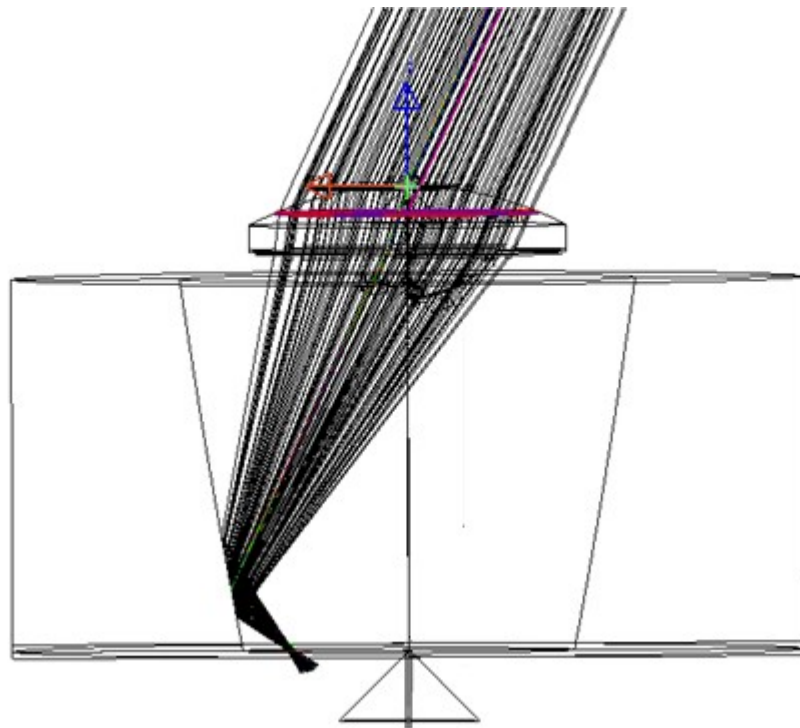


Figure 6.25 - Illustration of a convex-plano lens using a secondary optic that is rotationally symmetric about the primary's optical axis.

The method of creating an axially symmetric mirror is shown below in Figure 6.26. That is, a parabolic mirror was restricted to lie along the optical axis. Optimization was achieved by varying the curvature of the parabola, the diameter, and its position along the z-axis. Note that there are many other types of cross-sections that can be, and have been investigated. However, the scope of the analysis presented here is only to illustrate major restrictions and so only the parabolic cross-section will be shown.

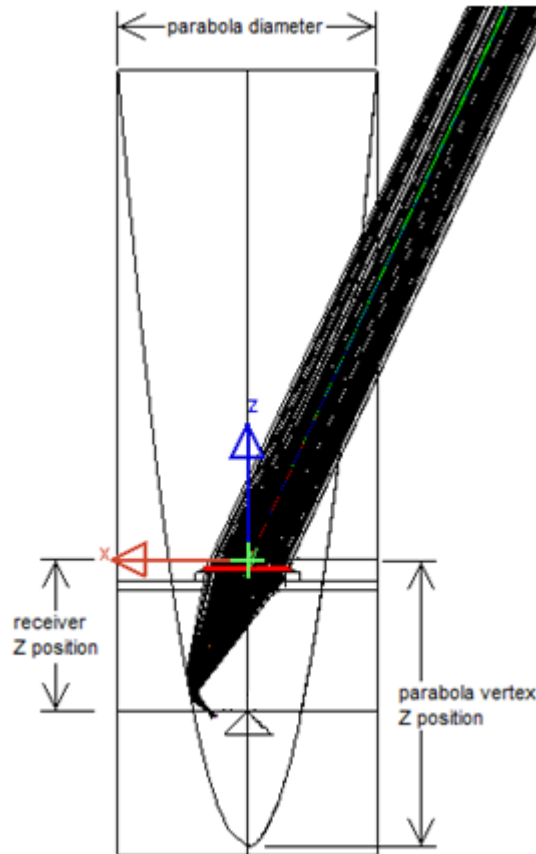


Figure 6.26 – Larger view of the system showing the parabola and receiver position.

Table 7 – Lens Specifications (cm) for a convex plano lens with an axially symmetric reflective secondary.

Primary Front Surface		Secondary Optic	
Conic Constant	-0.4536	Conic Constant	-1
Curvature	0.08005	Curvature	0.8
Diameter	10	Diameter	30
Depth	2.5	Parabola Vertex Z	-33.2620
Refractive Index	1.5	Receiver Z	-17.5724

As usual, we show four plots Figure 6.27, Figure 6.28, Figure 6.29, and Figure 6.30, which illustrate the characteristics of this system. We also illustrate some calculated metrics seen in Table 8. Note that these metrics are only intended to serve as an example of typical system performance. A rigorous comparison between fully optimized designs was not the goal.

Table 8 - Étendue analysis results for the convex plano lens with an axially symmetric mirror secondary.

Acceptance Angle	1°	0.5°	0.2665°
NA	0.8657	0.8657	0.8655
Receiver Radius	0.523 cm	0.295 cm	0.191 cm
Aperture Étendue	$\epsilon_{\text{aper}} = 0.0681 \text{ cm}^2 \text{ sr}$	$\epsilon_{\text{aper}} = 0.01703 \text{ cm}^2 \text{ sr}$	$\epsilon_{\text{aper}} = 0.004838 \text{ cm}^2 \text{ sr}$
Receiver Étendue	$\epsilon_{\text{rcvr}} = 2.0232 \text{ cm}^2 \text{ sr}$	$\epsilon_{\text{rcvr}} = 0.6437 \text{ cm}^2 \text{ sr}$	$\epsilon_{\text{rcvr}} = 0.2697 \text{ cm}^2 \text{ sr}$
Thermodynamic Efficiency	$\eta_{\text{opticThermo}} = 3.20\%$	$\eta_{\text{opticThermo}} = 2.51\%$	$\eta_{\text{opticThermo}} = 1.70\%$
Concentration	83x	260x	621x

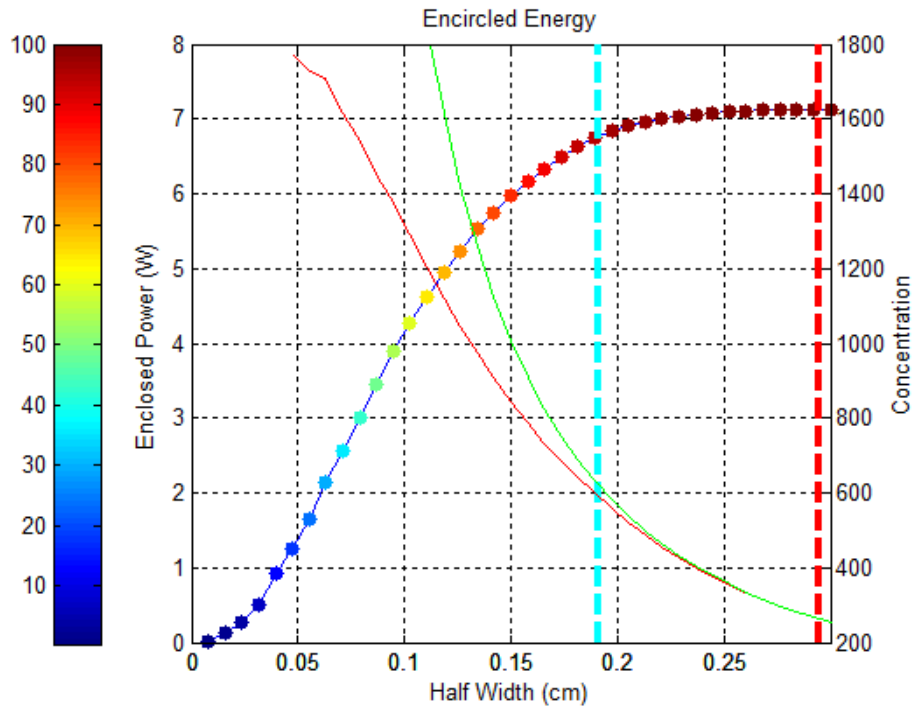


Figure 6.27 – Encircled Energy Diagram for an off-axis convex plano lens with an axially symmetric reflective secondary; the maximum enclosed power 7.1181 W.

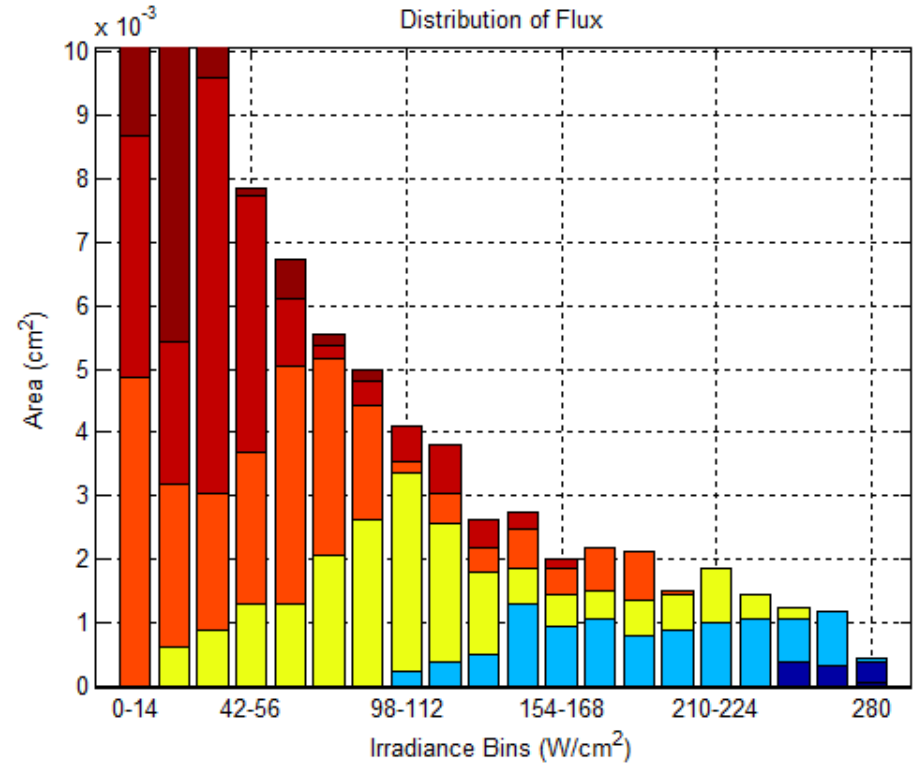


Figure 6.28 – Irradiance distribution histogram for an off-axis convex plano lens with an axially symmetric reflective secondary.

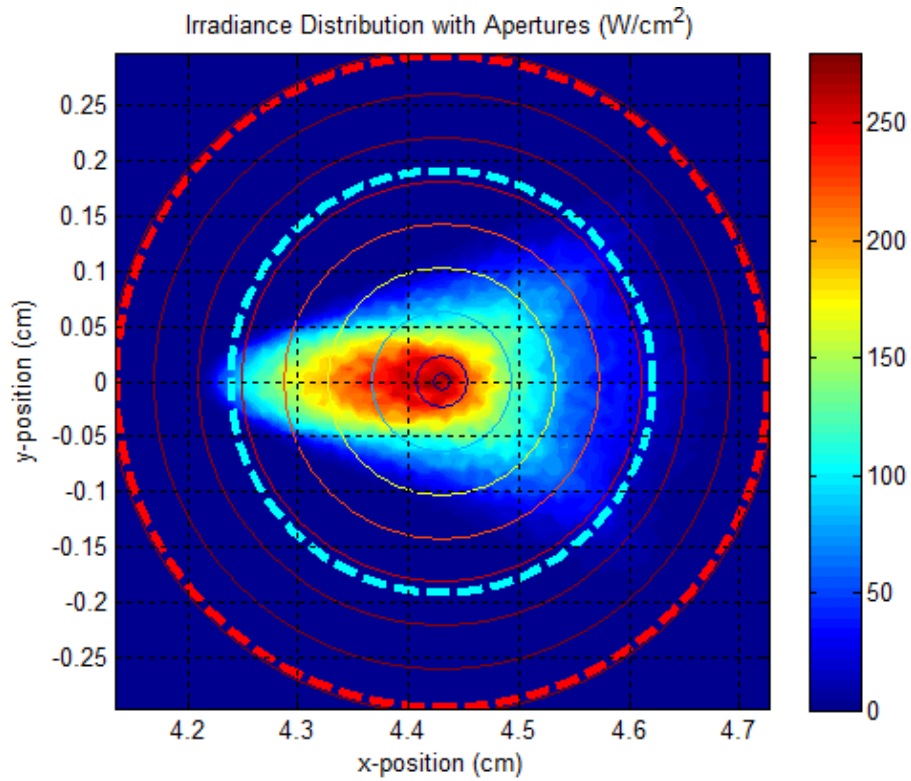


Figure 6.29 – Irradiance distribution diagram for an off-axis convex plano lens with an axially symmetric reflective secondary.

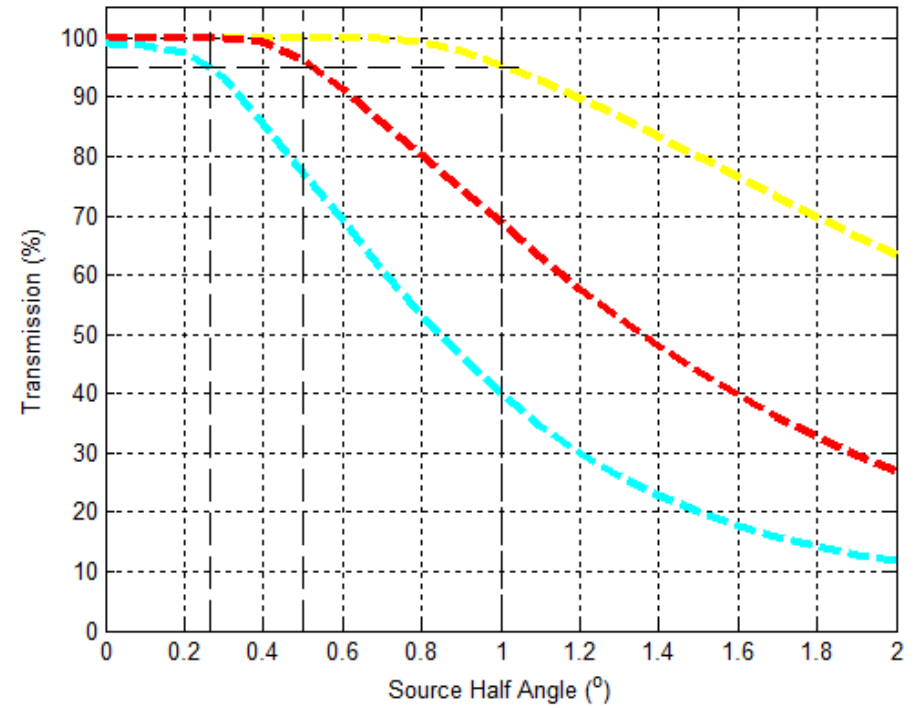


Figure 6.30 – Transmission angle diagram for an off-axis convex plano lens with an axially symmetric reflective secondary.

6.3.7 Convex Plano Lens and Plano Convex Lens

The previous examples use lenses which have an index of refraction of 1.5, along with no dispersion and no absorption. A more realistic example is shown in Figure 6.31 which uses BK7 glass having both dispersion and absorption properties. Both curved surfaces are conic sections. The nominal angle of incidence is 25° , and the total power incident on the aperture is as usual, 7.1181 W. Besides the geometric conditions, another notable characteristic is the losses that arise from using more realistic lenses. This is indicated by the 6.9187 W incident on the receiver plane.

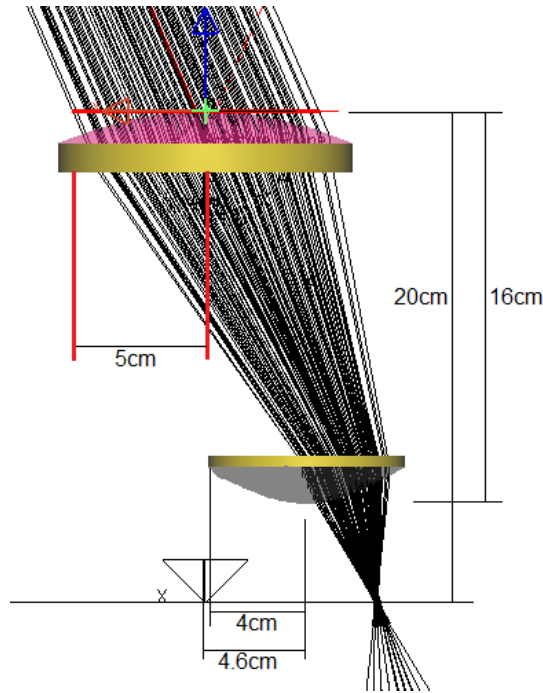


Figure 6.31 - Convex Plano-Plano Convex Lens combination with a 25° design angle.

As mentioned before, this configuration is similar to the one given by Duerr *et al.* [56], [79].

Table 9 - Lens Specifications for the convex plano lens and plano convex lenses.

Primary Front Surface		Secondary Back Surface	
Conic Constant	-2.1394	Conic Constant	-2.5275
Curvature	0.07642	Curvature	0.2429
Diameter	10	Diameter	4
Depth	2.5	Depth	2
Refractive Index	Schott Material - BK7	Refractive Index	Schott Material - BK7

We again show some merit function values given in Table 10.

Table 10 - Étendue analysis results for the convex plano lens and plano convex lenses.

Acceptance Angle	1°	0.5°	0.2665°
NA	0.5177	0.5177	0.5177
Receiver Radius	0.3065 cm	0.193 cm	0.148 cm
Aperture Étendue	$\epsilon_{\text{aper}} = 0.06811 \text{ cm}^2 \text{ sr}$	$\epsilon_{\text{aper}} = 0.01703 \text{ cm}^2 \text{ sr}$	$\epsilon_{\text{aper}} = 0.004838 \text{ cm}^2 \text{ sr}$
Receiver Étendue	$\epsilon_{\text{rcvr}} = 0.2485 \text{ cm}^2 \text{ sr}$	$\epsilon_{\text{rcvr}} = 0.09853 \text{ cm}^2 \text{ sr}$	$\epsilon_{\text{rcvr}} = 0.05794 \text{ cm}^2 \text{ sr}$
Thermodynamic Efficiency	$\eta_{\text{opticThermo}} = 26.04\%$	$\eta_{\text{opticThermo}} = 16.42\%$	$\eta_{\text{opticThermo}} = 7.93\%$
Concentration	241x	608x	1034x

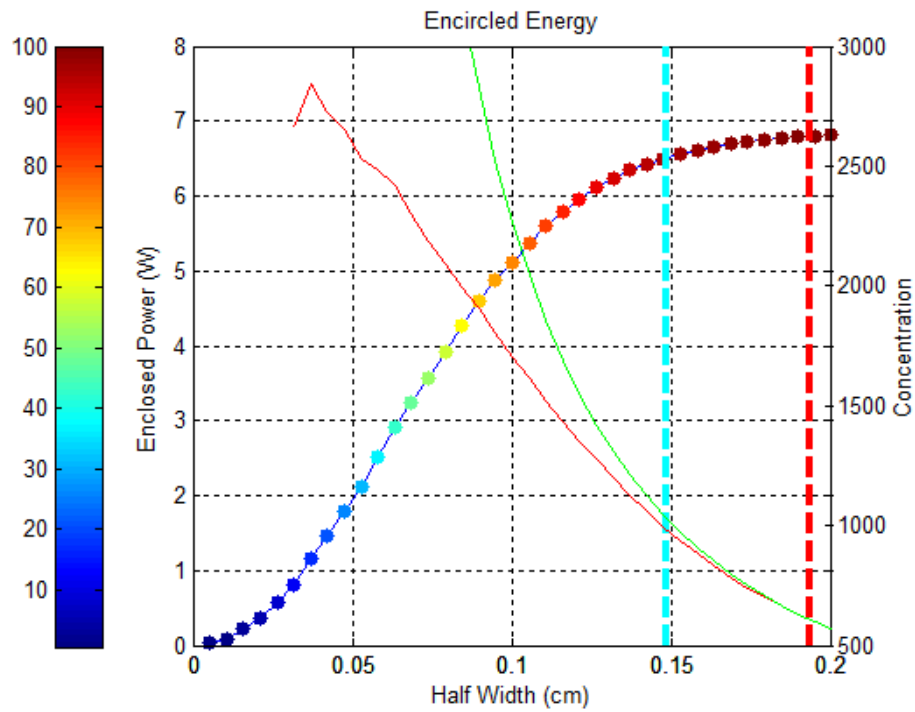


Figure 6.32 – Encircled energy diagram for the convex plano and plano convex off-axis lens system; the incident energy is 7.1181 W and the energy incident on the receiver is 6.9187 W.

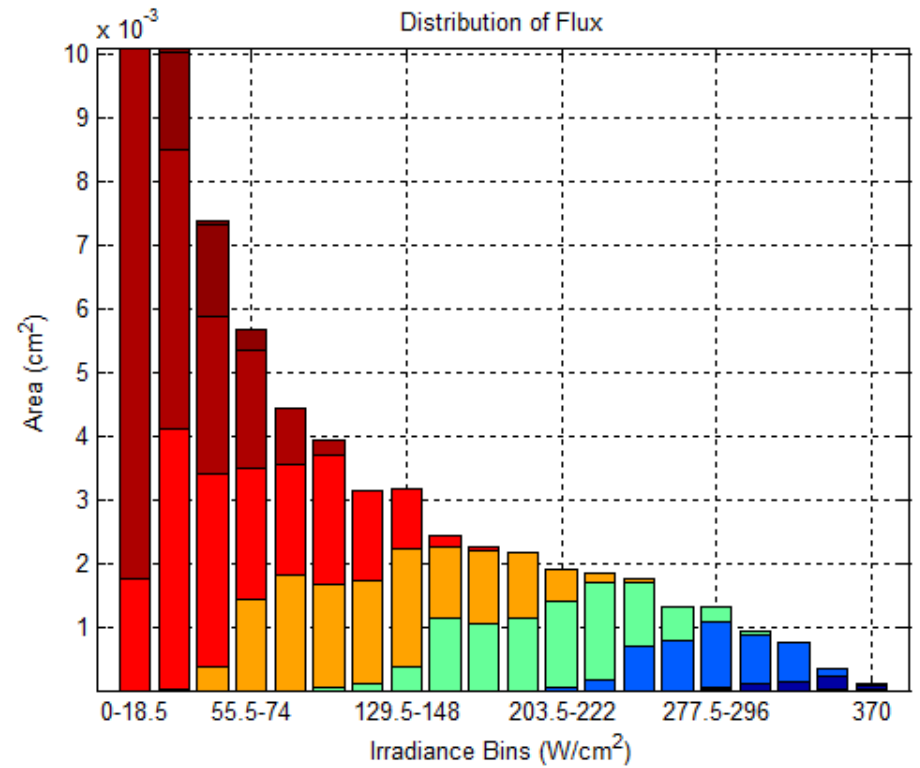


Figure 6.33 – Irradiance distribution histogram for the convex plano and plano convex off-axis lens system.

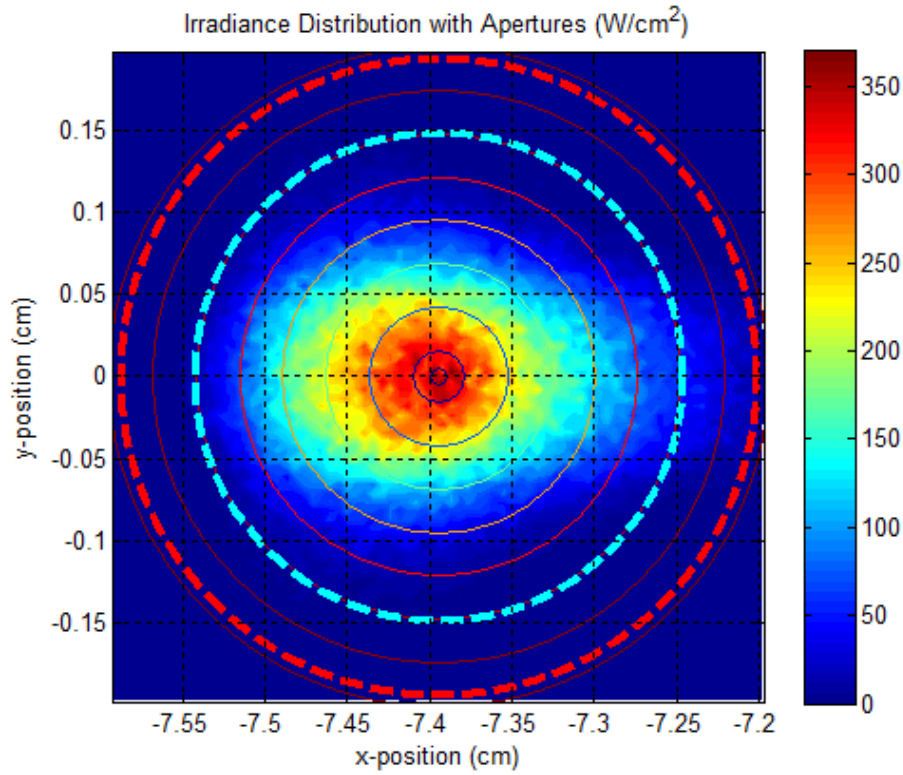


Figure 6.34 – Irradiance distribution diagram for the convex plano and plano convex off-axis lens system.

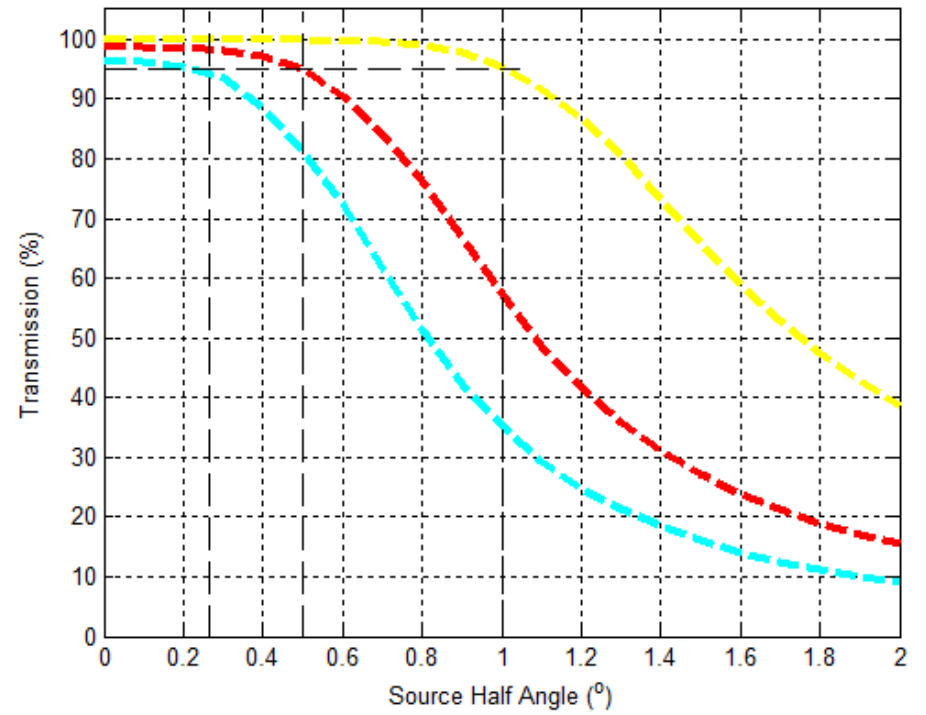


Figure 6.35 – Transmission diagram for the convex plano and plano convex off-axis lens system.

7 A Preferred Off-Angle Optical Design

7.1 Mechanical Design

7.1.1 Basics

Although, as shown in Section 6, there are many ways of going about off-angle tracking, Figure 7.1 below, is an illustration of how this might be achieved in a more efficient manner. To the left, the illustration shows how the primary optic remains fixed and the two secondary optical elements simply rotate about the optical axis. The picture to the right shows these movements from a perspective located below the entire system.

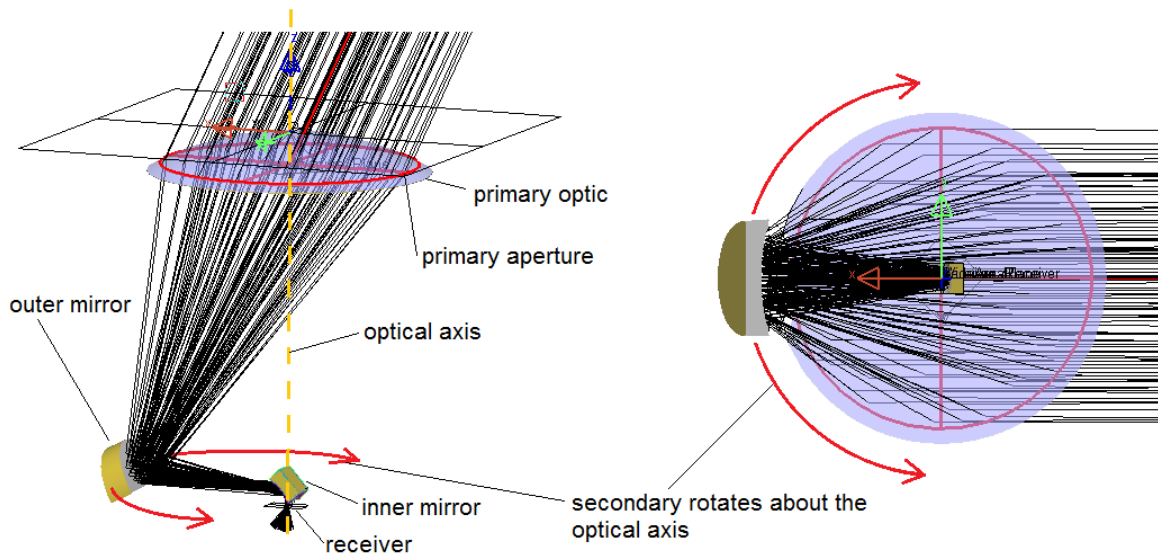


Figure 7.1 - Illustration of the mechanical motion of the secondary optic with respect to the primary optic.

Overall, the optical system consists of four optical surfaces; two refractive surfaces and two mirrored surfaces. Given that the typical CPV module consists of a lens and a secondary optical element, four surfaces is well within reason. Thus, we can expect that the optical losses due to light scattering and absorption would be similar to other CPV systems.

The primary optic is an aspheric-plano lens, and the two secondary mirrors are small freeform surfaces all of which can be manufactured on a large scale.

In this design, the main purpose of the primary optic is to focus the beam down to a sufficiently small size so that the freeform mirrors used for subsequent concentration can be made very small. The reason for this is that it is easier to make small freeform surfaces than larger ones. In addition, freeform surfaces give the designer a great deal of flexibility when it comes to optimizing the optical design. To clarify, it has been shown that only a single surface is

required to transform one congruency of rays to another congruency. In other words, roughly speaking, if you have a parallel, converging, or diverging beam of light you will be able to focus it to any point given a single freeform surface. The SMS design method extends this idea by using two surfaces to transform two congruent beams of light to two other congruent beams of light simultaneously. When you add an additional surface, you gain control over another bundle of rays.

In the case of 2D optics, having control over two bundles of rays allows the designer to completely satisfy the conditions of the edge ray theorem thus allowing the design of thermodynamically efficient concentrators. In 3D, the ability to accurately control the mapping of two or more bundles of rays gives the designer more freedom to create a CPV module with high homogeneity, a large acceptance angle, and a high concentration.

However, it must be noted that the primary optic could possibly be designed in a way that creates problems for the design of the subsequent mirrors. For instance, the primary could create a caustic that intersects the secondary optic. In such a case, bijective mapping of a bundle of input rays to a bundle of output rays is no longer possible with a single deflective surface. This would decrease the ability of the secondary optical elements to correct for aberrations that would limit the concentration efficiency.

One may wonder, why not another way? Well, although it has not been proven here, this design has several advantages that distinguish it from other designs. For example, in other designs it is often the case that the primary optic and receiver move with respect to one another. Keep in mind that the receiver must be thermally bonded to a heat sink which is exposed to the external environment. In addition, the primary optic is also exposed to the external environment. It is difficult to envision a module enclosure where the required relative movement of both the receiver and primary optic would not significantly complicate the system. On the other hand, in the current design both the receiver and primary optic are fixed with respect to one another. Any motion of the secondary optic can occur completely within the enclosure which would be much easier to accomplish in practice.

Another benefit of this design is the absence of optical coupling, which in the past has been shown to severely degrade over the course of 20 years thus leading to severe performance degradation [5].

An alternative system could be to replace the outer freeform secondary mirror with a secondary mirror rotationally symmetric about the optical axis. There are two problems with this. The first is that a rotational symmetry poses a constraint which a freeform mirror simply does not have. The second is that even though both mirrors can be manufactured, the freeform mirror is smaller and thus less material is used. This is thought to outweigh any benefit the symmetry of the rotationally symmetric mirror might have to offer in terms of manufacturability.

Another alternative would be to use GRIN lenses, which would clearly yield superior performance, but unfortunately manufacturing concerns keep them from being a commercially viable product.

7.1.2 Mirror and Lens Manufacturability

With modern machining capabilities, it is possible to manufacture freeform surfaces such as the one in Figure 7.1. The primary optic is an aspheric surface and is capable of being manufactured by slow servo, diamond turning machines. For a small number of parts, it would be more practical to machine glass or plastic directly. However, on the large scale, a mold, typically made of aluminum, would have to be made and used for compression molding of glass or plastic.

For the mirrors, the surfaces lack any rotational symmetry and thus must be manufactured using a fast servo, diamond turning machine. Again, if only a few parts are needed they may be manufactured directly. However, a mold may be machined from aluminum if large scale production is required. Once the plastic part is made, its surface may be covered with a reflective coating to create a mirrored surface.

7.1.3 Assembly

From an economic standpoint, it is very important that the module be very easy to manufacture and have as many similarities with conventional manufacturing techniques as possible in order to mitigate the cost of developing new manufacturing techniques.

Overall, we essentially make use of a single sheet of glass (with lenses molded in), a sheet of steel and many identical components. Massive parallel assembly will enable the use of very small cells and thus passive thermal management with only a steel sheet backing to serve as a heat sink would be possible. This approach to thermal management has already been demonstrated by more than one company.

Figure 7.2 shows how a typical CPV module would normally be assembled. In Figure 7.3, we have an illustration of how an off-angle tracking module may be assembled. Only one additional assembly step is shown when going from one to the other. However, every detail of the assembly process depends on the exact design which is an open ended problem, so the illustrations serve only as a guide. This is especially true considering that there are a wide variety of different methods which could be implemented to actuate the secondary optical elements. In addition, the secondary optic itself adds to the complexity.

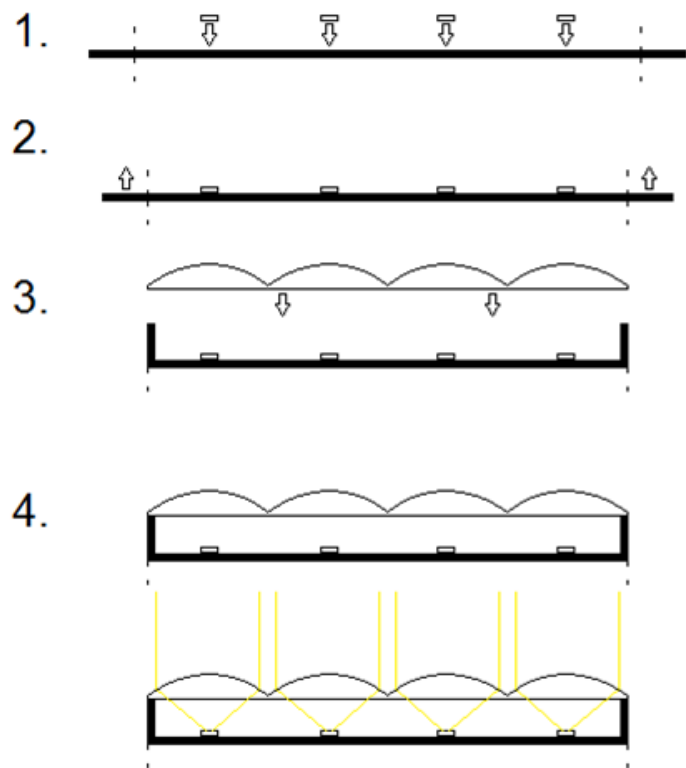


Figure 7.2 - Illustration of a simplified and hypothetical CPV module assembly.

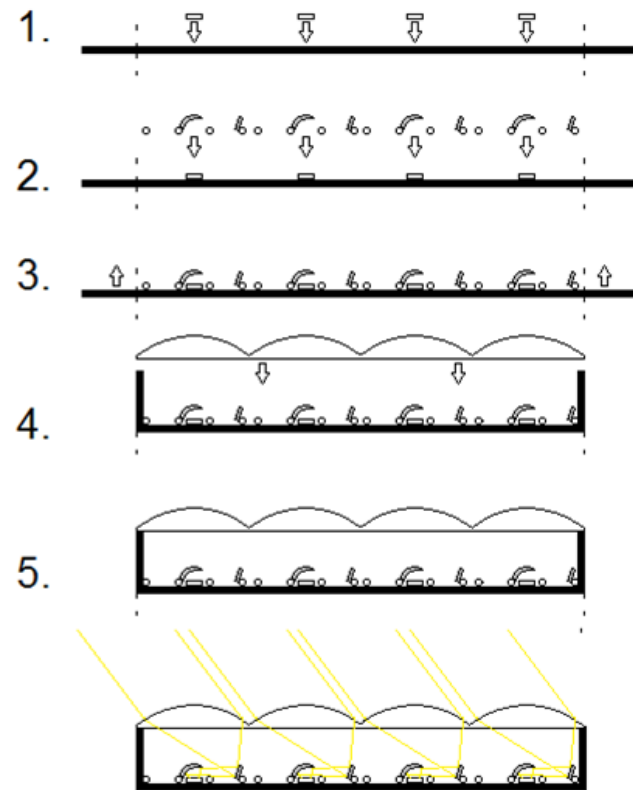


Figure 7.3 - Illustration a simplified and hypothetical off-angle tracking CPV module.

A top view of the secondary optical assembly is shown in Figure 7.4 below. Although the configuration given below is not final, the main point to take away is that it is self-contained. The ring along the perimeter could allow for simple actuation of the secondary optic. Actuating the device about the perimeter may allow one to take advantage of the small amount of leverage that is present rather than actuating the device from a point closer to the center.

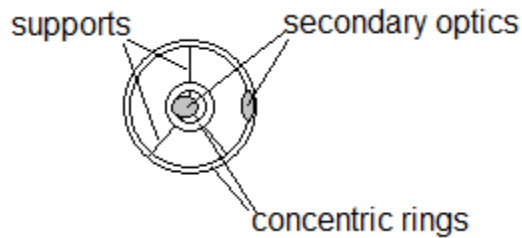


Figure 7.4 – Possible secondary optic configuration.

7.1.4 Receiver Symmetry

The present design takes advantage of rotational symmetry. Many systems usually have lenses with square apertures in order to allow for efficient tiling and compatibility with conventional square multi-junction photovoltaic cells. Although this has not been explored, these geometries may pose a bit of a problem when trying to maintain uniform illumination throughout the entire year. Instead, an alternative would be to utilize circular, or near circular cells in combination with hexagonal lens apertures. This would allow for efficient tiling while maintaining near circular symmetry. The exact trade-offs would have to be explored, but the option is clearly available as circular cells have already been manufactured by AZURSPACE [85] and patents have been filed by Concentrix Solar [86].

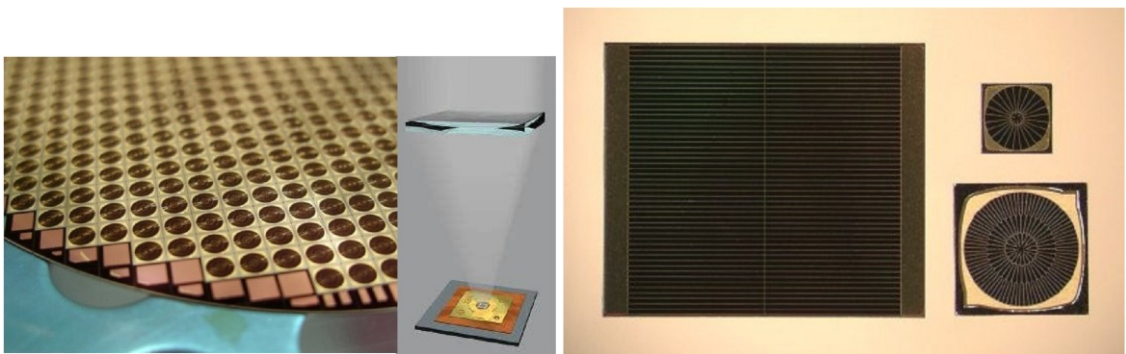


Figure 7.5 – Circular III-V Cells [85].

On the other hand, multi-junction photovoltaic cells are part of a relatively new technology that is constantly improving. If a significantly non-homogenous illumination is possible, square cells which are a more natural candidate from a cell manufacturing perspective could be ideal.

7.1.5 Louvered Tracking System

Although the use of single axis trackers is not new in photovoltaics, their use in high concentration photovoltaic (HCPV) system design is. Single axis external trackers are inherently less “bulky” than dual axis trackers and they offer several advantages in regards to the system’s mechanical design, which from a system level is just as important as the cell design.

Figure 7.6 shows an example of a louvered CPV system design from Phillips [87]. Clearly, there are several advantageous that are borrowed from the use of single axis trackers for linear concentrators which includes,

- Less space required than conventional 2 axis trackers
- Can be placed on inclined roofs and walls
- Reduction of wind forces on actuator because of less arm momentum
- Cheap tracking device due to one axis and low momentum

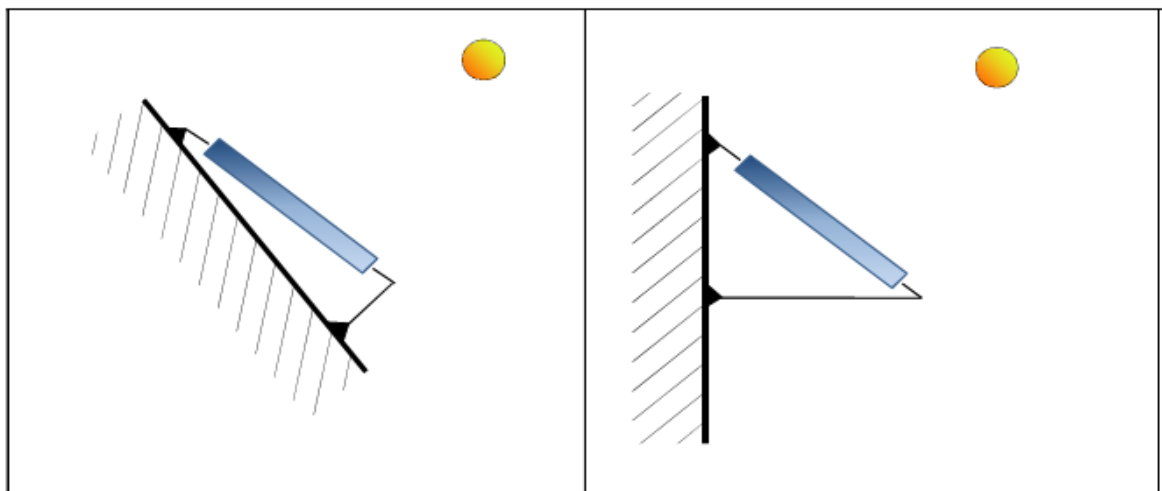


Figure 7.6 - Arrangement of a louvered tracking system from PHILLIPS which is analogous to what the off-angle tracking method allows for [87].

7.1.6 Internal Tracking System

There are two very important features of the internal tracking system that must be taken into account. The first feature is that seasonal motion is very slow, and so the motion of the secondary tracker needed to account for seasonal movement during any given day is on the order of 0.1 degrees. The second thing to consider is that, depending on how the system is configured, it may be required to move the internal tracker up to about 180° from one permitted alignment to another. This movement needs to happen at a reasonable pace since it is during this time that a daily interruption will occur when transitioning from one alignment to another.

It is possible that the best way of implementing the system would be to rotate each secondary individually. This individual rotation would also allow for some fine adjustment that would compensate for alignment errors for individual cells. However, it is more likely that synchronous motion of many secondary optical elements would be more economical.

Figure 7.7 below is an illustration of how synchronous motion of the entire array of secondary optics may be achieved. There are no major constraints on what the gears are made of and thus they could easily be formed by molded plastic parts so long as the shape of the gears was within a certain tolerance.

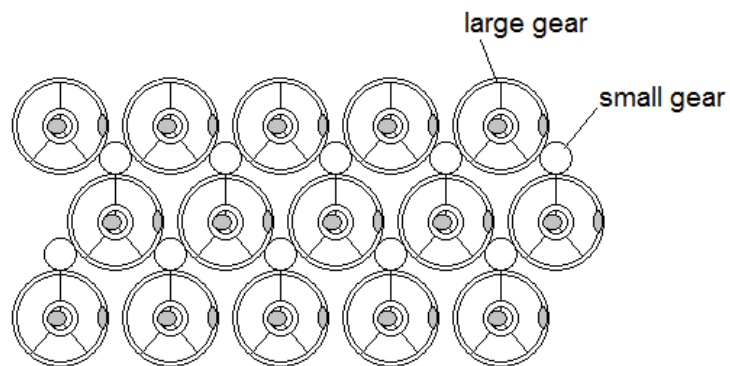


Figure 7.7 - Illustration of an array of secondary optical elements kept in synchronous motion through an intermediate gear assembly.

An alternative way of moving the secondary optics would be to use a toothed slider or worm gear to simultaneously move a row of secondary optical devices in synchronous motion, shown in Figure 7.8.

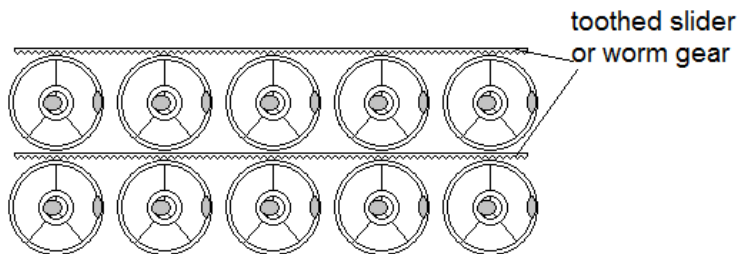


Figure 7.8 - Another possible way of simultaneously adjusting the secondary optical elements.

Figure 7.9 is an illustration of how a belt, chain, or other construct may be wrapped around multiple secondary optical components to allow for motion of the belt to move every secondary optical element in synchronous motion. Note that although it is not explicitly shown, if the belt or chain does not have sufficient rigidity, then tension must be placed on both ends. This might be achieved by using a spring or other such device.

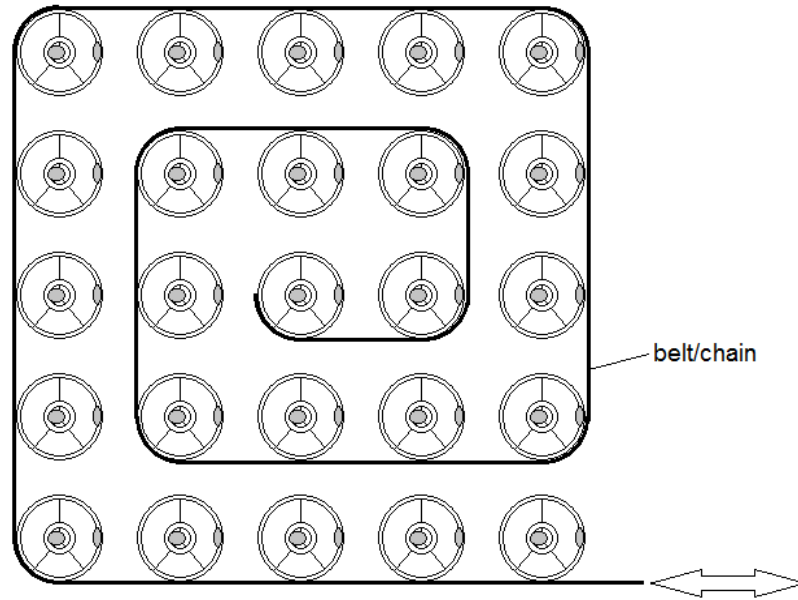


Figure 7.9 - Synchronous secondary optic movement achieved through a belt, chain or another long, flexible construct.

Below is an illustration of an array of joints made fixed relative to one another via some connector. The joints may exert a force on the rim of the secondary optic rim via a physical pivoting connection or an attractive magnetic or electrostatic force. In such a configuration all the secondary optical elements are forced to move in synchronous motion even if an actuator exerts a force directly on one secondary optical element.

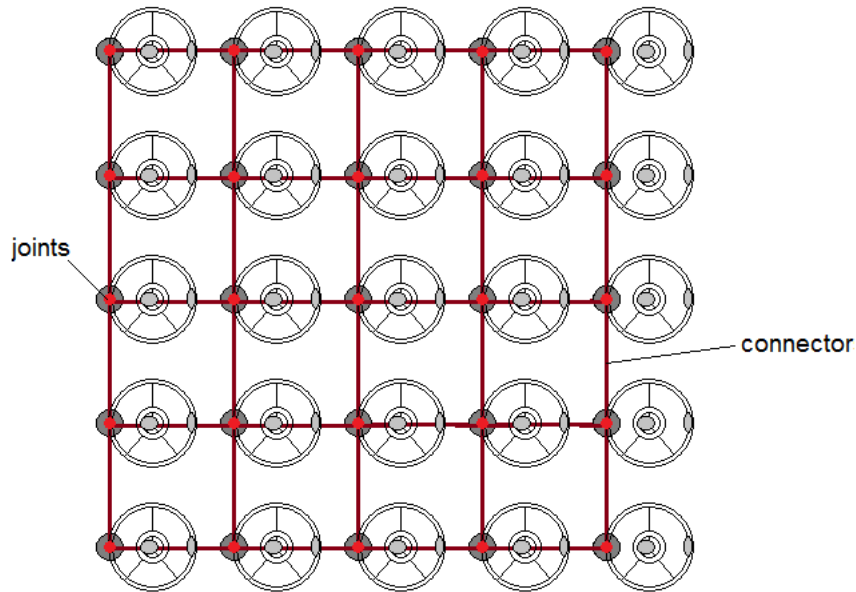


Figure 7.10 - Synchronous motion achieved with a stiff structure attached to pivoting joints on the secondary optical elements.

7.2 Lens Design

7.2.1 Specification

Equation (15) describes the primary optical surface. It is referred to as a polynomial asphere and consists of a several even ordered polynomial terms in superposition with a conic section term.

$$\frac{cr^2}{1 + \sqrt{1 - (1 + k)c^2r^2}} + c_4r^4 + c_6r^6 + c_8r^8 \quad (15)$$

The secondary optical mirrors are described by equation (16), which is a series of x and y polynomial terms up to the fourth order. This allows for the freedom to independently adjust the curvature along the x and y direction.

$$\begin{aligned} X1x + Y1y + X2x^2 + XYxy + Y2y^2 + X3x^3 + X2Yx^2y + XY2xy^2 \\ + Y3y^3 + X4x^4 + X3Yx^3y + X2Y2x^2y^2 + XY3xy^3 \\ + Y4y^4 \end{aligned} \quad (16)$$

We can find the optimal coefficients for the equations describing the optical surfaces via the LightTools optimization algorithms. In this case, we tried to optimize the performance for a source that subtended a 1° radius, the results are shown below.

Table 11 - Lens Specification (cm) for a off-axis convex plano lens with two reflective mirror secondaries.

Primary Front Surface		Outer Mirror		Inner Mirror	
Conic	0.09322	X	0	X	-0.01702

Constant					
Curvature	0.09511	Y	0	Y	0
4th aspheric	-2.4907e-005	X2	0.03373	X2	-0.08064
6th aspheric	-4.6770e-006	XY	0	XY	0
8th aspheric	7.3402e-008	Y2	0.004307	Y2	-0.09573
Diameter	10	X3	0.0039518	X3	0.02110
Depth	1.5	X2Y	0	X2Y	0
Refractive Index	1.5	XY2	0	XY2	0
Receiver Position	-13.5	Y3	0	Y3	0
		X4	-0.002669	X4	0
		X3Y	0	X3Y	0
		X2Y2	0	X2Y2	0
		XY3	0	XY3	0
		Y4	-0.0005658	Y4	0
		Diameter	5	Height	3
		X	5.0	Width	4
		Y	0	X	0
		Z	-11.5	Y	0
		Alpha	180	Z	-11.5
		Beta	-59.60	Alpha	0
		Gamma	0	Beta	47.21
				Gamma	0

7.2.2 Illumination Analysis

In our simulation, there are no losses due to absorption, scatter and reflection present. The reason is because the objective is to test for the performance of the system's basic geometry. The actual losses in this system are expected to be on par with the losses in any conventional system. The reason is due to the fact that the number of optical surfaces is limited to four and there are no significantly long path lengths through a highly absorbing medium.

An overview of the concentrator characteristics are summarized in Figure 7.13, Figure 7.14, Figure 7.15, Figure 7.16 and Figure 7.17. As illustrated in Table 12, given a certain receiver radius at 95% transmission, the numerical aperture for this concentrator is actually quite large. Figure 7.16 shows that the defined numerical aperture is not uniformly filled. As a consequence, although the concentration and acceptance angle seem reasonable, the defined thermodynamic efficiency limit is actually a bit low.

Table 12 - Étendue analysis results.

Acceptance Angle	1°	0.75°	0.5°
NA	0.7084	0.6715	0.6324
Receiver Radius	0.243 cm	0.2087 cm	0.183 cm
Aperture Étendue	$\epsilon_{\text{aper}} = 0.0681 \text{ cm}^2 \text{ sr}$	$\epsilon_{\text{aper}} = 0.0383 \text{ cm}^2 \text{ sr}$	$\epsilon_{\text{aper}} = 0.0170 \text{ cm}^2 \text{ sr}$
Receiver Étendue	$\epsilon_{\text{rcvr}} = 0.2925 \text{ cm}^2 \text{ sr}$	$\epsilon_{\text{rcvr}} = 0.1938 \text{ cm}^2 \text{ sr}$	$\epsilon_{\text{rcvr}} = 0.1322 \text{ cm}^2 \text{ sr}$
Thermodynamic Efficiency	$\eta_{\text{opticThermo}} = 22.12\%$	$\eta_{\text{opticThermo}} = 18.78\%$	$\eta_{\text{opticThermo}} = 12.24\%$
Concentration	384x	520x	677x

Another indication of étendue dilution is seen in Figure 7.11, where the edge rays clearly do not form a stigmatic image.

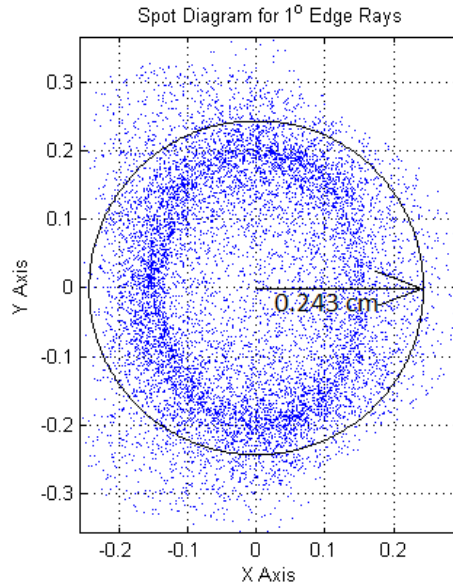


Figure 7.11 - Edge rays for a 1° radius source.

The reason for this étendue dilution becomes apparent when viewing Figure 7.12. The first step to improving the efficiency according to our given definition would likely be to make the angular extent of the incident rays more symmetrical about the receiver normal.

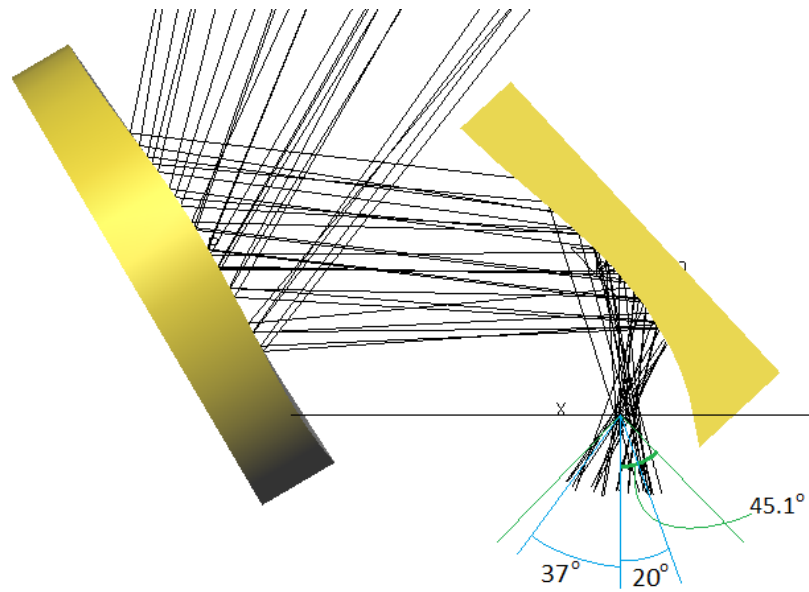


Figure 7.12 - Secondary cross-section showing how the NA is not completely filled; the 37° and 20° extent along the L axis correspond to the extent seen in Figure 7.16.

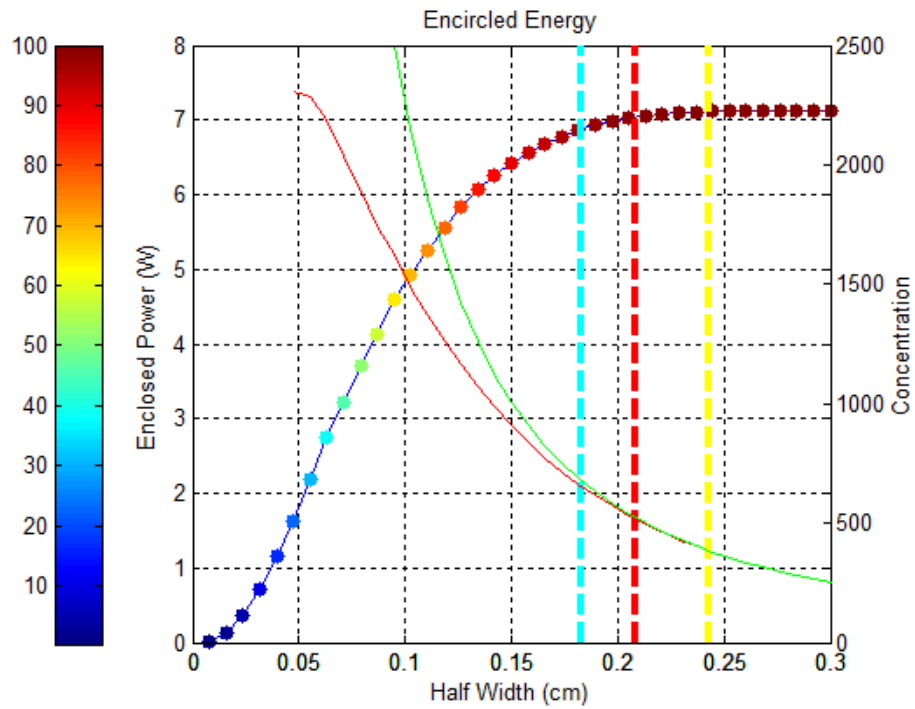


Figure 7.13 – Encircled energy diagram for the off-axis concentrator with dual freeform mirrors; the peak energy incident is 7.1181 W.

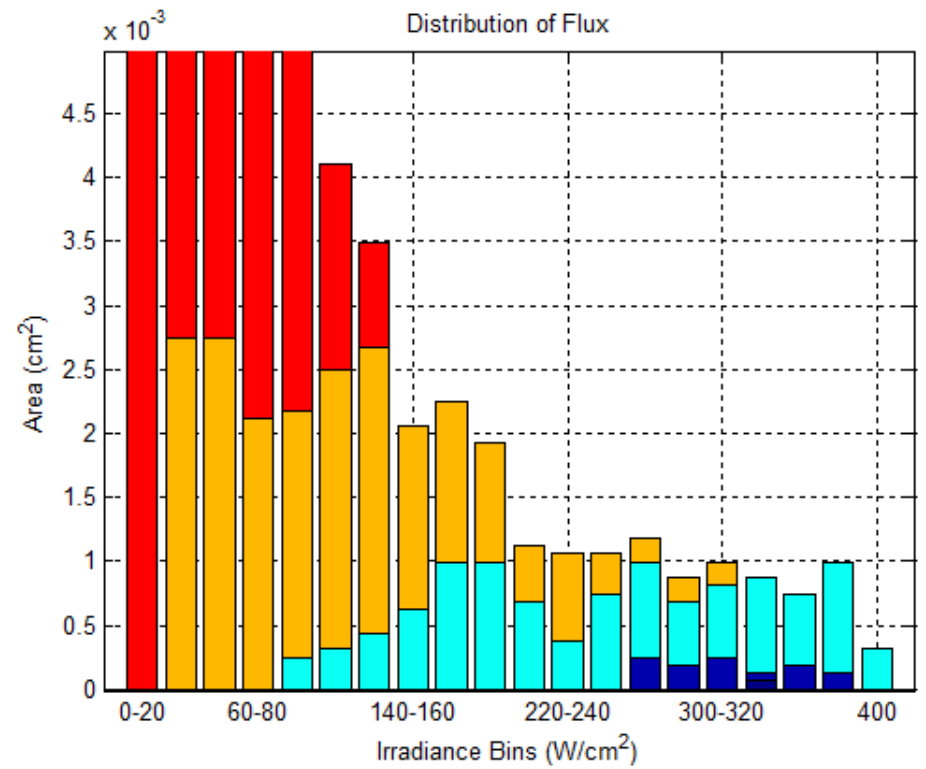


Figure 7.14 – Irradiance distribution histogram for the off-axis concentrator with dual freeform mirrors.

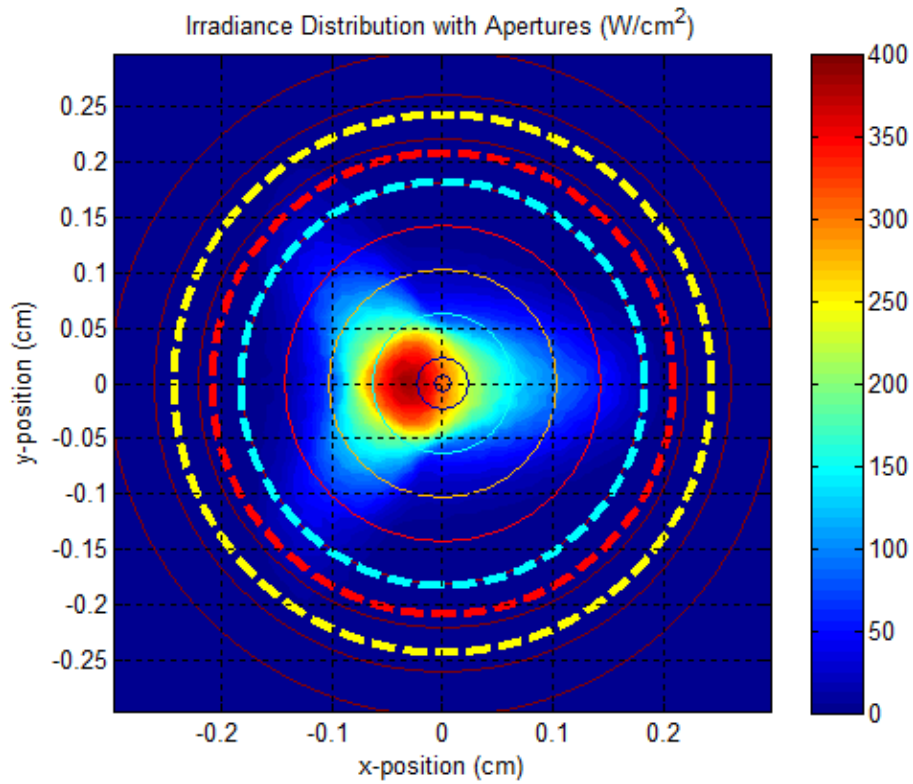


Figure 7.15 – Irradiance distribution diagram for the off-axis concentrator with dual freeform mirrors.

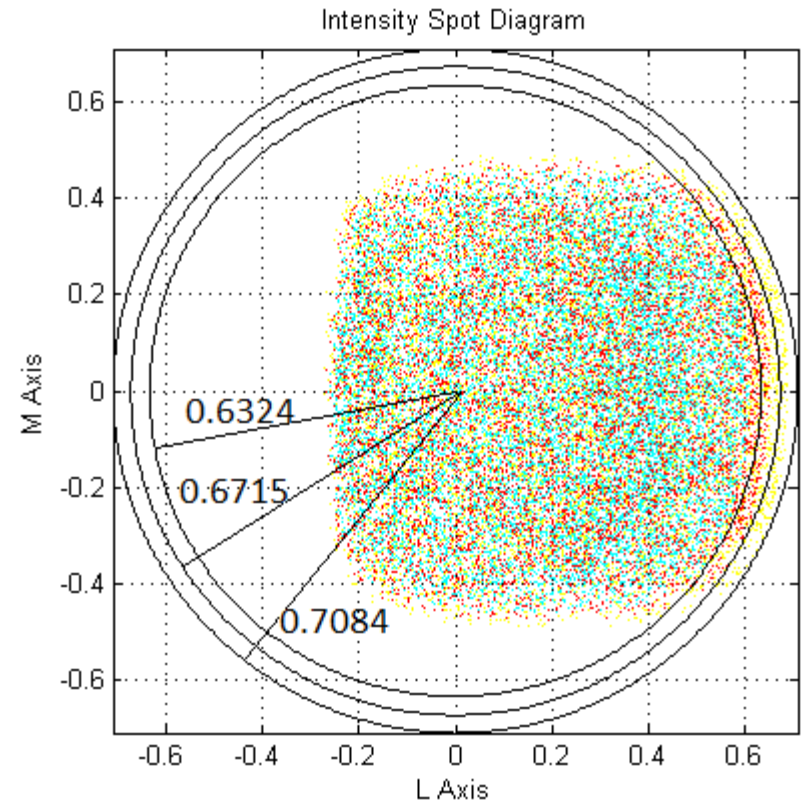


Figure 7.16 – Intensity spot diagram of rays from a 1° half angled source; the illustration is intended to show the angular extent of the rays within the 0.243cm radius receiver.

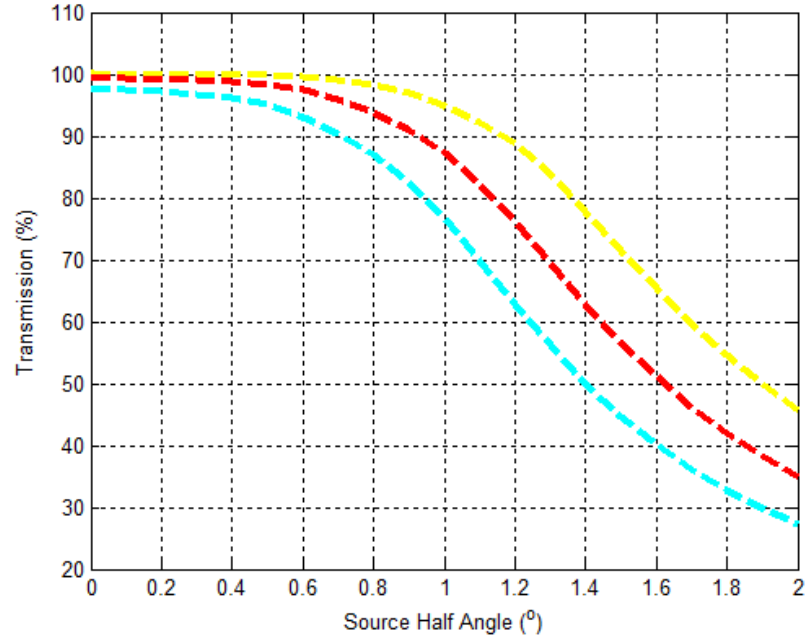


Figure 7.17 - Transmission for sources of a 0.5° (cyan), 0.75° (red) and 1° (yellow) half-angle.

8 Conclusion

The goal of this project was to create an integrated CPV design. Fundamental research on silicon photovoltaics has been ongoing since about 1954, and research on semiconductor technology has been carried out for about 50 years before that. However, what has yet to be achieved is to create a cost effective integrated CPV module which is actually an interdisciplinary problem that draws on the knowledge of experts traditionally outside of the photovoltaic R&D community. More specifically, an integrated design should be able to achieve synergy between different CPV components. This would allow for a more effective CPV system than when compared to the conventional modular design where each component, such as the tracker and optics, are considered somewhat independently.

Of course basic R&D undoubtedly plays an important role in the exploration of potentially viable and fundamentally new ideas related to photovoltaics. However, capitalizing on existing technology by creatively applying existing concepts in new, creative ways has been a proven method of packaging traditionally separate technologies into something novel. For example, the development of building integrated photovoltaics and maximum power point tracking does not involve anything fundamentally new to science. However, both of these topics are still active areas of research which are important to the photovoltaic industry. Ideas are common in science, but innovation, by definition, happens only once these ideas are embodied by a commercially viable product.

Along these lines of reasoning, the result of this investigation has led to a concept dubbed “off-angle tracking”. The concept was only found after a thorough, independent investigation of both technical and economic constraints whilst having ideas such as laterally moving receivers and integrated system design in mind.

The design concept was investigated further until eventually arriving at the final presented design. It is the author’s opinion that the optics in all of the presented designs can be optimized much further using more advanced optimization techniques not readily available in commercial software. This has not been carried out in the interest of time. Instead, the focus has been placed on the configuration of different optical components in the interest of achieving optimal functionality. In a broad sense, the reason is because this task is best addressed using the spatial and broad problem solving ability of human reasoning. The more iterative problem solving associated with optimization of lens curvatures can be carried out more carefully at a later time by using a computer.

The final presented design is not intended to be the *best* solution. It is only intended to be an example of a good solution that meets various constraints associated with CPV systems. These constraints include, but are not limited to acceptance angle, concentration, and

manufacturability. The details of such trade-offs have been illustrated and are also subject to change in the face of changes in available technology.

It should be noted that the striking contrast between the performance metrics of the final presented off-axis concentrator and the on-axis concentrators should not be a deterrent for further investigation. Freeform surfaces are quite difficult to work with from a design standpoint, which is probably because manufacturing them has only recently become commercially viable. Most of the effort in this project was placed on looking at the "big picture" in order to determine a good configuration for the optical components to achieve a great deal of freedom and functionality. In addition, GRIN lenses provide an example of an already existing ideal optical solution. Thus, as argued throughout the thesis, there do not appear to be any technical limitations preventing a more ideal solution from being found.

Possible next steps in the continuation of this project depend largely on whether it is classified as being basic research and development, or if it is classified as being early stage commercial development. How the present project is classified makes a difference because it distinguishes what aspects of the development are emphasized and which ones are not. For instance, if considered a basic research and development project, exploration of the use of gradient index optics from a theoretical standpoint may be an interesting starting point. However, GRIN lenses, although becoming more feasible, would be prohibitively expensive in CPV applications in the near term. However, if early stage commercial development is the goal, freeform surfaces should be the extent of optical design exploration. So, in the author's opinion this question must be answered before considering any one of the many possible avenues of exploration.

References

- [1] J. H. Ermer, R. K. Jones, P. Hebert, P. Pien, R. R. King, D. Bhusari, R. Brandt, O. Al-Taher, C. Fetzer, G. S. Kinsey, and N. Karam, "Status of C3MJ and C4MJ Production Concentrator Solar Cells at Spectrolab," *Photovoltaics, IEEE Journal of*, vol. 2, no. 2, pp. 209–213, Apr. 2012.
- [2] R. M. Swanson, "The promise of concentrators," *Progress in Photovoltaics: Research and Applications*, vol. 8, no. 1, pp. 93–111, Jan. 2000.
- [3] R. R. King, R. A. Sherif, G. S. Kinsey, S. R. Kurtz, C. M. Fetzer, and K. M. Edmondson, "Bandgap Engineering in High-Efficiency Multijunction Concentrator Cells," presented at the International Conference on Solar Concentrators for the Generation of Electricity or Hydrogen, Scottsdale, Arizona, 2005.
- [4] R. R. King, D. Bhusari, D. Larrabee, X.-Q. Liu, E. Rehder, K. Edmondson, H. Cotal, R. K. Jones, J. H. Ermer, C. M. Fetzer, D. C. Law, and N. H. Karam, "Solar cell generations over 40% efficiency," *Progress in Photovoltaics: Research and Applications*, p. n/a–n/a, 2012.
- [5] S. R. Kurtz, "Opportunities and Challenges for Development of a Mature Concentrating Photovoltaic Power Industry," National Renewable Energy Laboratory, Golden Colorado, Technical Report NREL/TP-520-43208, Jun. 2011.
- [6] R. Jones, "Terrestrial PV Technology from the Aerospace Industry," 12500 Gladstone Avenue, 10-Mar-2008.
- [7] D. M. Powell, M. T. Winkler, H. J. Choi, C. B. Simmons, D. B. Needleman, and T. Buonassisi, "Crystalline silicon photovoltaics: a cost analysis framework for determining technology pathways to reach baseload electricity costs," *Energy & Environmental Science*, vol. 5, no. 3, p. 5874, 2012.
- [8] M. A. Green, "Efficiency limits for photovoltaic solar energy conversion," in *Technology and Application*, Rome, 2002.
- [9] "National Center for Photovoltaics," *NREL*, 23-Jul-2012. [Online]. Available: <http://www.nrel.gov/ncpv/>. [Accessed: 23-Oct-2012].
- [10] M. A. Green, K. Emery, Y. Hishikawa, W. Warta, and E. D. Dunlop, "Solar cell efficiency tables (version 40)," *Progress in Photovoltaics: Research and Applications*, vol. 20, no. 5, pp. 606–614, 2012.
- [11] J. Zhao, A. Wang, M. A. Green, and F. Ferrazza, "19.8% efficient 'honeycomb' textured multicrystalline and 24.4% monocrystalline silicon solar cells," *Applied Physics Letters*, vol. 73, no. 14, pp. 1991–1993, Oct. 1998.
- [12] "Record 44 Percent CPV Efficiency From Startup Solar Junction: Greentech Media." [Online]. Available: <http://www.greentechmedia.com/articles/read/Record-44-Percent-CPV-Efficiency-From-Startup-Solar-Junction>. [Accessed: 23-Oct-2012].
- [13] N. Gregory F., "Beyond the learning curve: factors influencing cost reductions in photovoltaics," *Energy Policy*, vol. 34, no. 17, pp. 3218–3232, Nov. 2006.

- [14] "Polysilicon Prices in 2012: The Tipping Point For Solar," *Investment U.* [Online]. Available: <http://www.investmentu.com/2012/January/polysilicon-green-energy.html>. [Accessed: 02-Dec-2012].
- [15] H. of Department, "Event - Martin Green - The Physics of High Efficiency Photovoltaic Solar Energy Conversion - Theoretical Physics - ANU." [Online]. Available: <http://physics.anu.edu.au/theophys/events.php?EventID=62>. [Accessed: 14-Oct-2012].
- [16] J. C. Miñano, P. Benítez, and A. Santamaría, "Free-form optics for illumination," *Optical Review*, vol. 16, no. 2, pp. 99–102, Jun. 2010.
- [17] P. Benítez, J. C. Miñano, J. Blen, R. Mohedano, J. Chaves, O. Dross, M. Hernández, and W. Falicoff, "Simultaneous multiple surface optical design method in three dimensions," *Optical Engineering*, vol. 43, p. 1489, 2004.
- [18] Y. Chen, "Thermal Forming Process for Precision Freeform Optical Mirrors and Micro Glass Optics," M.Sc., The Ohio State University, Ohio, 2010.
- [19] Y. E. Tohme and J. A. Lowe, "Machining of freeform optical surfaces by slow slide servo method," in *ASPE*, 2003.
- [20] A. Y. Yi, C. Huang, F. Klocke, C. Brecher, G. Pongs, M. Winterschladen, A. Demmer, S. Lange, T. Bergs, M. Merz, and F. Niehaus, "Development of a compression molding process for three-dimensional tailored free-form glass optics," *Appl. Opt.*, vol. 45, no. 25, pp. 6511–6518, 2006.
- [21] "Fundamentals of ultraprecision machining," *Machine Design*, 10-May-2012.
- [22] A. Y. Yi and L. Li, "Design and fabrication of a microlens array by use of a slow tool servo," *Opt. Lett.*, vol. 30, no. 13, pp. 1707–1709, Jul. 2005.
- [23] T. Levi-Civita, "Complementi al teorema di Malus-Dupin. Nota I," *Rend. Sedute R. Accad. Dei Lincei IX (1)*, pp. 185–189, 1900.
- [24] É. L. Malus, *Mémoire sur l'Optique: (Càtoptrique), Dioptrique*. 1808.
- [25] E. L. Malus, *Mémoires de mathématiques et de physique*. Baudouin, imprimeur de l'Institut, 1811.
- [26] M. Born and E. Wolf, *Principles of Optics*, 7th expanded. Cambridge: Cambridge University Press, 2003.
- [27] R. Winston, J. C. Minano, and P. Benitez, *Nonimaging Optics*. Elsevier Academic Press.
- [28] M. A. Green, *Silicon solar cells: advanced principles & practice*. Centre for Photovoltaic Devices and Systems, University of New South Wales, 1995.
- [29] A. Martí and G. L. Araújo, "Limiting efficiencies for photovoltaic energy conversion in multigap systems," *Solar Energy Materials and Solar Cells*, vol. 43, no. 2, pp. 203–222, Sep. 1996.
- [30] G. L. Araújo and A. Martí, "Absolute limiting efficiencies for photovoltaic energy conversion," *Solar Energy Materials and Solar Cells*, vol. 33, no. 2, pp. 213–240, Jun. 1994.
- [31] S. Burroughs, R. Conner, B. Furman, E. Menard, A. Gray, M. Meitl, S. Bonafede, D. Kneeburg, K. Ghosal, R. Bukovnik, W. Wagner, and S. Seel, "A New Approach For A Low

- Cost CPV Module Design Utilizing Micro-Transfer Printing Technology,” Semprius Inc., Kiara, 10600 Baden Place, Raleigh, NC 27613 USA, White Paper, 2010.
- [32] “Useful Constants,” *International Earth Rotation and Reference Systems Service*, 29-Mar-2010. [Online]. Available: <http://hpiers.obspm.fr/eop-pc/models/constants.html>.
- [33] J. Haigh, “Solar influences on the Climate,” Imperial College London, Grantham Institute for Climate Change, Briefing Paper, Feb. 2011.
- [34] “Numerical Standards for Fundamental Astronomy,” *International Earth Rotation and Reference Systems Service*, 2009. [Online]. Available: http://maia.usno.navy.mil/NSFA/IAU2009_consts.html. [Accessed: 03-Sep-2012].
- [35] “Orbital Ephemerides of the Sun, Moon, and Planets.” International Astronomical Union Commission.
- [36] M. Emilio, J. R. Kuhn, R. I. Bush, and I. F. Scholl, “Measuring the Solar Radius from Space During the 2003 and 2006 Mercury Transits,” *The Astrophysical Journal*, vol. 750, no. 2, p. 135, May 2012.
- [37] D. R. Williams, “Sun Fact Sheet,” NASA, 02-Mar-2012. [Online]. Available: <http://nssdc.gsfc.nasa.gov/planetary/factsheet/sunfact.html>. [Accessed: 24-Sep-2012].
- [38] J. R. Kuhn, R. Bush, M. Emilio, and I. F. Scholl, “The Precise Solar Shape and Its Variability,” *Science*, Aug. 2012.
- [39] P. T. Landsberg and V. Badescu, “The geometrical factor of spherical radiation sources,” *Europhysics Letters (EPL)*, vol. 50, no. 6, pp. 816–822, Jun. 2000.
- [40] G. Kopp and J. L. Lean, “A new, lower value of total solar irradiance: Evidence and climate significance,” *Geophys. Res. Lett.*, vol. 38, no. 1, p. L01706, Jan. 2011.
- [41] C. A. Gueymard, *SMARTS2, A Simple Model of the Atmospheric Radiative Transfer of Sunshine: Algorithms and performance assessment*. .
- [42] A. Neumann, A. Witzke, S. A. Jones, and G. Schmitt, “Representative Terrestrial Solar Brightness Profiles,” *J. Sol. Energy Eng.*, vol. 124, no. 2, pp. 198–204, May 2002.
- [43] A. Bett, F. Ferrazza, J. Herzog, A. Marti, and W. Wettling, “Concentration Photovoltaics (CPV),” Fraunhofer ISE, Europe, Report, Oct. 2006.
- [44] Y.-Y. Liu, “Analysis of Structural Deformation and Concentrator Misalignment in a 5-kW Solar Tracker,” M.Sc., National Central University, Taiwan, 2010.
- [45] “Advanced optics for CPV,” Philadelphia, 07-Jun-2009.
- [46] G. Galbraith, “Development and evaluation of a tracking error monitor for solar trackers,” Sandia National Laboratory, United States, Sandia Report SAND-88-7025, Oct. 1988.
- [47] A. L. Luque and V. Andreev, Eds., “Inspira’s CPV Sun Tracking,” in *Concentrator Photovoltaics*, vol. 130, Berlin, Heidelberg: Springer Berlin Heidelberg, 2007, pp. 221–251.
- [48] I. Luque-Heredia, “Equipment and Process for Measuring the Precision of Sun Tracking for Photovoltaic Concentrators,” U.S. Patent 2008/025805123-Oct-2008.

- [49] R. Cervantes, G. Quemere, and I. Luque-Heredia, "Sunspear Calibration Against Array Power Output for Tracking Accuracy Monitoring in Solar Concentrators," in *EU PVSEC Proceedings*, Valencia, Spain, 2008, pp. 890 – 893.
- [50] I. Luque-Heredia, R. Cervantes, and G. Quemere, "A Sun Tracking Error Monitor for Photovoltaic Concentrators," in *2006 IEEE 4th World Conference on Photovoltaic Energy Conference*, Waikoloa, HI, 2006, pp. 706–709.
- [51] C. Cancro, G. Graditi, G. Leanza, F. Pascarella, A. Sarno, and D. Mancini, "Field testing of the PhoCUS solar tracker by means of a novel optoelectronic device," in *4 th International Conference on Solar Concentrators for the Generation of Electricity or Hydrogen, San Lorenzo del Escorial, Spain*, 2007, pp. 12–16.
- [52] M. Davis, J. Lawler, J. Coyle, A. Reich, and T. Williams, "Machine vision as a method for characterizing solar tracker performance," in *33rd IEEE Photovoltaic Specialists Conference, 2008. PVSC '08*, 2008, pp. 1 –6.
- [53] R. O. Campbell and M. Machado, "Tracking Concentrator Employing Inverted Off-Axis Optics and Method," U.S. Patent WO 2010/00915421-Jan-2010.
- [54] Ro. Bijl and P. Peter, "Device For Converting Solar Energy," U.S. Patent WO2007117136 A118-Oct-2007.
- [55] N. Tomonori, T. Kyoichi, and H. Kouetsu, "Light Converging Solar Module," U.S. Patent 570745813-Jan-1998.
- [56] F. Duerr, Y. Meuret, and H. Thienpont, "Tracking integration in concentrating photovoltaics using laterally moving optics," *Opt. Express*, vol. 19, no. S3, pp. A207–A218, May 2011.
- [57] F. Duerr, "Free form optics for a linear field of view," Washington, DC, 30-Oct-2011.
- [58] P. Kotsidas, V. Modi, and J. M. Gordon, "Nominally stationary high-concentration solar optics by gradient-index lenses," *Opt. Express*, vol. 19, no. 3, pp. 2325–2334, Jan. 2011.
- [59] J. M. Gordon, P. Kotsidas, and V. Modi, "Spherical Gradient Index (GRIN) Lenses and their uses in Solar Concentration," U.S. Patent WO/2012/033840.
- [60] P. Benitez, A. Cvetkovic, R. Winston, G. Diaz, L. Reed, J. Cisneros, A. Tovar, A. Ritschel, and J. Wright, "High-Concentration Mirror-Based Kohler Integrating System for Tandem Solar Cells," in *Conference Record of the 2006 IEEE 4th World Conference on Photovoltaic Energy Conversion*, 2006, vol. 1, pp. 690–693.
- [61] A. Tomlinson, "OFFSET CONCENTRATOR OPTIC FOR CONCENTRATED PHOTOVOLTAIC SYSTEMS," U.S. Patent WO/2011/06154926-May-2011.
- [62] R. Winston and W. Zhang, "LOW COST HIGH EFFICIENCY SOLAR CONCENTRATOR WITH TRACKING RECEIVERS," U.S. Patent WO/2012/03073108-Mar-2012.
- [63] S. E. Calico, "Feasibility of Photovoltaic Cells on a Fixed Mirror Distributed Focus Solar Bowl," M.Sc., Texas Tech University, 1986.
- [64] E. M. Kritchman, "A fixed Fresnel lens with tracking collector," *Solar Energy*, vol. 27, no. 1, pp. 13–17.

- [65] G. Bachmaier, D. Berggmann, M. Gerlich, and O. Hennig, "PASSIVE FINE-ADJUSTMENT CONCEPT FOR CPV PLANTS," U.S. Patent WO/2012/066062.
- [66] J. E. Ford, J. H. Karp, E. J. Tremblay, and J. M. Hallas, "System and Method for solar energy capture and related method of manufacturing," U.S. Patent WO2010/033859 A2.
- [67] J. H. Karp, E. J. Tremblay, and J. E. Ford, "Planar micro-optic solar concentrator," *Opt. Express*, vol. 18, no. 2, pp. 1122–1133, Jan. 2010.
- [68] J. H. Karp, E. J. Tremblay, J. M. Hallas, and J. E. Ford, "Orthogonal and secondary concentration in planar micro-optic solar collectors," *Opt. Express*, vol. 19, no. S4, pp. A673–A685, Jul. 2011.
- [69] J. M. Hallas, K. A. Baker, J. H. Karp, E. J. Tremblay, and J. E. Ford, "Two-axis solar tracking accomplished through small lateral translations," *Appl. Opt.*, vol. 51, no. 25, pp. 6117–6124, Sep. 2012.
- [70] K. A. Baker, J. H. Karp, E. J. Tremblay, J. M. Hallas, and J. E. Ford, "Reactive self-tracking solar concentrators: concept, design, and initial materials characterization," *Applied Optics*, vol. 51, no. 8, pp. 1086–1094, Mar. 2012.
- [71] M. Brunotte, A. Goetzberger, and U. Blieske, "Two-stage concentrator permitting concentration factors up to 300x with one-axis tracking," *Solar Energy*, vol. 56, no. 3, pp. 285–300, Mar. 1996.
- [72] A. Mohr, T. Roth, and S. W. Glunz, "BICON: high concentration PV using one-axis tracking and silicon concentrator cells," *Progress in Photovoltaics: Research and Applications*, vol. 14, no. 7, pp. 663–674, Nov. 2006.
- [73] S. Bouchard and S. Thibault, "Planar waveguide concentrator used with a seasonal tracker," *Appl. Opt.*, vol. 51, no. 28, pp. 6848–6854, Oct. 2012.
- [74] M. J. Clifford and D. Eastwood, "Design of a novel passive solar tracker," *Solar Energy*, vol. 77, pp. 269–280, 2004.
- [75] C. Li, Y. Liu, X. Huang, and H. Jiang, "Direct Sun-Driven Artificial Heliotropism for Solar Energy Harvesting Based on a Photo-Thermomechanical Liquid-Crystal Elastomer Nanocomposite," *Advanced Functional Materials*, p. n/a–n/a, 2012.
- [76] S. P. Hines, "Solar tracker," U.S. Patent 779998721-Sep-2010.
- [77] M. Rabinowitz and M. Davidson, "Electronic film with embedded micro-mirrors for solar energy concentrator systems," *Solar energy*, vol. 77, no. 1, pp. 3–13, 2004.
- [78] M. Rabinowitz, "Micro-optics Solar Energy Concentrator," U.S. Patent 2005/0195465 A108-Sep-2005.
- [79] F. Duerr, P. Benítez, J. C. Miñano, Y. Meuret, and H. Thienpont, "Integrating tracking in concentrating photovoltaics using non-rotational symmetric laterally moving optics," *Proceedings of SPIE*, vol. 8124, no. 1, p. 81240M–81240M–7, Sep. 2011.
- [80] J. M. Gordon, "Spherical Gradient-Index Lenses as Perfect Imaging and Maximum Power Transfer Devices," *Appl. Opt.*, vol. 39, no. 22, pp. 3825–3832, 2000.

- [81] P. Kotsidas, V. Modi, and J. M. Gordon, "Gradient-index lenses for near-ideal imaging and concentration with realistic materials," *Opt. Express*, vol. 19, no. 16, pp. 15584–15595, 2011.
- [82] K. K. Chong and C. W. Wong, "General formula for on-axis sun-tracking system and its application in improving tracking accuracy of solar collector," *Solar Energy*, vol. 83, no. 3, pp. 298–305, Mar. 2009.
- [83] A. B. Sproul, "Derivation of the solar geometric relationships using vector analysis," *Renewable Energy*, vol. 32, no. 7, pp. 1187–1205, Jun. 2007.
- [84] A. B. Sproul, "Erratum to 'Derivation of the solar geometric relationships using vector analysis': [Renew. Energy 32 (2007) 1187-1205]," *Renewable Energy*, vol. 32, no. 15, p. 2642, Dec. 2007.
- [85] G. F. X. Strobl, "From Space to Earth: 3rd Generation of Photovoltaics," Madrid, Spain, 02-Apr-2008.
- [86] S. V. Riesen and A. Gombert, "Solar cell chips with new geometry and method for manufacturing the same," U.S. Patent US2011/0247672 A1.
- [87] H. Zahn, S. Box, C. ter Laak, J. Schroen, and R. Wijnen, "Low cost, louvered CPV design," 22-Oct-2010.
- [88] N. Shatz, J. Bortz, and R. Winston, "Thermodynamic efficiency of solar concentrators," *Opt. Express*, vol. 18, no. S1, pp. A5–A16, Apr. 2010.
- [89] A. Conway and J. L. Synge, Eds., *The Mathematical Papers of Sir William Rowan Hamilton Vol. 1 Geometrical Optics*, vol. 1, 4 vols. Great Britain: Cambridge University Press, 1931.
- [90] J. L. Synge, *Geometrical Optics - An Introduction to Hamilton's Method*. Great Britain: The Cambridge University Press, 1962.

Appendix I. Étendue Metric

One way of quantifying the loss is by comparing the étendue at the input aperture and receiver. If they are equal, the system is said to be thermodynamically efficient. We may define a metric [88] to quantify the thermodynamic efficiency of the lens as,

$$\eta_{opticalThermo} = \eta_{optical} \min\left(1, \frac{\epsilon_{aper}}{\epsilon_{rcvr}}\right)$$

Where,

$$\epsilon_{aper} = A_{aper} \pi \sin(\theta_{aper})^2$$

And,

$$\epsilon_{rcvr} = A_{rcvr} \pi \sin(\theta_{rcvr})^2$$

Where θ_{aper} and θ_{rcvr} are the half angles of the acceptance angle cones. We also know that the aperture size is given by,

$$A_{aper} = \cos(\theta_{aper}) \pi R_{aper}^2$$

And the size of the receiver is given by,

$$A_{rcvr} = \pi R_{rcvr}^2$$

Where R_{aper} and R_{rcvr} are the radius of the aperture and receiver respectively.

Appendix II. Geometric Optics and the Application of the Characteristic Equation

Introduction

In modern times, computer ray tracing simulations have in a very large way displaced the analytical methods used to design optics in the past. In some ways, this is for a very good reason. Computers are far more flexible than analytical methods. Computers also offer friendly user interfaces which allows for a user to get away with treating the program like a black box. This is also unlike analytical methods where the user must understand how and when to apply any given equation and/or assumption. This then begs the question, why study analytical methods at all? If one is willing to surmount the initial learning curve, analytical methods provide a more intuitive and efficient insight into how a few very important optical surfaces behave. From a conceptual point of view, this insight is very useful and can even help one be more efficient at using ray tracing software. In addition, there is no reason why the results of some analytical expressions cannot also be implemented into software.

Overview

In 1832, Sir William Rowan Hamilton introduced the characteristic function, which, within the context of geometric optics, provides a general method for describing how light propagates through a medium [89]. Although the characteristic function provides invaluable theoretical insight, historically the characteristic function has not been considered practical and in more recent times, Monte Carlo simulations have also gained popularity. Despite this, it is still useful to obtain an analytical form of Hamilton's characteristic function for simple, yet common optical surfaces used for solar energy applications. Here, we discuss the background leading up to the characteristic function described in [90], and then provide an example of a 2D parabolic trough.

All of ray optics may be derived through the Euler-Lagrange equations,

$$\frac{\partial L}{\partial \mathbf{x}} - \frac{d}{d\sigma} \frac{\partial L}{\partial \mathbf{x}'} = 0$$

Once solved, we obtain an equation for the optical path length between points P_0 and P_1 given by,

$$S = \int_{P_0}^{P_1} L d\sigma = \int_{P_0}^{P_1} \mathbf{p} \cdot \mathbf{x}' d\sigma$$

Hamilton's characteristic function is defined as,

$$V = S(\mathbf{P}_1) - S(\mathbf{P}_0)$$

The "optical momentum" at P_0 and P_1 is given by the following six equations,

$$p_1^0 = -\frac{\partial V}{\partial x_1^0}, p_2^0 = -\frac{\partial V}{\partial x_2^0}, p_3^0 = -\frac{\partial V}{\partial x_3^0}$$

$$p_1^1 = \frac{\partial V}{\partial x_1^1}, p_2^1 = \frac{\partial V}{\partial x_2^1}, p_3^1 = \frac{\partial V}{\partial x_3^1}$$

And the following identity comes from the definition of optical momentum,

$$p_1^0{}^2 + p_2^0{}^2 + p_3^0{}^2 = n^2$$

$$p_1^1{}^2 + p_2^1{}^2 + p_3^1{}^2 = n^2$$

Taking the Legendre Transform⁷ of the characteristic function, we obtain the angular characteristic function,

$$T = V + \sum_{i=1}^3 p_i^0 x_i^0 - \sum_{k=1}^3 p_k^1 x_k^1$$

And the corresponding ray equations,

$$x_1^0 - \frac{p_1^0}{p_3^0} x_3^0 = \frac{\partial T}{\partial p_1^0}, \quad x_2^0 - \frac{p_2^0}{p_3^0} x_3^0 = \frac{\partial T}{\partial p_2^0}$$

$$x_1^1 - \frac{p_1^1}{p_3^1} x_3^1 = -\frac{\partial T}{\partial p_1^1}, \quad x_2^1 - \frac{p_2^1}{p_3^1} x_3^1 = -\frac{\partial T}{\partial p_2^1}$$

In this case we have assumed a homogeneous index of refraction and made use of the following identity to reduce the six equations to four,

$$p_3 = \sqrt{n^2 - p_1^2 - p_2^2}$$

Thus, we also have,

$$T = T(p_1^0, p_2^0, p_1^1, p_2^1)$$

⁷ If $F(x)$ is a continuous convex function, the Legendre transform is defined as $G(s) = s x(s) - F(x(s))$ where $s(x) = \frac{d}{dx} F(x)$

Reducing six coordinate variables to four momentum variables will often reduce the complexity of practical problems.

Parabola Example

In this case, the angular characteristic function is given as,

$$T(p0_2, p1_2) = (p0_2 - p1_2) x_2 + (p0_3 - p1_3) x_3 \quad (17)$$

The objective is to use Fermat's principle by finding the extremum of the angular characteristic function subject to the constraint,

$$F(x_2, x_3) = x_3 - \frac{1}{2} \frac{x_2^2}{R} \quad (18)$$

Where R is the radius of curvature at the vertex. Although there are many ways to do this, here we shall implement a method often referred to as the method of Lagrangian multipliers. Thus, we have,

$$\frac{\partial}{\partial x_2} T(x_2, x_3) = \lambda \left(\frac{\partial}{\partial x_2} F(x_2, x_3) \right) \quad (19)$$

$$\frac{\partial}{\partial x_3} T(x_2, x_3) = \lambda \left(\frac{\partial}{\partial x_3} F(x_2, x_3) \right) \quad (20)$$

Substituting in the angular characteristic function and the surface we get two equations which may be solved to obtain the value of x_2 .

$$x_2 = - \frac{(p0_2 - p1_2) R}{p0_3 - p1_3} \quad (21)$$

And now substituting the expression for x_2 into $F(x_2, x_3)$ we can solve for x_3 .

$$x_3 = \frac{1}{2} \frac{(p0_2 - p1_2)^2 R}{(p0_3 - p1_3)^2} \quad (22)$$

Finally, after substituting in the expression for x_2 and x_3 into the angular characteristic we get,

$$T(p0_2, p1_2) = - \frac{1}{2} \frac{R (p0_2 - p1_2)^2}{p0_3 - p1_3} \quad (23)$$

From this the ray equations for the initial and final rays may be calculated.

$$y0 - \frac{z0 p0_2}{p0_3} = \frac{\partial}{\partial p0_2} T(p0_2, p1_2) \quad (24)$$

$$y1 - \frac{z1 p1_2}{p1_3} = \frac{\partial}{\partial p1_2} T(p0_2, p1_2) \quad (25)$$

Expressed explicitly as,

$$y0 - \frac{z0 p0_2}{p0_3} = - \frac{(p0_2 - p1_2) R}{p0_3 - p1_3} - \frac{1}{2} \frac{(p0_2 - p1_2)^2 R p0_2}{(p0_3 - p1_3)^2 p0_3} \quad (26)$$

$$y1 - \frac{z1 p1_2}{p1_3} = - \frac{(p0_2 - p1_2) R}{p0_3 - p1_3} - \frac{1}{2} \frac{(p0_2 - p1_2)^2 R p1_2}{(p0_3 - p1_3)^2 p1_3} \quad (27)$$

Now the ray equations can be parameterized with respect to a parameter, s , to allow for a conceptually more pleasing form. That is,

$$\mathbf{r} = s \cdot \mathbf{a} + \mathbf{b} \quad (28)$$

Where $\mathbf{a} = \langle p_2, p_3 \rangle$ and \mathbf{b} is a constant vector denoting a point of ray intersection. So, we simply make the substitution $z0 = s p0_3$ and $z1 = s p1_3$. The resulting coefficients for rays in vector form for the first medium are,

$$\mathbf{a}0 = \begin{bmatrix} p0_2 \\ p0_3 \end{bmatrix} \quad (29)$$

$$\mathbf{b}0 = \begin{bmatrix} -\frac{1}{2} \frac{(p0_2 - p1_2) R (2p0_3^2 - 2p0_3 p1_3 + p0_2^2 - p1_2 p0_2)}{(p0_3 - p1_3)^2 p0_3} \\ 0 \end{bmatrix} \quad (30)$$

And for rays in the second medium,

$$\mathbf{a}1 = \begin{bmatrix} p1_2 \\ p1_3 \end{bmatrix} \quad (31)$$

$$\mathbf{b}1 = \begin{bmatrix} -\frac{1}{2} \frac{(p0_2 - p1_2) R (-2p1_3^2 + 2p0_3 p1_3 - p1_2^2 + p1_2 p0_2)}{(p0_3 - p1_3)^2 p1_3} \\ 0 \end{bmatrix} \quad (32)$$

There is some ambiguity in the sign convention because of the dual sign of $p0_3$ and $p1_3$. To resolve this, we define incident rays to travel in the negative z direction and reflected rays to travel in the positive z direction.

Now to make more sense of this, we shall consider a numerical example. First, we define the sign of the optical momentum in the x_3 direction as $p0_3 = -\sqrt{1 - p0_2^2}$ and $p1_3 = \sqrt{1 - p1_2^2}$.⁸ Now to make more sense of this, we shall substitute in a numerical value for

⁸ The consequence of this direction choice is shown in Figure II-1. Note that it is also possible that both the initial and final rays both be heading in either the positive or negative x_3 direction. However, it doesn't make sense for the initial ray to be heading in the positive x_3 direction while the final ray heads in the negative x_3 direction.

optical momentum. We set $p\theta_2 = \cos\left(\frac{95 \cdot \pi}{180}\right)$ and $pI_2 = \cos\left(\frac{50 \cdot \pi}{180}\right)$ and $R = 1$. Thus, the resulting equations are,

$$\begin{bmatrix} x\theta_2 \\ x\theta_3 \end{bmatrix} = s\theta \cdot \begin{bmatrix} -0.08715574294 \\ -0.9961946981 \end{bmatrix} + \begin{bmatrix} -0.4217189032 \\ 0. \end{bmatrix} \quad (33)$$

$$\begin{bmatrix} xI_2 \\ xI_3 \end{bmatrix} = sI \cdot \begin{bmatrix} 0.6427876095 \\ 0.7660444433 \end{bmatrix} + \begin{bmatrix} -0.4861969307 \\ 0. \end{bmatrix} \quad (34)$$

As seen in Figure II-1, the equations above describe two lines whose slope and intersection with the y-axis are defined by the optical momentum. The rays intersect some point along the parabola surface and the angle they make with the surface obeys Snell's law.

One can understand the angular characteristic equation as being the optical path between the feet of the perpendiculars. That is, the signed distance $[N_0Q]$ is distance from the foot of the perpendicular to the optical surface along the initial ray. The signed distance $[QN_1]$ is the distance from the optical surface to the foot of the perpendicular along the subsequent ray. The total distance, $[N_0QN_1]$ is thus the distance between the foot of perpendicular for the initial and final ray. The angular characteristic is this distance times the appropriate index of refraction which provides the optical path length.

To clarify numerical, consider our example in Figure II-1. We substitute in the values for optical momentum into Equation (21) and (22), we obtain the coordinate of Q to be,

$$x_2 = -0.41421356 \quad (35)$$

$$x_3 = 0.085786437 \quad (36)$$

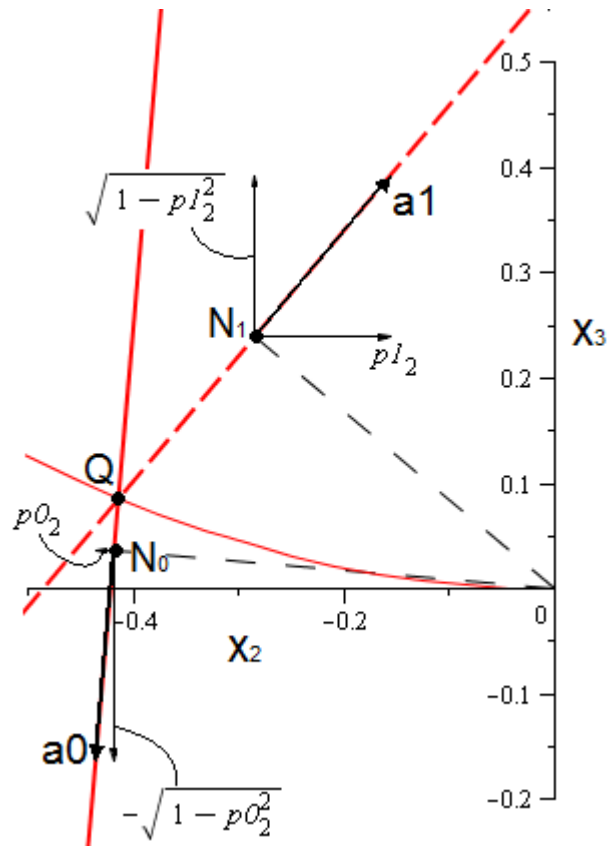


Figure II-1 - Illustration of the resulting rays from Equation (33) and (34).

As before, we break down the angular characteristic function into its constituent optical path lengths, N_0Q and $[QN_1]$.

$$[N_0Q] = p_{02}y + p_{03}z \quad (37)$$

$$[QN_1] = -p_{12}y - p_{13}z \quad (38)$$

Substituting in the appropriate values, we get,

$$[N_0Q] = -0.04936 \quad (39)$$

$$[QN_1] = 0.2005 \quad (40)$$

Notice how N_0Q , which is a measure on the back side of the parabola, is a negative value. Summing the two lengths together we get the value of the angular characteristic function.

$$T = 0.1512 \quad (41)$$

Phase Space for a Parabola

Although our previous discussion of the ray equations offer a more physically realistic analogy, from a mathematical perspective it can be useful to analyze an optical system's phase space. That is, a space that consists of both position and optical momentum coordinates. By

observing the ray equations, one can see that they can be expressed as a function of two coordinates. That is, $r_0 = r_0(x_0, p_0)$ and $r_1 = r_1(x_1, p_1)$. Also, we know that r_0 and r_1 can be mapped to one another. That is, a ray r_0 is mapped to a ray r_1 in a way governed by Snell's law and the contour of the parabolic surface.

As an example, consider Figure II-2 which shows us a pair of edge rays, denoted by blue and red, incident on the 45° rim of a parabolic trough. The intersection of these rays onto the focal plane is denoted by color coded dots A, B, C, and D. Each dot has a corresponding x_2 position coordinate and a p_2 momentum coordinate.

Figure II-3 is an illustration of the phase space along the focal plane. The dots A, B, C, and D are positioned within phase space according to the corresponding position and momentum coordinate. Going back and forth between the two illustrations will certainly help clarify how the points A, B, C and D map to one another in each illustration.

What is the point of this? Well, in addition to phase space being an alternative way of viewing rays incident on the focal plane, it also allows for a much clearer picture of how the rays r_0 map into the rays r_1 . If one wanted to understand this mapping based solely from Figure II-2, you would have to go to one ray at a time with a ruler and protractor to identify which initial rays maps to what final ray. On the other hand, by looking at Figure II-3 one can simply find the mapping of r_0 into r_1 by identifying the intersection point of the contour lines from r_0 phase space projected into r_1 phase space.

It is obviously more difficult to directly translate phase space to a physical picture just as it is difficult to determine the exact mapping of rays from a physical picture. Thus, the two illustrations complement one another.

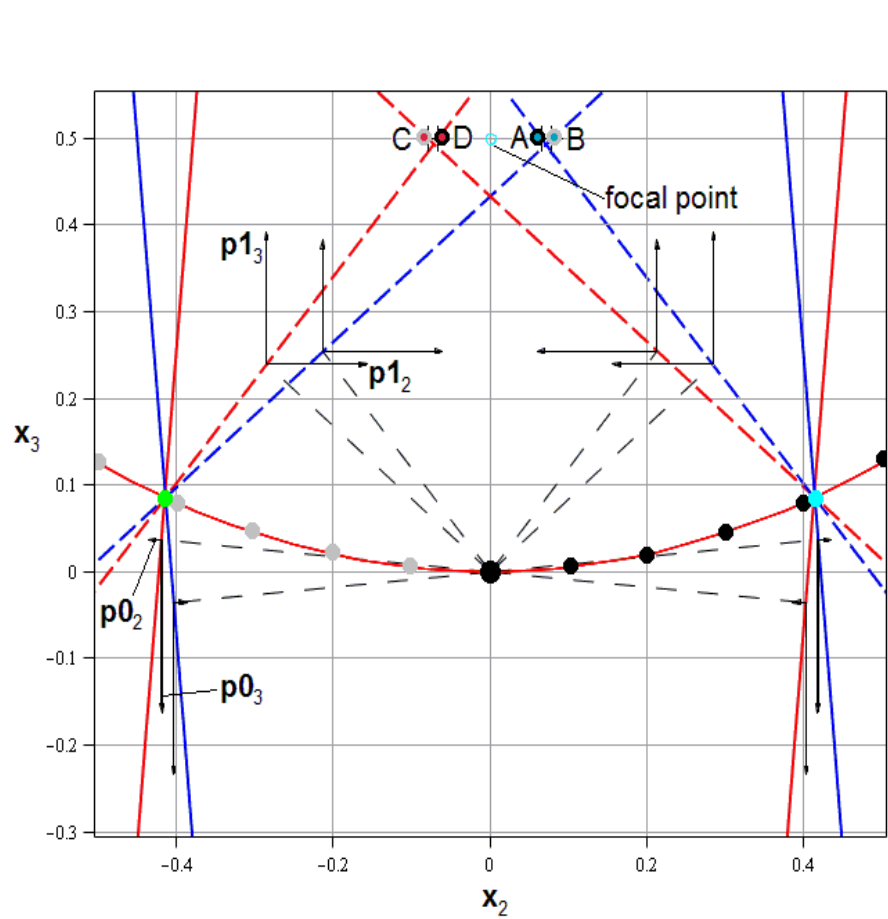


Figure II-2 - Illustration of edge rays incident on a parabola with a 45° rim angle.

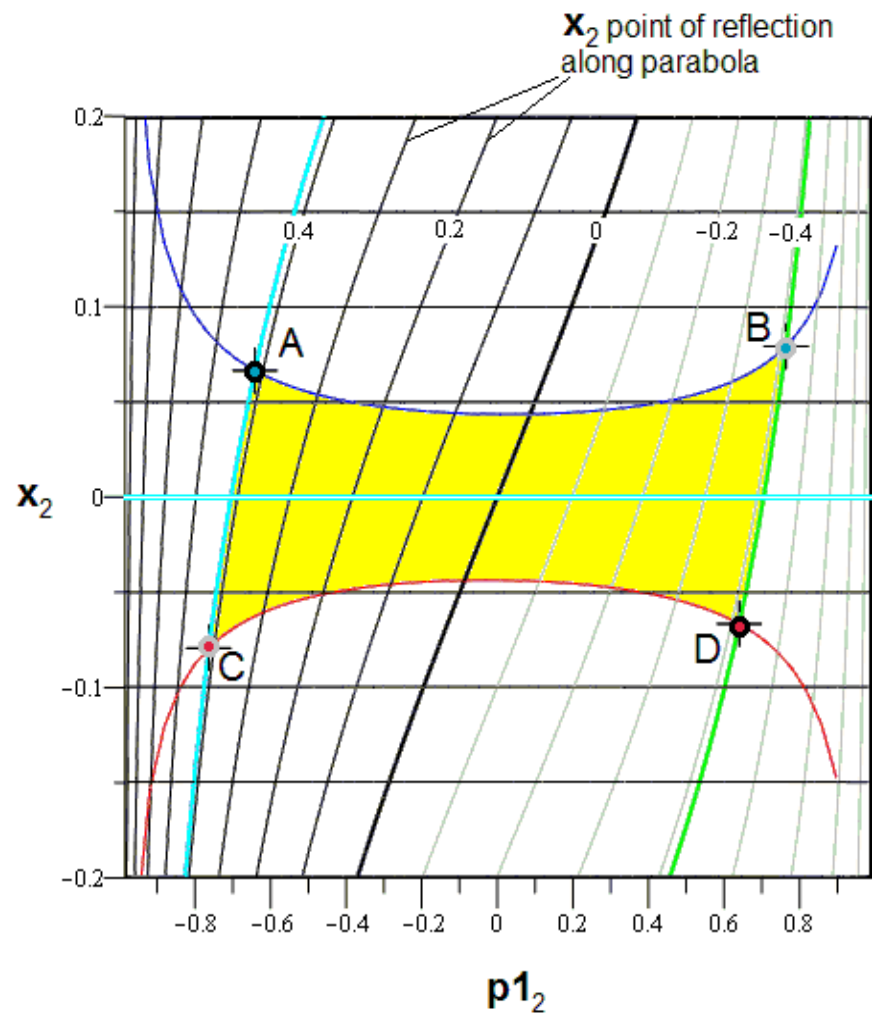


Figure II-3 - A projection of Appendix Figure II-4 showing the phase space at the focal plane.

Phase space is also an excellent way to illustrate the étendue and the thermodynamic efficiency of a concentrator. From the edge ray principle we know that light emitted between the edges of the object will always lie between the edges on the receiver. This boundary created by the edge rays given as the red and blue rays in real space correspond to the red and blue contour lines within phase space. The cyan and green point located at the 45° rim angle on the parabola also have corresponding cyan and green contour lines within phase space. Within the bounds of these four contour lines lie all possible ways rays from input space can map to output space. The volume within these boundaries is what we refer to as the étendue and it turns out that it must always be conserved [27].

From this concept of the étendue illustrated in phase space, we can also get a feel for its relationship with concentration. Clearly, if one wants to maximize concentration the projection of boundary contour lines from r_0 into r_1 should be parallel with the p_{12} axis. If this is not the case, then there is always a way of adjusting the lines such that the maximum distance between the lines is reduced while the phase space within the boundaries is maintained. Thus, increasing the concentration while obey the laws of thermodynamics.

Although it is truly possible to observe the four dimensions created by p_{02} , x_{02} , p_{12} , and x_{12} , it is possible to view a projection of r_0 in r_1 thanks to the bijective mapping property. As an aside, it might be useful to view how this projection from 3 dimensions reduces to two dimensions by observing Figure II-4.

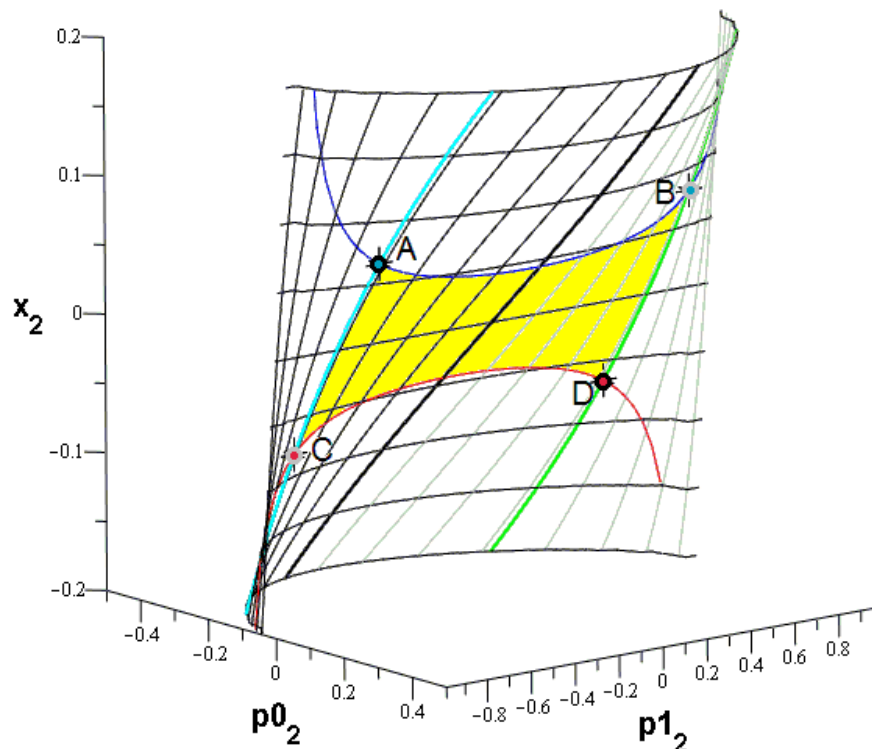


Figure II-4 - Illustration of the final ray position on the focal plane as a function of p_{02} and p_{12} .